UNIVERSITY OF CALIFORNIA
RIVERSIDE

Search for Self-Interacting Dark Matter With two Displaced Lepton-Jets Final State From Events Collected by the CMS Detector at LHC

A Dissertation submitted in partial satisfaction
of the requirements for the degree of

Doctor of Philosophy

in

Physics

by

Weinan Si

September 2020

Dissertation Committee:

Prof. Gail G. Hanson, Chairperson
Prof. Hai-bo Yu
Prof. Owen Long

The Dissertation of Weinan Si is approved:

Committee Chairperson

University of California, Riverside

Acknowledgments

I am grateful to my advisor, without whose help, I would not have been here.

To my parents for all the support.

ABSTRACT OF THE DISSERTATION

Search for Self-Interacting Dark Matter With two Displaced Lepton-Jets Final State From Events Collected by the CMS Detector at LHC

by

Weinan Si

Doctor of Philosophy, Graduate Program in Physics
University of California, Riverside, September 2020
Prof. Gail G. Hanson, Chairperson

This thesis presents an on-going search for self-interacting dark matter from events with two displaced lepton-jets in the CMS detector with pp collision data taken at $\sqrt{s} = 13\,\text{TeV}$ corresponding to 59.74 fb^{-1} of integrated luminosity during Run 2 of the LHC. Lepton-jet is a group of collimated leptons in a narrow cone, which can be the signature of dark photon Z_d – a theorized gauge boson which is charged under $\text{U}(1)_d$ gauge symmetry, bridging the dark sector and the Standard Model. As the first-round analysis, this search focuses more on displaced dark photons decaying to muon pair or electron pair. The expected results are presented as 95% confidence level upper limits on the self-interacting dark matter bound state production cross section, assuming the branch fraction of the bound state to dark photon pair is 100%.

Contents

List of Figures

List of Tables

Chapter 1

Introduction

We start to understand the world where we are living very long time ago. For thousands of years, generations after generations, our understanding was built upon the accumulation of daily experience and imaginations. It was only mostly in recent a few hundred years, the uprising of the acquirement of new knowledge by practicing experiments and observations advances our understanding in an unprecedented way. Benefiting from the invention of various experimental apparatus since one hundred years ago, we are capable to "observe" the microscopic world which is impossible with our native eyes. Finally we are approaching the answer to the question – *what is our world made of?*

At the beginning of the 20th century, the discoveries of the electron, proton and neutron, together with development of Quantum Mechanics and Special Relativity, opened the treasure chest of particle physics. In the following few decades, the progress of this subject rewards us with a remarkable insight of the fundamental structure of the world. Almost everything is composed of a few building blocks and their behavior can be explained by the interactions between them. It was so successful, which could describe all known elementary particles and three of the four interactions, that people name it as the Standard Model (SM) of the particle physics. The SM was gradually established in 1970s and 80s accompanying with a series of discoveries of quarks, gluons, and $W^{\pm}$ and Z bosons. The last missing piece of the SM, the Higgs boson H, was discovered at the Large Hadron Collider (LHC) in 2012 [27,28].

Although the predictions provided by the SM have been tested up to very short scales ($\mathcal{O}(10^{-19})$ m) by high energy ($\mathcal{O}(1)$ TeV) colliders, however, it is not *the theory of everything* as there are several problems which cannot be resolved. For example, one of the fundamental interaction, gravity, is not incorporated by the SM; the SM does not predict the existence of the Dark Matter (DM), which is believed to account for $\sim 80\%$ of the matter of the Universe. Additionally, the values of some fundamental parameters do not seem to be “natural” when we stare at them. The gravitational force is so weak when compared with the strong, weak and electromagnetic forces. The mass of the three generations of elementary particles differs so much. And neutrinos are observed to be massive from the oscillation experiments. These puzzles prompt physicists for continuous theory developments and experimental efforts. Being part of this quest, the work presented by this thesis is about the search for DM with the assumption that there is self-interaction between them with terrestrial collider experiment, the CMS detector at LHC. In Chapter 1, the theoretical motivation and the model are described; the description of experimental apparatus is present in Chapter 2; the data analysis procedures and techniques are provided in Chapter 3; at last, the summary and remarks are made in Chapter 4.

1.1 The Standard Model

1.1.1 Elementary particles

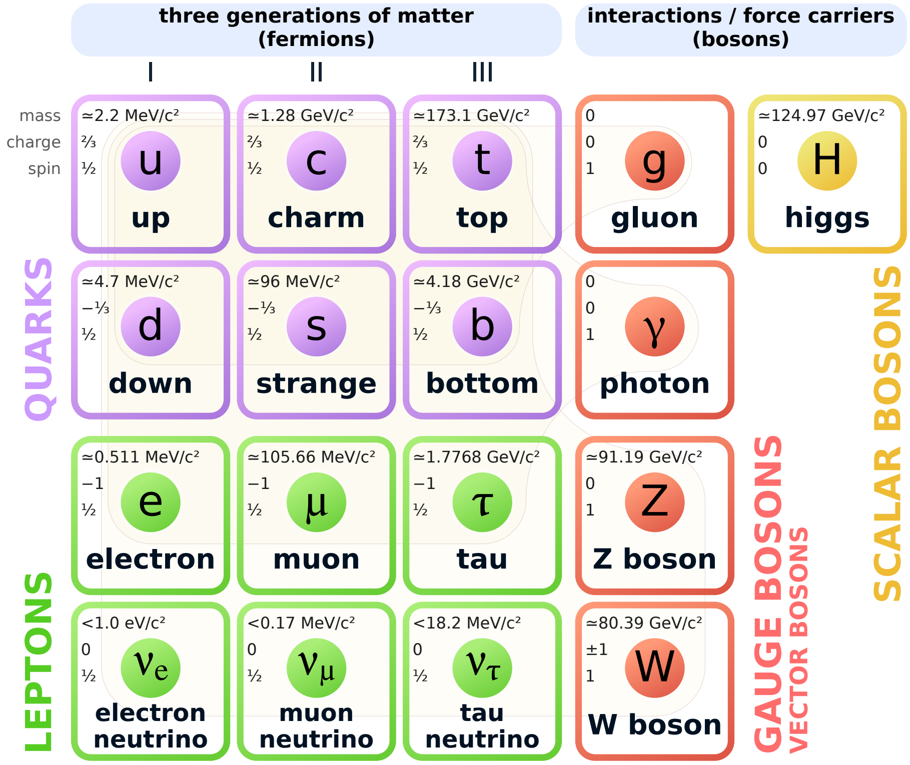

Figure 1.1: Standard Model of elementary particles

The elementary particles are categorized as the bosons and the fermions based on their intrinsic spins. The fermions have spin values as half-integers ($\pm 1/2, \pm 3/2, ...$) while the bosons have their spins as integers ($0, \pm 1, ...$). In SM, there are twelve fermions, four gauge bosons and one Higgs boson. The fermions are divided into the quarks (up u, down d, charm c, strange s, top t, bottom b, six in total) and the leptons (electron e, electron neutrino ν_e, muon μ, muon neutrino ν_μ, tau τ, tau neutrino ν_τ, six in total). The quarks have electric charge of $2/3$ or $-1/3$ of unit charge ($e = 1.602 \times 10^{-19}$ C), they participate in all three fundamental interactions. The leptons have electric charge of -1 or 0 of unit charge, they only take part in weak and electromagnetic interactions. The type of quarks or leptons is called “flavor”. Pairs of quarks and leptons are grouped into three generations, as shown in figure 1.1.

The fermions are the fundamental building blocks of the visible matter in the Universe, it is the gauge boson that carries the force and mediates the interactions among them. Of the three interactions described by the SM, strong, weak and electromagnetic forces, the corresponding gauge bosons are the gluon g, the $W^{\pm}, Z$ bosons, and the photon γ. Besides, the SM includes a Higgs boson, whose spin is 0. It is the quantum particle associated with the Higgs field, where SM particles acquire mass by interactions with it.

By convention, the energy, momentum and mass of particles are expressed in the unit of electronvolt (eV), following the natural unit system, in which both the reduced Planck constant $\hbar$ and the speed of light c equal to 1.

1.1.2 Fundamental interactions

Except gravity, the other three fundamental interactions are well described by the SM. The strong interactions bind the quarks into hadrons as bound states. The coupling strength of the strong force, α_s has a strong dependence on the energy scale of the interaction. The weak interactions are responsible for phenomena like nuclear β decay. Its coupling strength is six orders of magnitude smaller than the strong coupling strength at $\sim 1\,\text{GeV}$. The electromagnetic interactions happen among electrically charged particles, its coupling strength is known as the *fine structure constant* with value $\alpha \simeq \frac{1}{137}$. At energy over the so-called electroweak scale, at the order of $10^2\,\text{GeV}$, the electromagnetic and weak forces are unified as the electroweak force. A summary of the three fundamental interactions and their coupling strength is given in table 1.1.

Interaction	Force Carrier	Coupling Strength
Strong	g	1
Weak	$W^{\pm}, Z$	10^{-6}
Electromagnetic	γ	10^{-2}

Table 1.1: Summary of the SM fundamental interactions and coupling strengths

Gauge Theory In mathematical language, the SM interactions are described by a quantum field theory (QFT) that conforms to local gauge symmetries, i.e., the Lagrangian of the SM is invariant under local gauge transformations. For a SM Fermion, a local gauge transformation is defined as a local phase transformation

$$\psi \rightarrow \psi' = e^{it^a \alpha_a(\mathbf{x})}\psi \tag{1.1}$$

, where t^a are the generators of the symmetry group, α_a are functions of space-time coordinates $\mathbf{x}$, a are indices of the generators of the symmetry group. A $\mathrm{U}(N)$ group is a group of $N \times N$ complex matrices that each matrix U in the group satisfies $\mathrm{U}^\dagger\mathrm{U} = \mathrm{U}\mathrm{U}^\dagger = \mathbb{1}$. An $\mathrm{SU}(N)$ group is an $\mathrm{U}(N)$ group with additional requirements that the determinant of U must equal to 1. The gauge symmetry in the SM can be represented as $\mathrm{SU}(3)_C \times \mathrm{SU}(2)_L \times \mathrm{U}(1)_Y$, where the strong interaction is associated with $\mathrm{SU}(3)_C$ symmetry, the electroweak interaction is associated with $\mathrm{SU}(2)_L \times \mathrm{U}(1)_Y$ symmetry. In QFT, a gauge invariant Lagrangian can be generally written as

$$\mathcal{L} = -\frac{1}{4}F^a_{\mu\nu}F^{\mu\nu}_a + \bar{\psi}_i(i\gamma^\mu D_\mu - m_i)\psi_i \tag{1.2}$$

with the covariant derivative

$$D_\mu = \partial_\mu - igt_a A^a_\mu \tag{1.3}$$

and the field tensor

$$F^a_{\mu\nu} = \frac{[D_\mu, D_\nu]}{ig} = \partial_\mu A^a_\nu - \partial_\nu A^a_\mu - igf^{abc} A^b_\mu A^c_\nu \tag{1.4}$$

where μ, ν represent the space-time indices, ψ_i represent the fermion fields, m_i are the mass of fermions, γ^μ are Dirac matrices, $\bar{\psi_i} = \psi^\dagger \gamma_0$, A^a_μ are gauge boson fields, and g is the coupling constant. In the Lagrangian, each group generator t_a is associated with a gauge boson field A^a_μ. The gauge boson fields couple to the fermion fields with the coupling constant g. In order to maintain the gauge invariance in the Lagrangian, the gauge boson fields have to transform as $A^a_\mu \to e^{it^a\alpha_a(\mathbf{x})}(A^a_\mu - \frac{i}{g}e^{-it^a\alpha_a(\mathbf{x})}\partial_\mu e^{it^a\alpha_a(\mathbf{x})})e^{-it^a\alpha_a(\mathbf{x})}$. The gauge bosons are massless since otherwise the mass term $mA^a_\mu A^\mu_a$ will violate the gauge invariance.

Strong Interaction The strong interaction is represented by SU$(3)_C$ gauge symmetry. The *charge* (quantum number) of SU$(3)_C$ gauge symmetry is called *color*. There are three colors: red r, green g and blue b and each quark carries one color charge. The quark's field is expressed as triplets composed of the color components (e.g. $\psi_u = \begin{pmatrix} u_r \\ u_g \\ u_b \end{pmatrix}$ and $\psi_d = \begin{pmatrix} d_r \\ d_g \\ d_b \end{pmatrix}$ for up and down quark fields respectively). The generators in the SU$(3)_C$ group correspond to the 8 Gell-Mann matrices and yield 8 gluon field carriers, each carrying two color charges. Quarks interact with each other and form colorless bound states by exchanging gluons.

Electroweak Interaction The electroweak interaction is represented by SU$(2)_L \times$ U$(1)_Y$ symmetry, or *electroweak symmetry.* In SU$(2)_L$ symmetry, one *up-type* fermion and one *down-type* fermion of the same generation form a doublet that transforms under the

SU(2)$_L$ group. The up-type fermions include u, c, t, ν_e, ν_μ and ν_τ. The down-type fermions include d, s, b, e, μ and τ. Those doublets are written as $\psi = \left(\begin{smallmatrix} u \\ d \end{smallmatrix}\right)_L$, $\psi = \left(\begin{smallmatrix} e \\ \nu_e \end{smallmatrix}\right)_L$, etc. The quantum number associated with SU(2)$_L$ gauge symmetry is weak-isospin T_3, with values as $\pm\frac{1}{2}$. The left-handed up-type fermion carries $T_3 = +\frac{1}{2}$ while left-handed down-type fermion carries $T_3 = -\frac{1}{2}$. The right-handed fermions carry $T_3 = 0$ and do not participate in weak interactions, except for the right-handed neutrinos which do not exist in the SM. The left- and right-hand projections of the fermion fields $\psi_{\text{left/right}}$ are defined as $\psi_{\text{left/right}} = \frac{1+/-\gamma^5}{2}\psi$, where γ^5 is the fifth gamma matrix. The three generators of SU(2)$_L$ gauge group are the Pauli matrices and correspond to three gauge bosons W^a ($a = 1, 2, 3$), which process weak-isospin T_3 of 1, 0, -1 for $a = 1, 2, 3$ respectively. Both Left- and right-handed fermions transform under U(1)$_Y$ gauge symmetry. The quantum number associated with U(1)$_Y$ gauge symmetry is the weak hypercharge Y, which correlates with the electric charge Q and the third component of the weak-isospin T_3 by $\text{Q} = T_3 + \frac{\text{Y}}{2}$. The generator of U(1)$_Y$ group corresponds to the gauge boson B, which couples to both left- and right-handed fermions.

The Higgs Mechanism and Electroweak Symmetry Breaking The gauge bosons associated with the electroweak symmetry, $W^a (a = 1, 2, 3)$ and B, are all massless. However, the observation of massive $W^\pm$ and Z bosons suggests that the electroweak symmetry is broken. In the SM, the electroweak symmetry is a broken symmetry due to the Higgs mechanism [29–31], and $W^\pm$, Z and γ are produced by the mixings of W^a and B gauge boson after the electroweak symmetry breaking.

The Higgs mechanism adds a complex doublet field ϕ with $\mathrm{Y} = 1$ and $T_3 = -\frac{1}{2}$ to the SM fields. The Lagrangian for the doublet field is invariant under the electroweak symmetry breaking and is written as

$$\mathcal{L} = (D^{\mu}\phi)^{\dagger}(D_{\mu}\phi) - \mu^2\phi^{\dagger}\phi - \lambda(\phi^{\dagger}\phi)^2 \tag{1.5}$$

, where $\mu^2 < 0$ and $\lambda > 0$. In the Lagrangian, the covariant derivative D_μ is written as

$$D_{\mu} = \partial_{\mu} - ig\sigma_a W^a_{\mu} + ig'\frac{\mathrm{Y}}{2}\mathrm{B}_{\mu'} \tag{1.6}$$

, where σ_a are Pauli matrices (generators of $\mathrm{SU}(2)_L$ group), g is the coupling constant associated with W^a gauge bosons, g' is the coupling constant associated with the B gauge boson. In equation (1.5), the first term is the kinematic term of the field, the second and the third term describe the Higgs potential. The Higgs potential $V(\phi^{\dagger}\phi)$ has a minimum value at $\phi^{\dagger}\phi = -\frac{\mu^2}{\lambda} = v^2$, v is called the vacuum expectation value (VEV) of the Higgs potential. In general, the Higgs doublet field can be written as $\phi = \left(\begin{smallmatrix}\phi_1 + i\phi_2 \\ \phi_3 + i\phi_4\end{smallmatrix}\right)$, where ϕ_{1-4} are real scalar fields. At the ground state of the Higgs potential, ϕ can be expressed in terms of a constant part that reflects the non-zero value of the ground state v plus a variable field $H(x)$ that is small for perturbations around the ground state: $\phi = \frac{1}{\sqrt{2}}\left(\begin{smallmatrix}0 \\ v + H(x)\end{smallmatrix}\right)$. By inserting ϕ into the Higgs potential, the following can be obtained:

$$V = \frac{\mu^2}{2}H^2 + \frac{\mu^2}{\lambda}H^3 + \frac{\mu^2}{4\lambda^2}H^4 \tag{1.7}$$

The Higgs potential, therefore, describes a scalar particle. The Higgs boson, which process a mass of $\sqrt{2}\mu$. The $W^{\pm}, Z$ boson fields and photon field (A) are expressed as:

$$W^{\pm}_{\mu} = \frac{1}{\sqrt{2}}(W^1_{\mu} \mp iW^3_{\mu}) \tag{1.8}$$

$$\begin{pmatrix} Z_\mu \\ A_\mu \end{pmatrix} = \begin{pmatrix} \cos\theta_W & \sin\theta_W \\ -\sin\theta_W & \cos\theta_W \end{pmatrix} \begin{pmatrix} W_\mu^2 \\ \mathrm{B}_\mu \end{pmatrix} \tag{1.9}$$

, with masses

$$M_{W^\pm} = \frac{1}{2}vg, \quad M_Z = \frac{1}{2}v\sqrt{g^2 + g'^2}, \quad M_\gamma = 0 \tag{1.10}$$

, where $\cos\theta_W = \frac{M_{W^\pm}}{M_Z} = \frac{g}{\sqrt{g^2+g'^2}}$. θ_W is named as the Weinberg angle. From equations above, it can be seen that the SM $W^\pm, Z$ and γ come from the mixing of $W^a(a = 1, 2, 3)$ and B gauge bosons, and gain masses from the non-zero VEV of the Higgs potential.

The Fermion's mass Although the mass term for the fermions, $m_i\bar{\psi}_i\psi_i$, in equation (1.2) does not violate SU(3)$_C$ symmetry, it does violate the SU(2)$_L$ symmetry as it mixes the left- and right-handed fermions. This is addressed by adding a Yukawa coupling term between the Higgs boson and the fermions to the SM Lagrangian

$$\mathcal{L}_{\text{Yukawa}} = -g_l\bar{L_L}\phi l_R - g_d\bar{Q_L}\phi d_R - g_u\bar{Q_L}\phi^C u_R + h.c. \tag{1.11}$$

, where L_L and Q_L are left-handed lepton and quark doublets, ϕ^C is the charge conjugate of the Higgs field, $g_{l,d,u}$ are Yukawa coupling constants. By inserting $\phi^C = \frac{1}{\sqrt{2}}\binom{v+H}{0}$, the following can be obtained

$$\mathcal{L}_{\text{Yukawa}} = -g_f\frac{v}{\sqrt{2}}\bar{\psi}\psi - \frac{g_f}{\sqrt{2}}\bar{\psi}\psi H \tag{1.12}$$

. From which, the fermions acquire mass $m_f = g_f\frac{v}{\sqrt{2}}$ by interacting with the Higgs field.

1.2 Evidence of the Dark Matter

Despite the tremendous success of the SM in describing the matter and the interactions we've known so far, it is not the completion of physics. By observing the stars, galaxies and halos in the Universe, we find some phenomena very puzzling unless something not visible is there in the darkness. They point to us the evidence of the existence of the *dark matter*. However, it is not predicted by the SM.

1.2.1 Rotation curves

One of the most convincing evidence of the existence of the dark matter comes from the analysis of galaxy's rotation curves, the orbital velocities of stars, gases with respect to the distance from the galaxy center. In the outer galactic region where there is no stars but only cold hydrogen, it is measured by observing emission at the wavelength of 21-cm corresponding to ultra-thin splitting due proton-electron spin interactions. The orbiting of a galaxy leads to Doppler shift of the 21-cm line, which allows the estimation of the gas rotational velocity. According to Kepler's law, the orbital velocity of an object at distance r from the center of the galaxy is

$$v^2(r) = \frac{GM(r)}{r} \tag{1.13}$$

, where $M(r)$ is the mass distribution of the galaxy embedded into a sphere of radius r. When r is large enough, the observed $M(r)$ begins to remain constant with the growth of r, the relationship of the v of a distant object with respect to r should become

$$v \sim \frac{1}{\sqrt{r}} \tag{1.14}$$

.

However, soon after extending to larger radii using 21-cm radio observations [32, 33], optical observations by Rubin and Ford of M31 [34] revealed a circular velocity that did

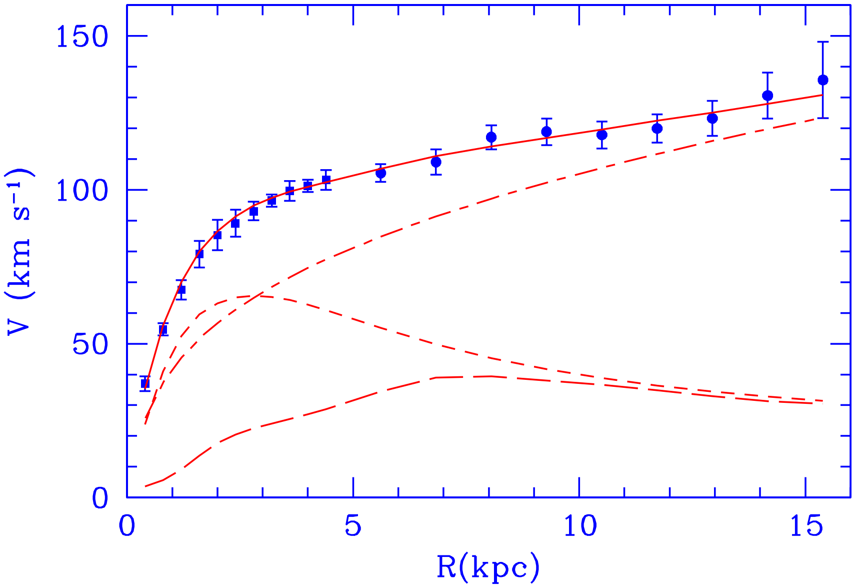

Figure 1.2: The rotation curve of M33 galaxy (blue dots). The solid line represents the best fit. In M33 there are four types of observed matter: stellar disk, atomic gas, warm ionized gas and molecular gas. The contributions are shown for the observed stellar disk (short dashed), gaseous matter (long dashed) and dark matter (dot dashed). Reprinted from [1].

not fall off, but remained approximately constant. Many other spiral galaxies were found to exhibit the same behavior [1, 35–38], e.g. M33 in figure 1.2. The fact that the mean rotational velocity $\bar{v}$ remains constant with respect to r implies that $M(r)$ is proportional to r:

$$M(r) = \frac{\bar{v}^2 r}{G} \tag{1.15}$$

, indicating that most of the mass in galaxies is found in massive, non-luminous halos extending far beyond the spatial extent of luminous stars and gas [39, 40].

1.2.2 Gravitational lensing

Another compelling evidence of the DM is *gravitational lensing*, which is distortion and magnification of the light emitted by distant galaxies caused by non-uniform distribution of matter along the path of the propagation. The effect is equivalent to viewing an object through a lense that has a spatially varying index of refraction. By measuring the distortion and the magnification, one can determine the mass distribution of the galaxy cluster. The distant galaxies often appear as tiny elliptical images, which are called arclets [2]. An example of such arclets of the cluster `RX J1347-1145` is shown in figure 1.3.

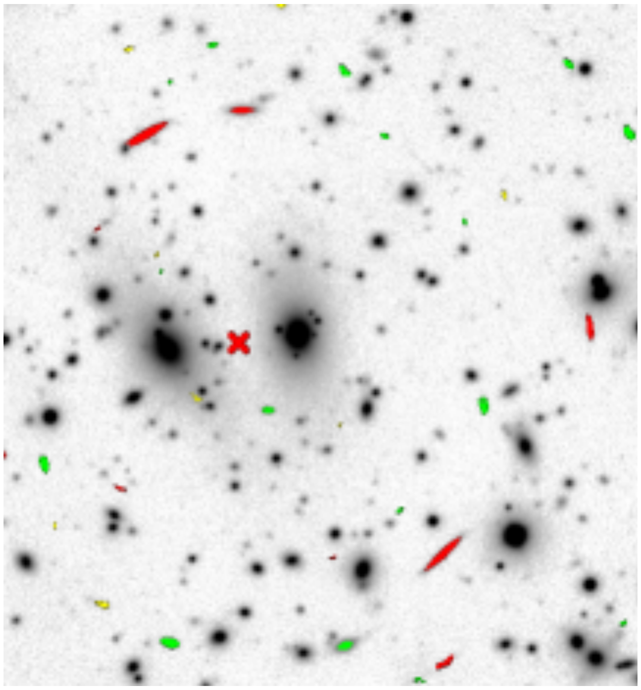

Figure 1.3: Image of the cluster `RX J1347-1145`. The colors encode the objects eccentricity: [0.7, 0.8] - green, [0.8, 0.9] - yellow, [0.9, 1.0] - red, i.e. the red objects are most likely arcs. The assumed center of the cluster is marked with a red cross. Reprinted from [2].

Analysis of the results of gravitational lensing made in the last ten years has revealed that the diameter of the dark halo in the galaxies may be more than one order of magnitude greater than the visible diameter of a galaxy itself.

1.3 Dark matter candidates and crisis on small scales

1.3.1 Dark matter candidates, WIMPs

The existence of DM in the Universe is exclusively deduced from its gravitational effect on the behavior of astrophysical systems. At first, neutrino was thought to be a promising DM candidate within the SM [41–43]. A relic thermal bath of neutrinos produced alongside the cosmic microwave background (CMB), could yield the required mass density if the mass of neutrino was in the order of $\mathcal{O}(10)$ eV. However, because neutrinos are "hot" DM, they decouple from photons and electrons around the neucleosynthesis epoch while still being relativistic, the free-streaming would lead to the density fluctuations below supercluster scales get erased. Numerical simulations have shown that the top-down structure formation where superclusters form first in the neutrino-dominated universe then subsequently fragment into galaxies, is incompatible with galaxy clustering constraints [44–46].

With no viable DM candidate within the SM, the underlying theory for DM remains unknown. Many new particle theories are proposed to address the shortcomings of the SM while providing candidate for DM as new particles. The examples include weakly-interacting massive particles (WIMP) motivated by the hierarchy problem, such as neutralinos in supersymmetric models [47, 48] and Kaluza-Klein states in extra dimensional models [49, 50], as well as extreme light axion particles [51] associated with the solution to the strong CP problem in QCD [52]. The comic abundance of these new particles can be naturally close to DM abundance inferred from the cosmological observations. This coincidence has motivated decades of efforts to search for the particle physics realization of DM beyond the SM.

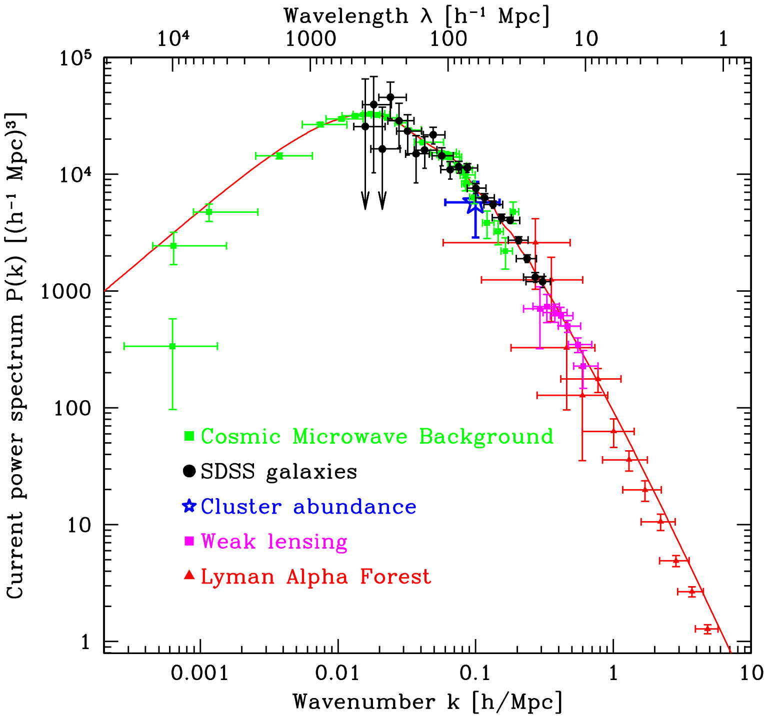

Figure 1.4: Matter power spectrum inferred through cosmological measurements. Red line shows the best fit for ΛCDM cosmology for a simiplified five-parameter model, assuming a flat spatial geometry and a scale-invariant primordial spectrum. Reprinted from [3].

So far, cosmological data has converged upon the ΛCDM paradigm as the standard model of cosmology. Of the total mass-energy content of the Universe, approximately 26% is cold dark matter (CDM) and 5% is baryonic matter (while the reminder is consistent with a cosmological constant Λ), with a nearly scale-invariant spectrum of primordial fluctuations [53]. In this picture, structure in the Universe forms as the primordial overdensities collapse under the gravity. Since CDM, acting as a pressureless fluid, is more dominant and collapse more readily than baryonic matter, it provides the gravitational potential underlying the distribution of visible matter in the Universe. The observed matter power spectrum, as obtained from a variety of cosmological probes, is in remarkable agreement with ΛCDM cosmology, shown in figure 1.4. In addition, the ΛCDM model also explains many important aspects of galaxy formation [54, 55].

The most popular DM candidate are WIMPs, whose naming indicates that they participate in the weak interaction in addition to the gravity. The expected WIMP mass is usually considered in the order of $\mathcal{O}(1)\,\mathrm{GeV} - \mathcal{O}(10)$ TeV. Should they were present in thermal equilibrium in the early universe, WIMPs would annihilate with one another so that a predictable number of them are left today. An annihilation cross section of weak interaction strength automatically gives the right abundance in the present Universe, near the value measured by WMAP experiment [56]. This coincident is known as the WIMP miracle [57].

1.3.2 Crisis on small scales

On large scales ($> \mathcal{O}(\mathrm{Mpc})$), the structure of the Universe is consistent with DM particles that are cold, collisionless, and interact with each other in addition to the SM particles purely via gravity (figure 1.4). On smaller scales, structure formation becomes strongly nonlinear and N-body simulation have become the standard tool to explore this regime. Cosmological DM-only simulations have provided several predictions for the structure and abundance of CDM halos and their substructures. However, it remains unclear whether these predictions are borne out in nature. Since the 1990s, four main discrepancies between CDM predictions and observations have come to light.

Core-cusp problem: Collisionless CDM-only simulations predict "cuspy" DM density profiles whose logarithmic slope, defined by $\alpha = \mathrm{d}\ln\rho_{\mathrm{DM}}/\mathrm{d}\ln r$, tends to be $\alpha \sim -1$ at small radii (or $\rho_{\mathrm{DM}} \propto r^{-1}$) [58–61]. Such halos are well- described by the Navarro-Frenk-White (NFW) profile [59, 60],

$$\rho_{\mathrm{NFW}}(r) = \frac{\rho_s}{(r/r_s)(1 + r/r_s)^2} \tag{1.16}$$

, where r is the radical coordinate and ρ_s and r_s are characteristic density and scale radius of the halo, respectively. On the other hand, many observations do not find evidence for the steep inner density slope predicted for collisionless CDM, preferring "cored" profiles with inner slopes $\alpha \sim 0$ (or $\rho_{\mathrm{DM}} \propto r^0$) that systematically shallower. This discrepancy is known as "core-cusp" problem.

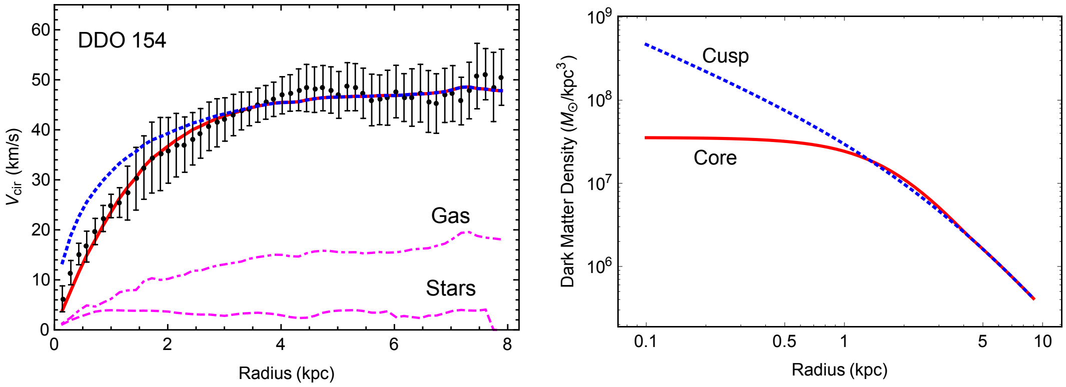

Figure 1.5: *Left*: The observed rotation curve of the dwarf galaxy `DDO 154` (black dotted) [4] compare to models with an NFW profile (blue dotted) and cored profile (red solid). Stellar (gas) contributions is indicated by pink (dot-) dashed lines. *Right*: Corresponding DM density profiles adopted in the fits. NFW halo parameters are $r_s \approx 3.4$ kpc and $\rho_s \approx 1.5 \times 10^7\ \mathrm{M}_\odot/\mathrm{kpc}^3$, while the cored density profile is generated using an analytical SIDM halo model developed in [5, 6]. Reprinted from [7].

Late-type dwarfs and low surface brightness (LSB) galaxies are ideal for testing CDM predictions as they are DM dominated down to small radii (or over all radii) and environmental disturbances are minimal. Flores & Primack [62] and Moore [61] first recognized the core-cusp issue based on HI rotation curves for several dwarfs, which, according to observations, are well described by cored profiles. Figure 1.5 illustrates the rotation curve of the dwarf galaxy `DDO 154`. On the left, it shows the measured HI rotation curve [4] compared to the fits with cuspy (NFW) and cored profiles, which are shown on the right. The NFW halo has been chosen to fit the asymptotic velocity at large radii and match the median cosmological relations between ρ_s and r_s [6]. However, this profile over-predicts $V_{\rm circ}$ in the inner region. This discrepancy is a symptom of too much mass for $r \lesssim 2$ kpc, while the data favors a shallower cored profile with less enclosed mass.

Diversity problem In ΛCDM, the hierarchical structure formation produces self-similar halos well-described by NFW profiles. Since the halo parameter (e.g. ρ_s and r_s) are strongly correlated, there is only one parameter specifying a halo. For example, once the maximum circular velocity $V_{\rm max}$ (or any other halo parameter) is fixed, the halo density profile is completely determined at all radii including the inner density cusp (up to scatter). On the other hand, the inner rotation curves of observed galaxies exhibit considerable diversity.

Omen et al. [8] parametrized the diversity of rotation curves directly by comparing $V_{\rm circ}(2\ \rm kpc)$ versus $V_{\rm max}$, which represent the inner and outer halos, respectively. Figure 1.6 shows the scatter in these velocities for observed galaxies (blue points) compared to the correlation expected from CDM-only halos (solid line) and CDM halos with baryons (red band). For $V_{\rm max}$ in the range of $50 - 300$ km/s, the spread in $V_{\rm circ}(2\ \rm kpc)$ is a factor of 3 for a given $V_{\rm max}$.

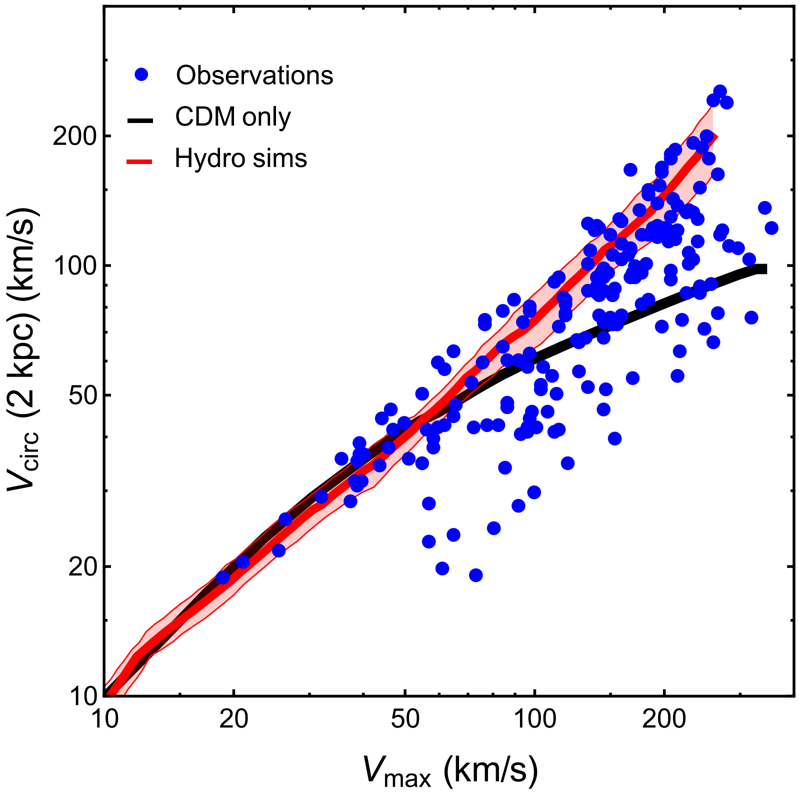

Figure 1.6: The total (mean) rotation speed measured at 2 kpc versus the maximum rotation speed for observed galaxies. Black solid line represents CDM-only prediction expected for NFW halos of average concentration. Red thick line show the mean relation predicted in the cosmological hydrodynamical simulations (the shaded areas indicate the standard deviation). Reprinted from [8].

Missing satellite problem: CDM halos are rich with substructures, since they grow via hierarchical merging of smaller galaxies that survive the merging process [63]. From the observations, however, the number of small galaxies in the Local Group are far fewer than the number of predicted subhalos. In the Milky Way (MW), simulations predict $\mathcal{O}(100-1000)$ subhalos large enough to host galaxies, while only 11 dwarf satellite galaxies were known when this issue was first raised [64, 65]. Nearby galaxies in the field exhibit a similar under-abundance of small galaxies compared to the prediction from simulations [66, 67].

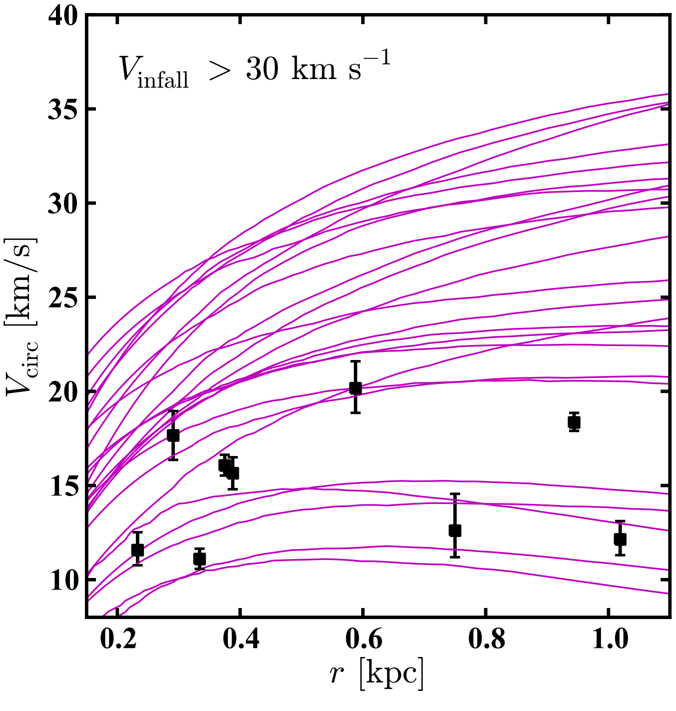

Figure 1.7: Circular velocity profiles for MW subhalos with $V_{\mathrm{max}} > 30$ km/s predicted from CDM simulations (purple lines), each data points corresponds to V_{circ} evaluated at the half-light radius for nine brightest MW dwarf spheroidal galaxies. Reprinted from [9].

Too-big-to-fail problem (TBTF): In recent years, much attention has been paid to the most luminous satellites in the MW, which are expected to inhabit the most massive subhalos in CDM simulations. However, it seems that these subhalos are too dense in the central regions to be consistent with the stellar dynamics of the brightest dwarf spheroidals. Boylan-Kolchin et al. [9, 68] showed that the population of the MW's brightest dSph galaxies exhibit a discrepancy with respect to CDM predictions, as shown in figure 1.7. The simulations predict $\mathcal{O}(10)$ subhalos with $V_{\rm max} > 30$ km/s, whereas the bright MW dSphs have stellar dispersions corresponding to CDM subhalos with $12 \lesssim V_{\rm max} \lesssim 25$ km/s.

The origin of the name stems from the expectation that such massive subhalos are too big to fail in forming stars and should host observable galaxies. At face value, the issue is reminiscent of the core-cusp/mass deficit problems for rotation curves and other observations. Thus one way to resolve the TBTF problem is if these galaxies have reduced central densities compared to CDM halos. By generating cored profiles in low-mass halos, self-interactions may resolve this issue for the dwarf galaxies in the MW [69, 70], Local Group [71], and the field [72].

It must be emphasized, however, that these issues originally gained prominence by comparing observations to theoretical predictions from DM-only simulations. Hence, there has been extensive debate in the literature whether these small scale issues can be alleviated or solved in the ΛCDM framework once dissipative baryonic process such as gas cooling, star formation, and supernova feedback are included in simulations [73, 74]. On the other hand, a more intriguing possibility is that CDM paradigm may break down on galactic scales. One early attempt to solve these issues supposes that DM particles are warm, instead of cold, meaning that they were quasi-relativistic during kinetic decoupling from the thermal bath in the early Universe [75, 76]. However, the favored mass range of the thermal warm DM is in strong tension with Lyman-α forest observations [77, 78] and the abundance of high redshift galaxies [79]. Also, while warm DM halos have constant density cores set by the phase space density limit, the core sizes are far too small to solve the core-cusp problem given Lyman-α constraints [80].

1.4 Self-Interacting Dark Matter

Another promising alternative to the collisionless CDM is self-interacting dark matter (SIDM), proposed by Spergel & Steinhardt [81] to solve the core-cusp and missing satellites problems. In this scenario, DM particles scatter elastically with each other through $2 \rightarrow 2$ interactions. The self-interactions lead to radical deviations from CDM predictions for the inner halo structure, shown in figure 1.8. The expectations for SIDM halos (blue) compared to CDM halos (black) are summarized as following:

Isothermal velocity dispersion: Although a CDM halo is a virialized object, the DM velocity dispersion, indicating the "temperature" of DM particles, is not a constant and decreases toward the center in the inner halo. Self-interactions transport heat from the hotter outer to the cooler inner region of a DM halo, thermalizing the inner halo and driving the velocity dispersion to be uniform across radius. The velocity distribution function for SIDM is more Maxwell-Boltzmann compared to CDM [82].

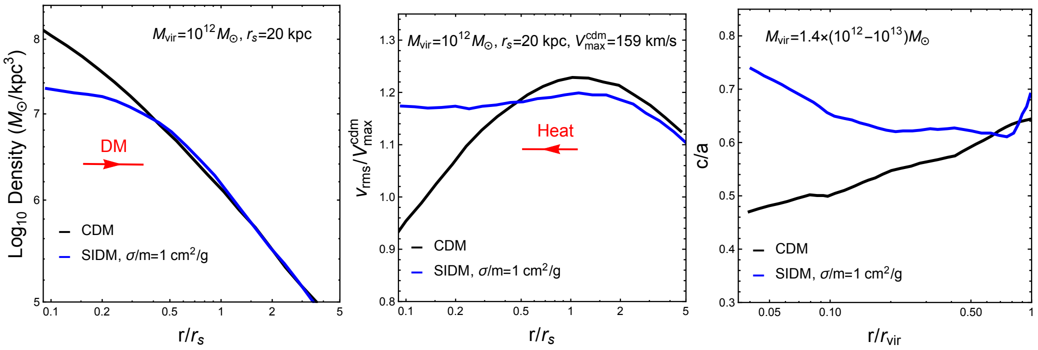

Figure 1.8: Density profiles (*left*), dispersion profiles (*middle*), and median halo shapes (*right*) for SIDM with $\sigma/m = 1\text{cm}^2/\text{g}$ and its CDM counterpart. DM self-interactions cause heat transfer from the hot outer region to the cold inner region of a CDM halo and kinetically thermalize the inner halo, leading to a shallower density profile and a more spherical halo shape. Simulation data from [10, 11]. Reprinted from [7].

Reduced central density: Hierarchical structure formation leads to a universal density profile for CDM halos [59,60]. In the presence of collisions, the central density is reduced as low-entropy particles are heated within the dense inner halo, turning a cusp into a core.

Spherical halo shape: While CDM halos are triaxial [58], collisions isotropize DM particle velocities and tend to erase ellipticity. The minor-to-major axis ratio c/a is closer to unity toward the center of SIDM halos compared to CDM halos.

Since the scattering rate is proportional to the DM density, SIDM halos have the same structure as CDM halos at sufficiently large radii where the collision rate is negligible.

The local collision rate is given by

$$R_{\text{scat}} = \sigma v_{\text{rel}} \rho_{\text{DM}}/m \approx 0.1\text{Gyr}^{-1} \times (\frac{\rho_{\text{DM}}}{0.1\ \text{M}_\odot/\text{pc}^3})(\frac{v_{\text{rel}}}{50\ \text{km/s}})(\frac{\sigma/m}{1\ \text{cm}^2/\text{g}}) \tag{1.17}$$

,where m is the DM particle mass, while σ, v_{rel} are the cross section and relative velocity, respectively for scattering. Within the central region of a typical dwarf galaxy, we have

$\rho_{\rm DM} \sim 0.1~{\rm M}_\odot/{\rm pc}^3$ and $v_{\rm rel} \sim 50$ km/s [83]. Therefore, the cross section per unit mass must be at least

$$\sigma/m \sim 1~{\rm cm}^2/{\rm g} \approx 2 \times 10^{-24}~{\rm cm}^2/{\rm GeV} \tag{1.18}$$

to have an effect on the halo, corresponding to at least one scattering per particle over 10 Gyr galactic timescales. For $\sigma/m \sim 1~{\rm cm}^2/{\rm g}$, the mean free path of DM particles is larger than the core radii (Knudsen number larger than unity) and heat conduction is effective in the inner halo. Provided σ/m is not dramatically larger than this value, $R_{\rm scat}$ is negligible during the early Universe when structure forms. Therefore SIDM retains the success of large-scale structure formation from ΛCDM, affecting structure at late times and only on small scales in the dense inner regions of halos.

The figure of merit for self-interactions, σ/m, depends on the underlying DM particle physics model. WIMPs have self-interactions mediated through weak force, Higgs boson, or other heavy states. Since WIMP interactions and masses are set by the weak scale, yielding $\sigma/m \sim 10^{-38}~{\rm cm}^2/{\rm GeV}$, they effectively behave as collisionless CDM. if self-interactions indeed explain the small scale issues, then DM cannot be a usual WIMP.

An analogy for such large enough σ/m is provided by nuclear interactions, mediated by pion exchange. The required cross section for SIDM is comparable in magnitude to nuclear cross sections for visible matter. The lesson here is that $1~{\rm cm}^2/{\rm g}$ or larger can be achieved if the interaction scale lies below $\sim 1\,{\rm GeV}$. However, unlike the nuclear scattering, the theory of self-interactions need not be strongly-coupled, nor does the DM mass need to be below $1\,{\rm GeV}$. For example, self-interactions can be a weakly-coupled dark force [84–90]

, with the mediator particle denoted by ϕ. A perturbative calculation gives (in the limit $v_{\rm rel} = 0$)

$$\sigma/m = \frac{4\pi\alpha_d^2 m}{m_\phi^4} \approx 1\mathrm{cm}^2/\mathrm{g} \times (\frac{\alpha_d}{0.01})^2(\frac{m}{10\,\mathrm{GeV}})(\frac{m_\phi}{40\ \mathrm{MeV}})^{-4} \tag{1.19}$$

, where α_d is the DM analog of the electromagnetic fine structure constant, $\alpha_{\rm EM} \approx 1/137$. Self-interactions that are electromagnetic strength (or weaker) are sufficient, as are weak-scale DM masses, provided the mediator mass m_ϕ is light enough.

1.5 SIDM bound state production at LHC and lepton-jet signature

DM self-interactions can arise from a dark force mediator that is much lighter than the dark matter particle. In this case, when a pair of SIDM particles is produced at the LHC, they may form a bound state due to the same mediator that leads to dark matter self-interactions in the halos. The resulting bound state can annihilate into two boosted mediators, which subsequently decay back to the SM particles, as illustrated in figure 1.9. If the mediator's coupling to the SM is small enough to satisfy other existing constraints, it can be long-lived and have a macroscopic decay length which is comparable to the geometry of CMS detector.

The Lagrangian of SIDM where a fermionic dark matter particle χ couples to a dark photon Z_d with mass m_{Z_d} and kinetic mixing ϵ_{Z_d} to the SM photon [91–94] is

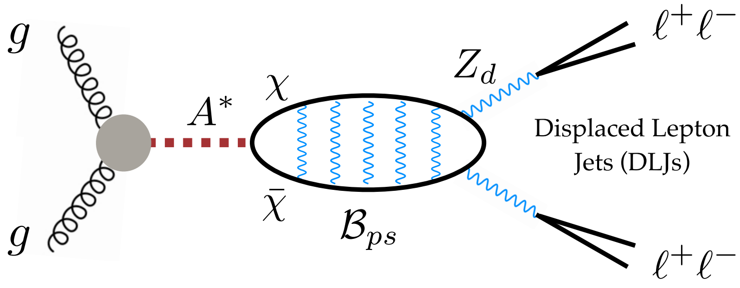

Figure 1.9: Displaced lepton-jet signatures from the SIDM bound state at the LHC. In the model, a heavy pseudoscalar (A^*) couples the SIDM particle (χ) to the gluon (g), a dark photon (Z_d) mediates dark matter self-interactions and leads to formation of the bound state ($\mathcal{B}_{ps}$). The boosted Z_d decays to SM charged leptons via a kinetic mixing portal. Reprinted from [12].

$$\mathcal{L}_{\text{SIDM}} = \bar{\chi}(i\partial\!\!\!/ + g_\chi Z\!\!\!/_d - m_\chi)\chi + \frac{m^2_{Z_d}}{2} Z_{d,\mu} Z^\mu_d + \frac{\epsilon_{Z_d}}{2} F_{\mu\nu} F^{\mu\nu}_d \tag{1.20}$$

[12]. The dark photon Z_d mediates dark matter self-interactions and bind dark matter particles into a bound state. The SIDM bound state decays dominantly into two dark photons, which can further decays into SM leptons via the kinetic mixing term. The decay length of Z_d in the lab frame is [12]

$$\begin{aligned} L_{Z_d \to l^+l^-} &= \gamma_{Z_d} \Big[\sum_l \frac{\alpha \epsilon^2_{Z_d} m_{Z_d}}{3} \sqrt{1 - \frac{4m_l^2}{m^2_{Z_d}}} (1 + \frac{2m_l^2}{m^2_{Z_d}})\Big]^{-1} \\ &\sim 1 \text{ m } (\frac{m_\chi}{10\,\text{GeV}})\ (\frac{10 \text{ MeV}}{m_{Z_d}})^2\ (\frac{10^{-4}}{\epsilon_{Z_d}})^2 \end{aligned} \tag{1.21}$$

, where $\gamma_{Z_d} \approx m_\chi / m_{Z_d}$ is the boost factor. The boosted Z_d from the $\mathcal{B}_{ps}$ decay can easily have a detector size lifetime, and the decay products $e^+e^-/\mu^+\mu^-$ can easily be within a cone of small opening angle $\Delta R \ll 0.5$ ($\Delta R \equiv \sqrt{\Delta\eta^2 + \Delta\phi^2}$, η is pseudorapidity (equation (2.6)), ϕ is azimuthal angle on the beam transverse plane). Thus, the dark photons from the dark matter bound state decay can be treated as displaced lepton-jets in the LHC search. In hadron collider experiments, related searches for dark photons were conducted by the CDF and D0 collaborations at the Tevatron [95–97], and by the CMS [98–101], ATLAS [102–107] and LHCb [108, 109] collaborations at the LHC.

For the collider study, s-wave production of a pseudoscalar bound state shown in figure 1.9 is focused. The Lagrangian of a heavy pseudoscalar A that couples the dark matter particle to the SM [110, 111].

$$\mathcal{L}_A \supset \frac{1}{2}(\partial A)^2 - \frac{m_A^2}{2}A^2 - iy_\chi A\bar{\chi}\gamma_5\chi - i\frac{y_q}{\sqrt{2}}\sum_f \frac{m_f}{v}A\bar{f}\gamma_5 f \tag{1.22}$$

, where $v = 174\,\text{GeV}$ and f represents the SM fermions. Although A can lead to dark matter-nucleus scattering, direct detection constraints on m_A are very weak because the cross section is either highly momentum or loop suppressed [112,113]. The pseudoscalar can be produced at the LHC through heavy quark and gluon fusion processes. The production cross section calculation is included in equation (2.7, 2.8) of [12]. Assuming the mass of the pseudoscalar $m_A = 450\,\text{GeV}$, $\alpha_\chi = 0.5$, $y_\chi = 1$ and $y_q = 1$, the cross section of DM bound state as a function of its mass is obtained as shown in figure 1.10.

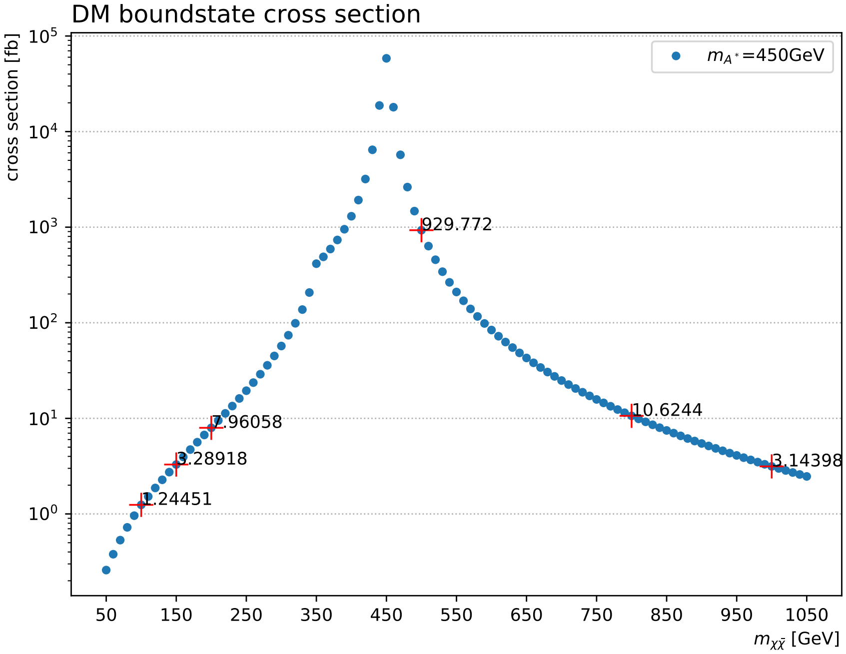

Figure 1.10: Dark matter bound state production cross section vs. mass. The mass of pseudoscalar A^* (mediator between dark matter χ and quark/gluon) is set as 450 GeV, $\alpha_\chi = 0.5$, $y_\chi = 1$ and $y_q = 1$. The signal samples used for the search in chapter 3 are generated at selected mass points marked by red crosses, with corresponding cross sections annotated.

Chapter 2

The Compact Muon Solenoid Detector at the Large Hadron Collider

The Compact Muon Solenoid (CMS) detector is a general purpose composite layer particle detector for measuring fundamental particles from proton-proton and heavy ion collisions on the Large Hadron Collider (LHC) at the European Organization for Nuclear Research (CERN). LHC makes two beams of high energy proton or heavy ion circulating around a 27.6 km tunnel in opposite directions and colliding at designated locations. The CMS is built to surround one of such interaction points.

2.1 The Large Hadron Collider

The LHC is the biggest and the most powerful particle collider human has ever built and still been under operation so far. It is a two-ring circular hadron collider designed to collide protons at a center-of-mass energy of $\sqrt{s} = 14\,\text{TeV}$ and instantaneous luminosity of $\mathcal{L} = 10^{34}\ \text{cm}^{-2}\text{s}^{-1}$ [114]. Since 2015, LHC has been operated to collide protons at a center-of-mass energy of $\sqrt{s} = 13\,\text{TeV}$, and remains this mode to present.

2.1.1 The Accelerator Chain and Beam Structure

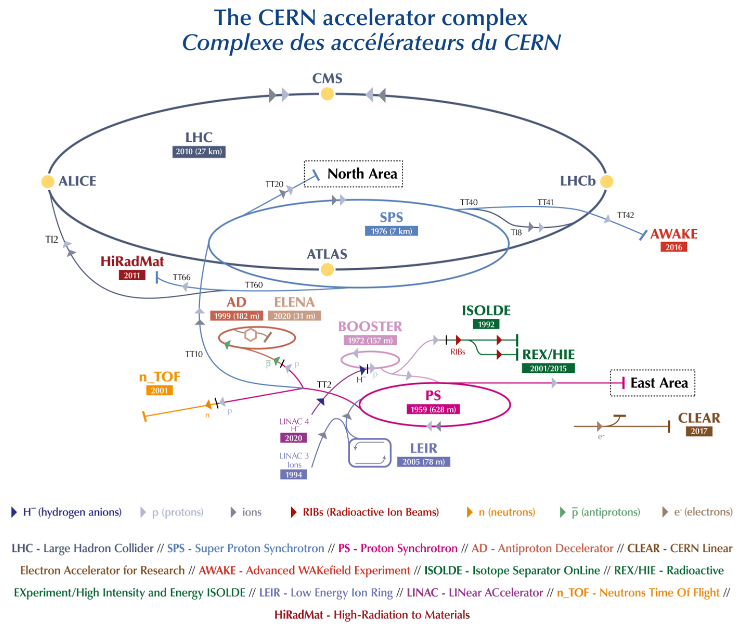

Figure 2.1: CERN accelerator complex diagram. Reprinted from [13].

The protons which collide in the CMS is not boosted from the rest to 13 TeV in one step. Instead, before entering into LHC, they have already traveled through an accelerator complex (figure 2.1) and LHC provides the very last gaint leap. The LHC tunnel has 8 arcs and 8 straight sections. Each straight section can serve as a location for experiments, while only 4 are used. The beam crossing happen at such four places, where four largest experiments are built. Two general purpose experiments, ATLAS and CMS, are located at Point 1 and Point 5 respectively. Two special purpose experiments, ALICE and LHCb are located at Point 2 and Point 8 respectively. Figure 2.2 summarizes the accelerator chain from the injection to the collision which the protons would go through. Starting from Linac2, which is a linear accelerator, the protons are subsequently injected into the Proton Synchrotron Booster (PSB), the Proton Synchrotron (PS), the Super Proton Synchrotron (SPS), and finally the LHC. It takes 12 cycles of the SPS and 3-4 cycles of the PS to fill the LHC, which leads to approximately 4 minutes per beam of a total LHC filling time.

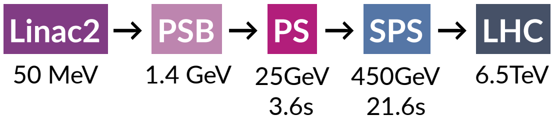

Figure 2.2: A simple diagram of proton injection chain, with designated energy protons are accelerated to at each stage. For PS and SPS, multiple cycles are required and the synchrotron cycle time are indicated also.

The proton beams in LHC are not continuous streams of protons, instead they are organized in the form of high-intensity bunches spaced 25 ns apart. The corresponding periodic frequency is 40 MHz. The LHC has 3564 bunch spaces, 2544 of them are filled with protons in colliding bunches. The consecutive bunches of protons are called trains, which are separated with empty filled bunches as gaps. Figure 2.3 shows a diagram of LHC beam bunch places represented by squares, the filled bunches are colored in blue.

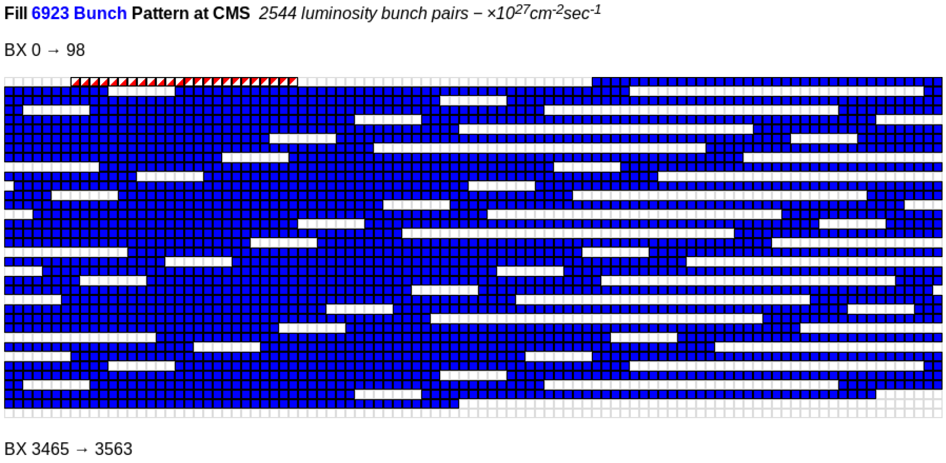

Figure 2.3: Diagram of the bunch spaces of an LHC proton beam, produced from Fill 6923 of the LHC on Jul.14-15, 2018 CEST. Each square represents a bunch. The square is colored in blue if it is filled, and left empty otherwise. In total, there is $26 \times 96 = 2564$ bunches.

2.1.2 RF Cavities and Steering Magnets

The protons are accelerated from the 450 GeV at SPS to 6.5 TeV at LHC by a system of 8 radio frequency (RF) cavities. These RF cavities oscillate at 400 MHz with the maximum amplitude of 2 MV. For one beam, they provide 16 MV to increase the proton energy by $\sim$ 0.5 MeV per revolution. The phase of the RF waveform is carefully modulated to create and maintain the bunch structure of protons, and to accelerate and maintain them at the desired energy. The RF cavity has a frequency of 400 MHz, dividing a bunch space into 10 RF buckets. The shape and size of the bucket are determined by the RF voltage amplitude and the number of bunch spaces. When coasting (at collision energy), a (hypothetical) particle is called a synchronous particle if the RF frequency happens to be exactly an integer multitude of the orbit frequency, and it is synchronized such that it passes the RF cavity at a time when the voltage within the RF waveform is exactly zero. Particles with different energy of arriving at a different timing with respect to the synchronous particle will encounter a non-zero voltage, and therefore will feel a restoring force. These particles will oscillate longitudinally around the synchronous particle. The size of a RF bucket is given as an area in energy-time phase space defined with respect to a synchronous particle. It is parametrized by the maximum energy deviation of a particle within a bunch with respect to the synchronous particle and the maximum arriving time deviation of a particle within a bunch with respect to the synchronous particle. The area of the bunch is called the longitudinal emittance with the unit of $\mathrm{eV} \cdot \mathrm{s}$.

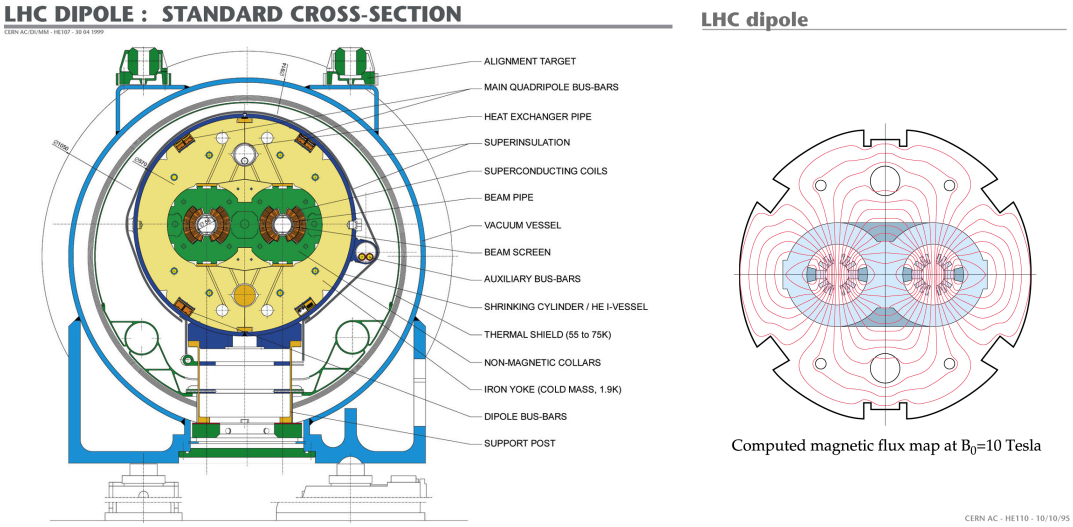

Figure 2.4: The cross section of LHC dipole magnet (*left*), reprinted from [14], and the depiction of the magnet lines inside the dipole (*right*), reprinted from [15].

Charged particles in the LHC are bent and squeezed by a total of 1232 superconducting dipole and quadrupole magnets. The superconductive winding in the magnets are made in niobium-titanium (NbTi), cooled by liquid helium to the operating temperature of 1.9 K to produce a magnetic field of 8.33 T. Figure 2.4 shows the cross section diagram of the LHC dipole magnet and the lines of magnetic field in the magnet dipole.

2.1.3 Instantaneous and Integrated Luminosity

The number of events generated by the LHC per second for a physics process with the cross section σ is

$$\frac{\mathrm{d}N}{\mathrm{d}t} = \mathcal{L}\sigma \tag{2.1}$$

, where $\mathcal{L}$ is the instantaneous luminosity, and depends on machine parameters only:

$$\mathcal{L} = \frac{N_p^2 N_b f \gamma}{4\pi\epsilon\beta^*} R \tag{2.2}$$

, where R is a geometrical factor accounting for the beam crossing angle,

$$\frac{1}{R} = \sqrt{1 + (\frac{\theta\sigma_z}{2\sigma^*})^2} \tag{2.3}$$

. The designed LHC beam parameters in equation (2.2), equation (2.3) are defined and summarized in table 2.1. The peak instantaneous luminosity under this configuration is $\mathcal{L} = 10^{34}\ \mathrm{cm}^{-2}\mathrm{s}^{-1}$.

Symbol	Name	Value
N_p	protons per bunch	1.15×10^{11}
N_b	bunches per beam	2544
f	revolution frequency (1/24.95 ns/3564)	11.25 kHz
γ	relativistic Lorentz factors for protons (E_p/m_p)	7461
ϵ	normalized transverse beam emittance	$3.75\ \mu m$
β^*	optical β function (amplitude of betatron oscillations)	55 cm
θ	beam crossing angle	285 μrad
σ_z	longitudinal RMS bunch length	7.55 cm
σ^*	transverse RMS beam size	$16.7\ \mu m$

Table 2.1: LHC nominal design beam parameters. From [24].

The collisions of protons lead to a natural decrease in luminosity over time. The integral of the instantaneous luminosity over time is called the integrated luminosity $\mathcal{L}_{\mathrm{int}}$.

The total number of events generated by the LHC for a given physics process with cross section σ is given by the product of the integrated luminosity and the cross section.

$$N = \sigma \mathcal{L}_{\text{int}} = \sigma \int \mathcal{L} dt \tag{2.4}$$

. The total integrated luminosity delivered by the LHC and recorded by the experiment is a measure of the number of total recorded events or the amount of data taken by the experiment, since the cross section of pp interactions remains constant. For convenience, the integrated luminosity is commonly expressed in the unit of inverse femto-barns:

$$1 \text{ fb}^{-1} = 10^{39} \text{ cm}^{-2} \tag{2.5}$$

Figure 2.5 presents the total integrated luminosity of pp collisions recorded by CMS over time for LHC Run 1 (2010-2012) and Run 2 (2015-2018). The analysis presented by this thesis is performed using data collected by the CMS experiment in 2018 that correspond to an integrated luminosity of 59.74 fb^{1}.

2.2 The Compact Muon Solenoid detector

2.2.1 Introduction

CMS is located at Point 5 of the LHC in Cessy, France, at the same level of the LHC beampipe, which is $\sim$ 100 m underground. Weight 14,000 tons, it has a cylindrical geometry with 15 m in diameter and 21.6 m in length. The heart of CMS is a powerful superconductive solenoid magnet surrounding the LHC beampipe symmetrically, providing

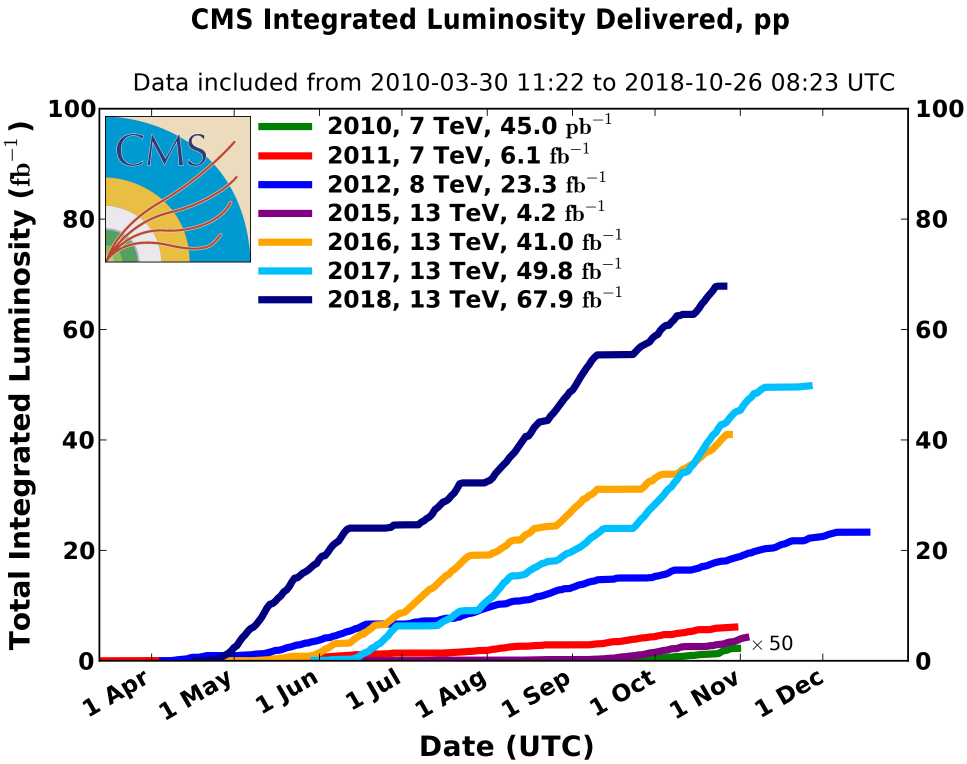

Figure 2.5: The cumulative integrated luminosity versus day delivered to CMS during stable beams for pp collisions at nominal center-of-mass energy. This is shown for data-taking in 2010 (green), 2011 (red), 2012 (blue), 2015 (purple), 2016 (orange), 2017 (light blue), and 2018 (navy blue). Reprinted from [16].

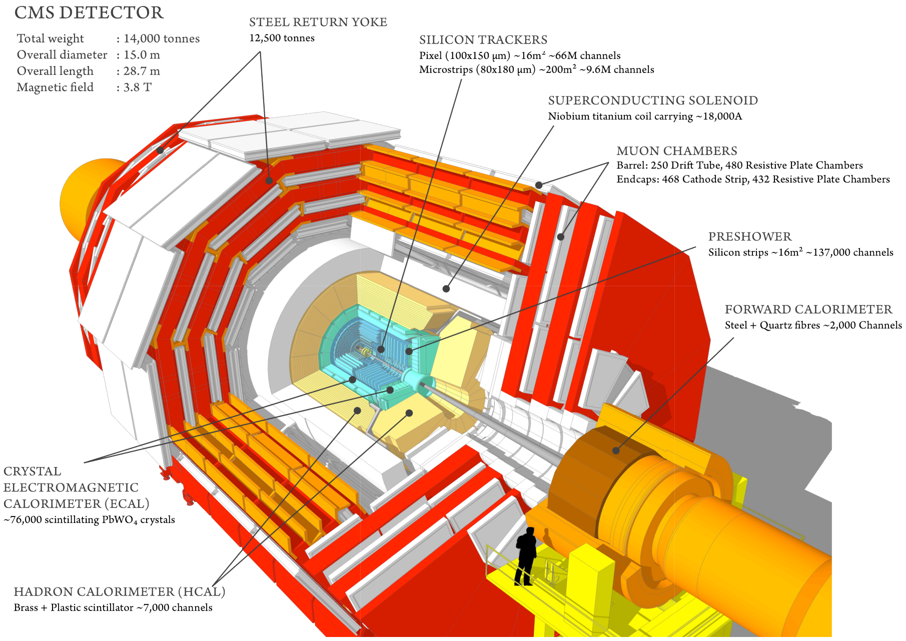

Figure 2.6: The layout of the CMS detector. Reprinted from [17].

a magnetic field of 3.8 T. The sub-detectors are placed in a layer structure, from inner to outer radically, as shown in figure 2.6. They are:

- silicon tracker
- electromagnetic calorimeter
- hadronic calorimeter
- solenoid magnet
- muon system

Figure 2.7 also indicates the detector signatures of particles that can be detected by CMS directly:

- electrons

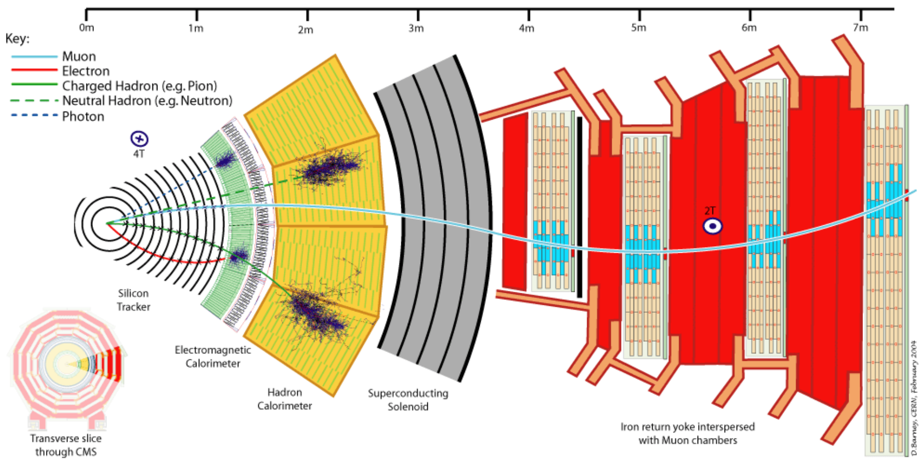

Figure 2.7: The transverse slice of the CMS detector, together with the 5 types of detectable particles and their signatures. Reprinted from [18].

- photons
- charged hadrons
- neutral hadrons
- muons

Charged particles – electrons, muons, charged hadrons – will leave helical traces in silicon tracker when they travel under the magnetic field. Electrons, photons and hadrons will deposit energy in electromagnetic and hadronic calorimeters.

2.2.2 Coordinate System

The coordinate system used for the descriptions of any CMS-related quantities is as following: the origin is set at the pp collision point. The y-axis is pointing upwards, the x-axis is pointing radically inwards towards the center of the LHC, the z-axis is pointing along

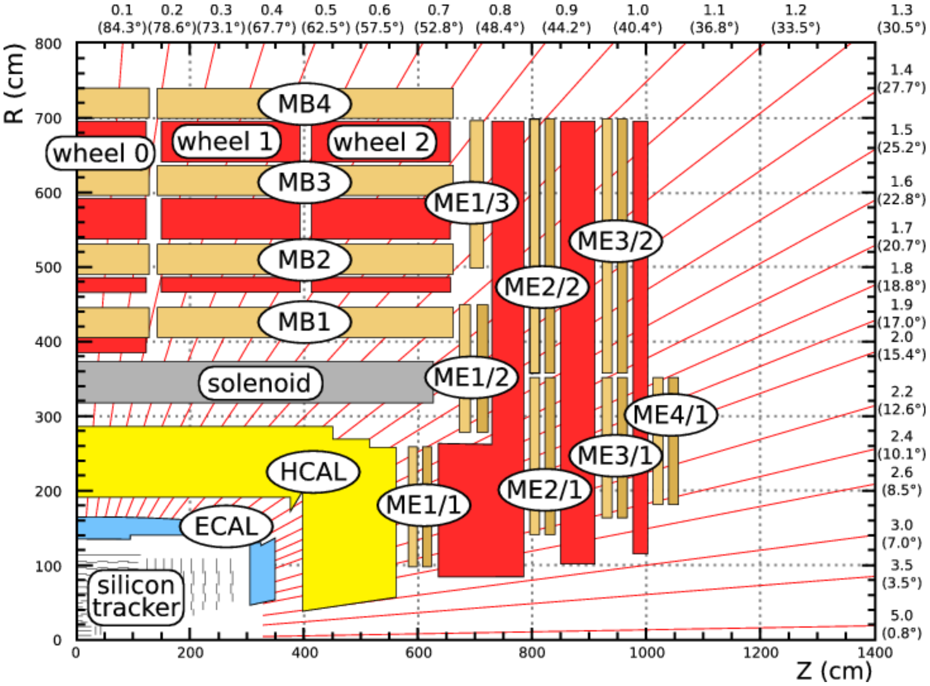

Figure 2.8: A quadrant of CMS in R-Z Cartesian coordinates together with θ, η mapping. Reprinted from [19].

the LHC beamline such that they form a right-handed coordinate system. The azimuthal angle ϕ is measured from the x-axis in the x-y plane and the polar angle θ is measured from the z-axis. The pseudorapidity η defined as

$$\eta = -\ln(\tan(\frac{\theta}{2})) \tag{2.6}$$

, which is commonly used to map the polar angle. The pseudorapidity has the advantage that it converges to rapidity (Lorentz-invariant along the z-axis) in high-velocity, low-mass limit ($|\mathbf{p}| \to E$), and depends only on the polar angle θ but not the energy of the particle. Figure 2.8 shows a quadrant of CMS in R-Z Cartesian coordinates together with θ, η mapping. As shown, $\eta = 0$ points upwards, $\eta \to \infty$ points along the z-axis, which is often referred to as high η or forward region.

2.2.3 Silicon Tracker

The inner tracking system provides precise measurements for trajectories of charged particles, which enables the reconstruction of secondary vertices of $\mathcal{O}(10^3)$ particles every 25 ns bunching crossing, while being exposed to the full flux radiation coming from high energy collisions from the LHC. To satisfy the harsh requirements on precision, speed and radiation-hardness, silicon technology was chosen to build the tracker. When charged particles travel through the dosed silicon material, electron-hole pairs will be created due to ionization and drift under the applied external voltage to form a current as a signal.

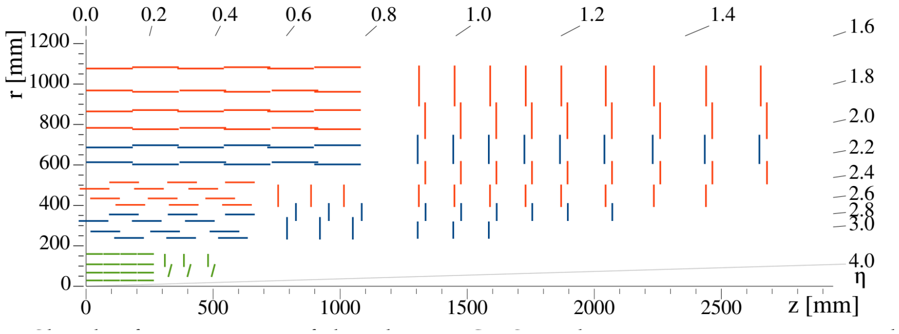

Figure 2.9: Sketch of one quarter of the Phase-1 CMS tracking system in r-z view. The pixel detector is shown in green, while single-sided and double-sided strip modules are depicted as red and blue segments, respectively. Reprinted from [20].

The CMS tracker makes use of two silicon detector technologies: pixel and strip. The pixel detector is the innermost sub-detector of CMS, sitting radically $2.9 - 16$ cm away from the LHC beam pipe. During 2016-17 extended year-end technical stop, CMS pixel detector underwent an upgrade. It is composed of 4 barrel layers and 3 endcaps at each side now, compared to 3 barrel layers and 2 endcaps at each side before the upgrade. In total, the number of pixels on silicon sensors is $\sim$ 124 million distributed across 1856 modules. The size of the pixel is 150×100 μm^2 with the thickness of 250 μm, providing the spatial resolution of $10 - 20$ μm, depending on η. The strip detector is located just outside of the pixel detector, at a radii from 20 to 110 cm. The size of each strip module is $10 - 25$ cm in length and $80 - 180$ μm in width, depending on the location of the module. In total, the number of strip sensors is ~ 9.6 million distributed across $15,148$ modules. The strip detector provides the spatial resolution of $20 - 40$ μm, depending on η. Together, the CMS tracker is capable to achieve 1% p_T resolution for 100 GeV charged particles, and it is the largest silicon detector in the world [20, 115].

2.2.4 Calorimeters

Calorimeters are destructive detectors which measure the incident particle's energy and position by absorbing all the energy of the particle. When the incoming particle interacts with the material of the calorimeter, the cascades of the secondary particles (particle showers) will be produced until all of them are stopped and absorbed by the material. To ensure maximum absorbance, calorimeters are made in dense material. The CMS calorimeters are composed by electromagnetic and hadronic calorimeters.

Electromagnetic calorimeter (ECAL) is a homogeneous calorimeter (single material serving as active and absorbing material at the same time) which consists of $\sim 76,000$ scintillating lead tungstate ($PbWO_4$) crystals – a material with high density and short radiation length. The radiation length of a material is defined as the mean length needed to reduce the energy of an electron by a factor of $1/e$ due to bremsstrahlung or $7/9$ of the mean free path for photon pair production in the material. It characterizes the longitudinal development of a electromagnetic shower. When electrons or photons passing through the scintillating crystals, a shower of particles with energy proportional to the energy of the incident particle will be developed. They will be measured by the photodetectors installed on each crystal to determine the energy of the incident particle. ECAL is crucial to the discovery of the SM Higgs boson in di-photon channel $H \to \gamma\gamma$ [116].

Hadronic calorimeter (HCAL) is a sampling calorimeter (made of repeating layers of absorbing and active material, the shower energy is measured using the active material) which consists of brass and plastic tiles. The HCAL has four parts: barrel (HB), endcaps (HE), outer (HO) and forward (HF). Brass is a dense material with short nuclear interaction length, which is defined as the mean length needed to reduce the energy of a hadron by a fraction of $1/e$. The interaction length characterizes the longitudinal development of a hadronic shower. Brass has a radiation length of 1.5 cm and an interaction length of 16.4 cm. The total absorber thickness is 5.6 interaction lengths at small $|\eta|$ and increases to 10.3 with increasing $|\eta|$. HB and HE are placed inside the magnet, while HO is placed outside of the magnet, built to detect the energy of showers that leak out of the back of HB. The HO uses the magnet as the absorbing medium and plastic tiles as scintillator, extending the total absorber thickness in the barrel region to 10 interaction lengths.

The HF is located 11 m from the interaction point, covering pseudorapidity range $3 < |\eta| < 5$. This forward region is exposed to high dose of LHC radiation and is thus constructed with radiation-hard materials: steel for absorber and quartz fiber for active material, which detects Cherenkov radiation produced by the energetic jets [117].

2.2.5 Solenoid Magnet

As mentioned above, CMS uses a superconductive solenoid magnet. It is 12.5 m in length and 6.3 m in inner diameter. The magnet is cooled by liquid helium to 4 K. It draws 19 kA current and is the largest magnet in the world in terms of 2.6 GJ stored energy.

The magnetic field is introduced to measure the transverse momentum of the charged particles. To illustrate, consider a particle charge q and transverse momentum p_{T} in an uniform magnetic field B in z-direction. It will travel in a helix with radius $R = p_{\mathrm{T}}/qB$. The radius of the curvature is proportional to particle's p_{T}. However, what is being measured is the position of hits whose resolution functions are Gaussian. Consider an arc left by a charged particle in a magnetic field, let L be the length of the chord connecting the outermost points, s be the sagitta, the distance between the midpoint of the chord and the center of the arc. Then the curvature R can be expressed in terms of L and s as

$$R = \frac{L^2}{8s} + \frac{s}{2} \approx \frac{L^2}{8s} \tag{2.7}$$

Since s is typically small when compared to L, $s/2$ term can be dropped. Then

$$\frac{q}{p_{\mathrm{T}}} = \frac{1}{BR} \approx \frac{8s}{BL^2} \tag{2.8}$$

As s is linear in the position measurement, its distribution is also Gaussian. Therefore, it is the distribution of q/p_{T}, not p_{T}, is Gaussian. The uncertainty of the measurement of p_{T} that obtained from applying the standard error propagation to q/p_{T} must therefore be considered carefully, as it does not describe standard deviations of a variable distributed as a Gaussian.

2.2.6 Muon System

Muons are elementary particles very similar to electrons but ~ 207 times heavier. Due to the mass, muon bremsstrahlung is heavily suppressed compared to electrons, therefore muons mainly interact with the detector through ionization and can penetrate the CMS calorimeter with very little energy loss. For this reason, muon detectors are placed outermost, outside the magnet. Muon's momentum can be measured with the 1.8 T magnetic field in the return yolk of the magnet. The algorithm used to measure the muon momentum in the muon chambers is similar to the algorithm used for the tracker. The best muon momentum resolution is mostly obtained by combining tracks in the muon system and the silicon tracker.

CMS muon system has 3 tasks: triggering, muon identification, and muon reconstruction. As with other subsystems, the shape of the solenoid informs a design of a cylindrical barrel section and two endcap disk sections. Both barrel and endcap sections consist of 4 stations of muon detectors, concentric for the barrel and sequential for the endcaps. The muon system is composed by 3 kinds of gaseous ionization detectors: drift tubes (DT), cathode strip chambers (CSC), and resistive plate chambers (RPC).

Drift Tubes The barrel muon system consists of 4 stations instrumented with 250 drift tube chambers. Drift tubes were chosen to be the tracking detectors in the barrel region because of the low expected rate and relatively low intensity of local magnetic field. A cathode tube with cross-sectional dimensions 42×13 mm^2 contains an anode wire under tension. The anode wire is operated at 3600 V. The tube is filled with a gas mixture of 85% Ar and 15% CO_2. When an energetic muon travels through the cell, the gas will be ionized to produce electrons drifting towards the wire. The measurement of the drift time (maximum 380 ns) will give the position within the cell.

The most basic independent unit of DT is a superlayer (SL), which consist of 4 layers of drift cells staggered by a half cell. A DT chamber consists of 3 (or 2) SLs. The wires in the two outer SLs are parallel to the beam line, and provide a location measurement in the $r-\phi$ plane. The wires in the inner SL are orthogonal to the beam line, and provide a location measurement along the z axis. The inner SL is not present in the 4th (outermost) muon station, which therefore provides measurement of ϕ coordinate only.

Cathode Strip Chambers The endcap muon system consists of 4 stations instrumented with 540 cathode strip chambers. Cathode strip chambers were chosen to be the tracking detector in the endcap region because of the excellent position resolution in ϕ direction achieved by precision cathode charge readout and interpolation. The CSCs are arranged in circular disks. Each CSC consists of 6 layers, each layer lying in an $r-\phi$ plane of CMS, consisting of a gas mixture of 50% CO_2, 40% Ar, and 10% CF_4 in between a plane of copper cathode strips and a plane of anode wires, which are operated at $2900-3600$ V. When an energetic muon travels through a CSC, the gas will be ionized to produce electrons drifting towards the wires, causing a charge avalanche that induces an opposite charge on the cathode strips. The interpolation of theses charges will give a precise location of the avalanche.

Resistive Plate Chambers Resistive plate chambers interspread throughout both barrel and endcap muon system. In total, there are 480 and 576 RPCs correspondingly, providing fast timing response and comparable resolution with respect to the scintillators.

Because of this, RPCs are important components for dedicated muon trigger which identifies muon tracks and assigns bunch crossing with high efficiency. An RPC consists of 2 parallel plates of phenolic resin coated with conductive graphite, with a 2 mm gap filled with a gas mixture of 95.2% freon ($C_2H_2F_4$), 3.5% isobutane (i-C_4H_{10}), and 0.3% sulfur hexafluoride (SF_6). When an energetic muon travels through a chamber, the ionized gas will produce an image charge which is sampled and read out. RPCs have a timing resolution of $\sim$ 2 ns, which is much shorter than 25 ns between LHC bunch crossings. But RPC's spatial resolution is coarser compared to DTs and CSCs.

2.2.7 Trigger System

At designed luminosity, the rate of proton-proton collision at LHC exceeds 1 GHz. As each recorded event occupies $\sim$ 1 Mb storage space, it is not realistic to save every event for later processing. However, only a small fraction of total events are of interest to CMS physics program, therefore CMS employs a sophisticated trigger system which identifies interesting events for later processing at runtime. In such way, the rate of events needs to be recorded is reduced to a manageable level for tape writting.

CMS trigger system is two-tiered, including a Level-1 Trigger (L1T) and a high level trigger (HLT). A schematic view is shown in figure 2.10. The L1T makes decisions at the hardware level with custom-built programmable electronics, synchronously with the LHC, and is designed to reduce the event rate from 40 MHz to 100 kHz. The HLT makes decisions at the software level by performing computations at the full rate of LHC in real time, using a processor farm located on the surface of Point5. The processing time per

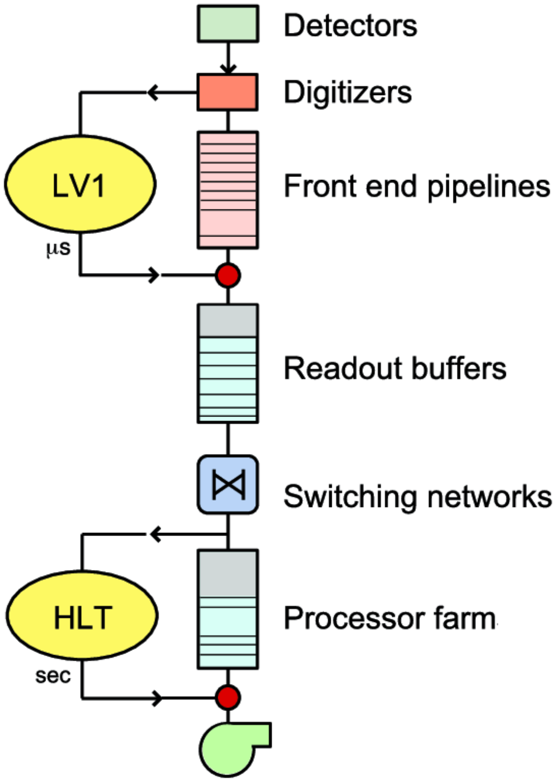

Figure 2.10: Schematic view of CMS two-tiered trigger system.

event is longer for HLT with respect to L1T, but still faster than reading out total events at full rate. By design, HLT will reduce the event rate from 100 kHz to hundreds of Hz.

The L1T consists of two components: calorimeter trigger and muon trigger. They are organized into local, regional and global components. Both ECAL and HCAL participate in the calorimeter trigger; all muon chambers, DT, CSC and RPC, participate in the muon trigger. The local components are the lowest level, based on energy deposits in the calorimeters and hits and segments in the muon system. The regional components combine the information collected from the local components to build trigger objects with pattern recognition and track finding in small regions, and assigning them ranks. The global com-

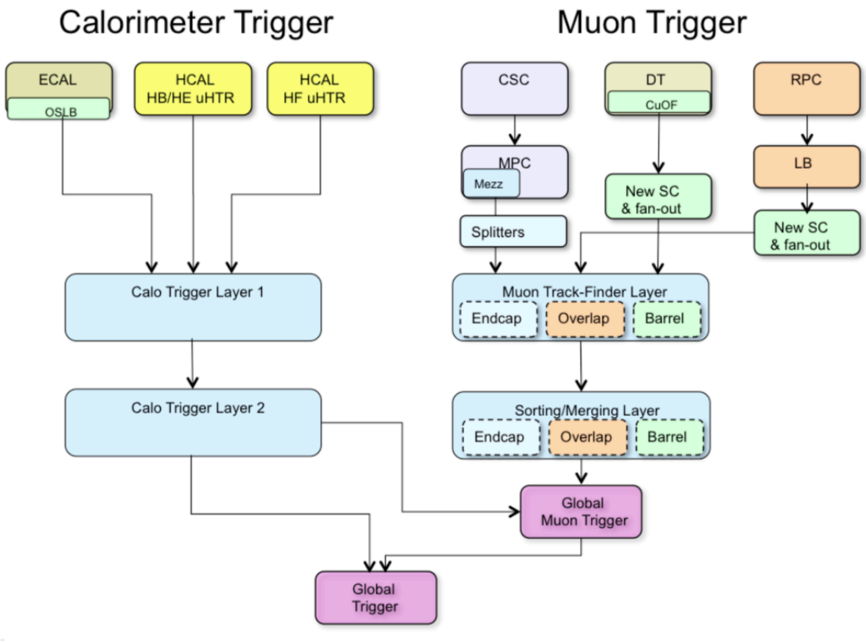

Figure 2.11: Schematic view of CMS Level-1 Trigger system. Reprinted from [21].

ponents determine the trigger objects with highest ranks and transfer them to the global trigger of L1T, which issues a decision on whether to reject or accept the event at Level-1. A Level-1 Accept (L1A) decision is passed to all subsystems and the event will be passed to HLT for further evaluation. The fact that L1T needs to analyze each bunch crossing limits the maximum latency of L1T processing to 3.2 μs.

The L1T and HLT menus consists of *paths* which define the criteria under what conditions the trigger would fire. These criteria are the first step for most physics analysis, if not all. They include requirements on p_{T}, number of objects (muons, jets, etc.), pseudorapidities $|\eta|$, relative distances between objects and so on. The HLT uses information collected from all subsystems and analyzes them with sophisticated algorithms which are very similar to the ones use for offline reconstruction. Therefore, the decision from HLT is more precise than from L1T. Each HLT path is seeded by one or more L1T objects, and is designed to be inclusive and general while maintain the total trigger rate within the maximum limit which the data acquisition system can endure.

2.2.8 Offline Computing System

The CMS computing infrastructure consists of dozens of computing centers distributed around the globe organized in a tiered structure. The central computing center is located at CERN, named as Tier-0. There are 8 large computing centers located at various places named as Tier-1, and more than 50 smaller scale Tier-2 and Tier-3 centers worldwide. The Tier-0 receives the data of event accepted by HLT in `RAW` format, which contains low-levels signals from sub-detectors, and performs prompt event reconstruction (RECO). The `RECO` format includes more high-level reconstructed objects. The RAW and RECO datasets are transferred to various Tier-1 centers for permanent storage. The copies of data in Tier-1 centers are transferred to Tier-2 centers so that analyzers/physicists from anywhere can access them more easily. For the convenience of data analysis, Analysis Object Data (`AOD`) data format was developed as a slimmed version of `RECO` dataset. It contains pre-computed higher level data and drops low-level detector signal at the same time, therefore save the additional computing time and storage requirements. Since Run2, CMS has developed even slimmer data format called `MiniAOD` and `NanoAOD`. They drop more low-level information about the event (with reduced numerical precision for `NanoAOD`) to save more storage space and preserve commonly used pre-computed values to reduce computing time to cope with the increasing amount of data needed to process and the frequency of reprocessing. Tier-2 and Tier-3 centers are also used for the production and storage of the Monte Carlo simulated events.

The software used by CMS is maintained in a softare framework named as `CMSSW` (CMS SoftWare). `CMSSW` is written in C++ with modular design, and used for event reconstruction, simulation, detector calibration and data analysis. It's a framework integrated with many external open source software. The data preservation is based on `ROOT` [118] data analysis framework. Users/analyzers can create independent plugin modules with configuration files in Python programming language to accomplish their analysis tasks.

Chapter 3

Search for Self-interacting Dark Matter (SIDM) with Two Displaced Lepton-jets

This chapter presents a search of SIDM with two displaced lepton-jets final state at CMS detector with data collected in 2018 at center-of-mass energy $\sqrt{s} = 13\,\text{TeV}$ corresponding to 59.74fb^{-1} of integrated luminosity during Run 2 of LHC. Lepton-jets are striking experimental signatures where one or more lepton pairs are collimated in a narrow cone. They are mostly theorized as the decay signatures of *dark photon*, which is a spin-1 gauge boson in dark sector with kinetic mixing with SM photons. The search is focused on two lepton-jets event topology, and interpreted in the context of SIDM model introduced in Chapter 1. While the lepton-jet reconstruction and the analysis procedures are meant to be more inclusive and model-independent.

3.1 Simulation, Dataset and Triggers

3.1.1 Simulation

The essential task of the search can be simplified as testing the non-null signal hypothesis by comparing the observation with the predictions. The predictions can come from either data or simulations. The simulation starts from theoretical calculations and includes production of particles and their detector response when they pass through the material of the CMS detector. Because the Monte Carlo method is used to model the stochastic effects at each stage of the simulation, the result of the total process is commonly referred to as "MC simulation". In this analysis, both simulations of signal and background processes are used for studies. In the end the prediction is from data, the simulations of background processes are however used to make selection cuts and gain insights. In the following of this section, some details about the signal and background simulations used in the analysis are described.

Signal Simulation

The SIDM model is implemented with MadGraph5_aMC@NLO v2.6.0 [119] at leading order with free model parameters including mass of DM bound state $m_{\chi\bar{\chi}}$, mass of dark photon m_{Z_d}, and dark photon's kinetic mixing coupling ϵ_{Z_d}. In the model, the production of pseudo-scalar bound state is focused by considering a pseudo-scalar particle A^* that mediates the DM-SM coupling. For the calculation of bound state production, it is assumed that the pseudo-scalar coupling $y_q = y_\chi = 1$, also $\alpha_\chi = g_\chi^2/4\pi = 0.5$. We fix the mass of the pseudo-scalar m_{A^*} as 450 GeV, which is the best existing constraint coming from the CMS mono-jet search [120]. The generated parton level events are further showered with PYTHIA v8.230 [121], before passing to GEANT4 [122–124]-based CMS detector simulation of particle-material interactions. The pileup collisions (multiple collisions within the same bunch crossing) are simulated and overlapped on top of the main collision to mimic realistic proton proton bunch collisions. The decay length of dark photon Z_d in the lab frame can be calculated from equation (1.21).

$m_{\chi\bar{\chi}}$ [GeV]	m_{Z_d} [GeV]	$c\tau$ [mm]				
100	0.25	0.02	0.2	2	10	20
	1.2	0.096	0.96	9.6	48	96
	5	0.4	4	40	200	400
150	0.25	0.013	0.13	1.3	6.7	13
	1.2	0.064	0.64	6.4	32	64
	5	0.27	2.7	27	130	270
200	0.25	0.01	0.1	1	5	10
	1.2	0.048	0.48	4.8	24	48
	5	0.2	2	20	100	200
500	0.25	0.004	0.04	0.4	2	4
	1.2	0.019	0.19	1.9	9.6	19
	5	0.08	0.8	8	40	80
800	0.25	0.0025	0.025	0.25	1.2	2.5
	1.2	0.012	0.12	1.2	6	12
	5	0.05	0.5	5	25	50
1000	0.25	0.002	0.02	0.2	1	2
	1.2	0.0096	0.096	0.96	4.8	9.6
	5	0.04	0.4	4	20	40
lxy		0.3 cm	3 cm	30 cm	150 cm	300 cm

Table 3.1: Signal parameter grid

We scan DM bound state masses from 100 GeV up to 1000 GeV on 6 points, and dark photon mass of 0.25 GeV, 1.2 GeV and 5 GeV with several lifetime settings such that the mean flight distances in lab frame correspond to $0.3, 3, 30, 150, 300\,\mathrm{cm}$. Table 3.1 shows the parameter grid with all possible combinations. We allow one of the two dark photons decay to muon pairs $Z_d \to \mu^+\mu^-$, the other one decays to either a muon pair or an electron pair $Z_d \to \mu^+\mu^-(e^+e^-)$. This results in two search channels: channel 4μ and channel $2\mu 2e$. The decay branch ratio of dark photon is plotted as a function of its mass in figure 3.1.

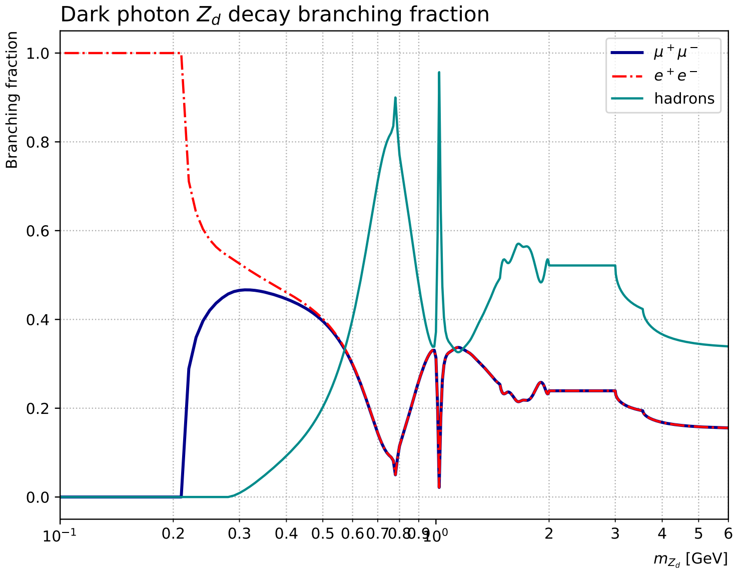

Figure 3.1: Dark photon decay branching fraction. Reproduced from [22].

To save the computing resources and storage for signal sample generation, a few kinematic cuts were applied at the generator level to filter only events that will enter the acceptance of the detector. The filters requires all 4 final state leptons to meet the following criteria:

- $p_{\mathrm{T}} > 5\,\mathrm{GeV}$
- $|\eta| < 2.4$
- $V_{\mathrm{xy}} < 740\,\mathrm{cm}$ && $V_{\mathrm{z}} < 960\,\mathrm{cm}$

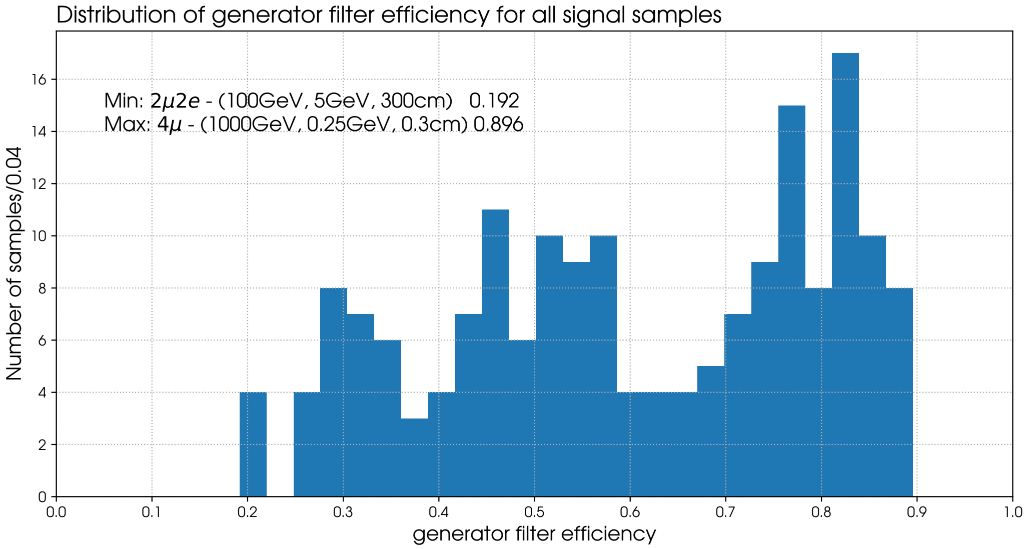

Figure 3.2: The generator filter (defined above) efficiencies for simulated SIDM samples. The samples with the minimum and the maximum efficiencies are annotated in the plot, with the sample parameter in ($m_{\chi\bar{\chi}}$, m_{Z_d}, $L_{\rm xy}$) form.

Such cuts result in various generator level filter efficiencies from $\sim 20-90\%$, which can be understood as a minimal acceptance. Figure 3.2 displays the distribution of the generator filter efficiencies obtained from all signal samples in the following table 3.2. All the signal samples with the listed parameter settings in both channels are produced by CMS Monte Carlo sample generation infrastructure in `RunIIAutumn18` campaign. The dataset names are listed in table 3.2. Each sample is asked to generate $\sim$ 100 k events.

Generator level signal distributions

This section contains several distributions which demonstrate the kinematic features of SIDM model. They are obtained from the simulated samples which are listed in table 3.2.

Dataset name	# events
/SIDM_XXTo2ATo{4Mu, 2Mu2E}_mXX-100_mA-0p25_ctau-{0p02, 0p2, 2, 10, 20}_TuneCP5_13TeV-madgraph-pythia8	~ 100 k
/SIDM_XXTo2ATo{4Mu, 2Mu2E}_mXX-100_mA-1p2_ctau-{0p096, 0p96, 9p6, 48, 96}_TuneCP5_13TeV-madgraph-pythia8	~ 100 k
/SIDM_XXTo2ATo{4Mu, 2Mu2E}_mXX-100_mA-5_ctau-{0p4, 4, 40, 200, 400}_TuneCP5_13TeV-madgraph-pythia8	~ 100 k
/SIDM_XXTo2ATo{4Mu, 2Mu2E}_mXX-150_mA-0p25_ctau-{0p013, 0p13, 1p3, 6p7, 13}_TuneCP5_13TeV-madgraph-pythia8	~ 100 k
/SIDM_XXTo2ATo{4Mu, 2Mu2E}_mXX-150_mA-1p2_ctau-{0p064, 0p64, 6p4, 32, 64}_TuneCP5_13TeV-madgraph-pythia8	~ 100 k
/SIDM_XXTo2ATo{4Mu, 2Mu2E}_mXX-150_mA-5_ctau-{0p27, 2p7, 27, 130, 270}_TuneCP5_13TeV-madgraph-pythia8	~ 100 k
/SIDM_XXTo2ATo{4Mu, 2Mu2E}_mXX-200_mA-0p25_ctau-{0p01, 0p1, 1, 5, 10}_TuneCP5_13TeV-madgraph-pythia8	~ 100 k
/SIDM_XXTo2ATo{4Mu, 2Mu2E}_mXX-200_mA-1p2_ctau-{0p048, 0p48, 4p8, 24, 48}_TuneCP5_13TeV-madgraph-pythia8	~ 100 k
/SIDM_XXTo2ATo{4Mu, 2Mu2E}_mXX-200_mA-5_ctau-{0p2, 2, 20, 100, 200}_TuneCP5_13TeV-madgraph-pythia8	~ 100 k
/SIDM_XXTo2ATo{4Mu, 2Mu2E}_mXX-500_mA-0p25_ctau-{0p004, 0p04, 0p4, 2, 4}_TuneCP5_13TeV-madgraph-pythia8	~ 100 k
/SIDM_XXTo2ATo{4Mu, 2Mu2E}_mXX-500_mA-1p2_ctau-{0p019, 0p19, 1p9, 9p6, 19}_TuneCP5_13TeV-madgraph-pythia8	~ 100 k
/SIDM_XXTo2ATo{4Mu, 2Mu2E}_mXX-500_mA-5_ctau-{0p08, 0p8, 8, 40, 80}_TuneCP5_13TeV-madgraph-pythia8	~ 100 k
/SIDM_XXTo2ATo{4Mu, 2Mu2E}_mXX-800_mA-0p25_ctau-{0p0025, 0p025, 0p25, 1p2, 2p5}_TuneCP5_13TeV-madgraph-pythia8	~ 100 k
/SIDM_XXTo2ATo{4Mu, 2Mu2E}_mXX-800_mA-1p2_ctau-{0p012, 0p12, 1p2, 6, 12}_TuneCP5_13TeV-madgraph-pythia8	~ 100 k
/SIDM_XXTo2ATo{4Mu, 2Mu2E}_mXX-800_mA-5_ctau-{0p05, 0p5, 5, 25, 50}_TuneCP5_13TeV-madgraph-pythia8	~ 100 k
/SIDM_XXTo2ATo{4Mu, 2Mu2E}_mXX-1000_mA-0p25_ctau-{0p002, 0p02, 0p2, 1, 2}_TuneCP5_13TeV-madgraph-pythia8	~ 100 k
/SIDM_XXTo2ATo{4Mu, 2Mu2E}_mXX-1000_mA-1p2_ctau-{0p0096, 0p096, 0p96, 4p8, 9p6}_TuneCP5_13TeV-madgraph-pythia8	~ 100 k
/SIDM_XXTo2ATo{4Mu, 2Mu2E}_mXX-1000_mA-5_ctau-{0p04, 0p4, 4, 20, 40}_TuneCP5_13TeV-madgraph-pythia8	~ 100 k

Table 3.2: SIDM MC datasets

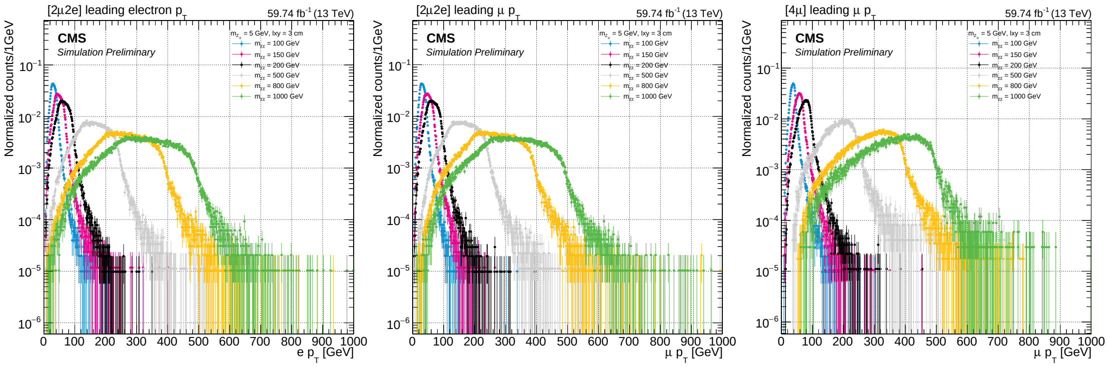

Figure 3.3: Leading lepton p_T of SIDM signal. *Left*: leading electron p_T for channel $2\mu 2e$; *Middle*: leading muon p_T for channel $2\mu 2e$; *Right*: leading muon p_T for channel 4μ. The dark photon's mass and transverse decay length are kept fixed at 5 GeV and 3 cm, respectively. The distributions from different bound state masses are normalized to unity.

Figure 3.3 shows the distributions of the leading lepton p_{T} for both search channels.

Figure 3.4 shows the distribution of ΔR between the lepton pairs for both search channels.

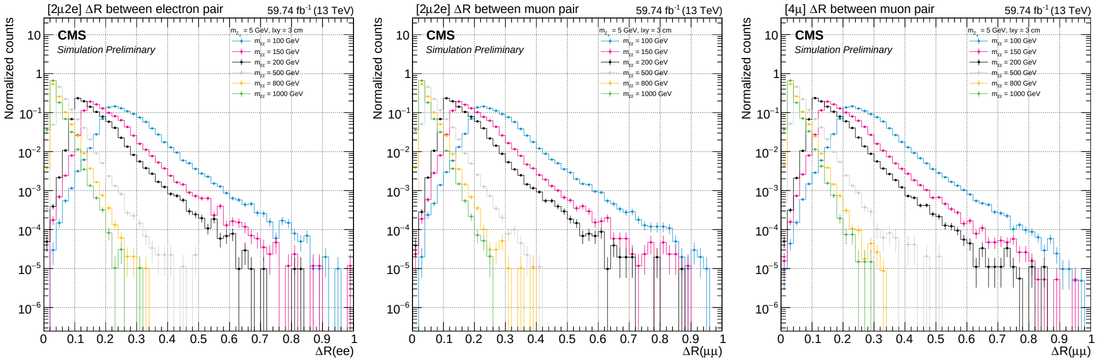

Figure 3.4: ΔR between lepton pairs in SIDM signals. *Left*: $\Delta R(e^+e^-)$ for channel $2\mu 2e$; *Middle*: $\Delta R(\mu^+\mu^-)$ for channel $2\mu 2e$; *Right*: $\Delta R(\mu^+\mu^-)$ for channel 4μ. The dark photon's mass and transverse decay length are kept fixed at 5 GeV and 3 cm, respectively. The distributions from different bound state masses are normalized to unity.

Fig. 3.5 shows the distribution of the azimuthal separation $|\Delta\phi|$ between the dark photon pair for both search channels.

Figure 3.6 shows the distribution of the transverse decay length of dark photons for both search channels.

Background Simulation

The main background are coming from SM events giving muons, including QCD process where B hadrons decay-in-flight, Drell-Yan process giving $\mu^+\mu^-$ and top quark events where μ comes from B meson decay in the hadronizatino of b quark. The probability of which two real muons are close-by may not be necessarily high, however, there are

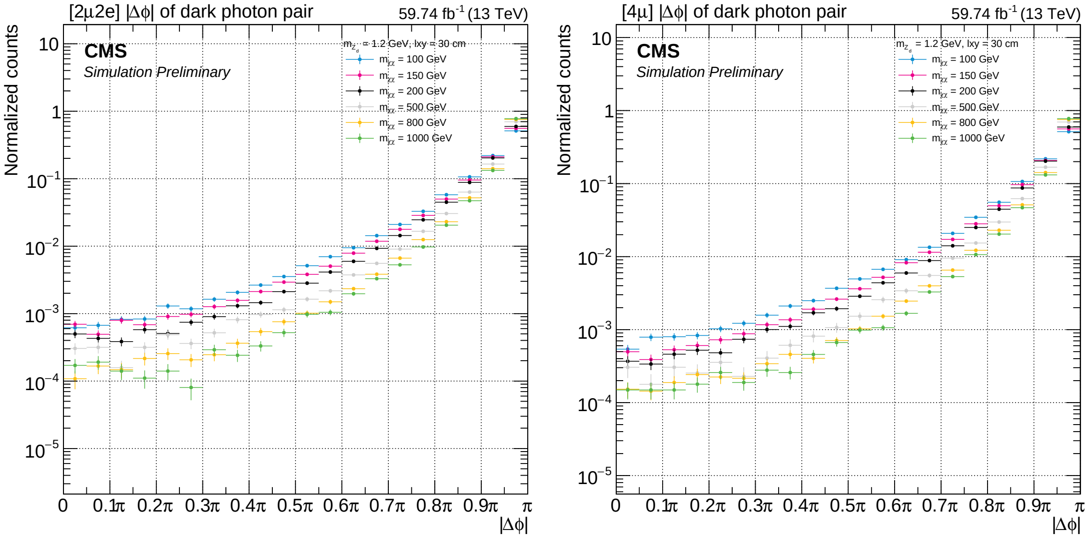

Figure 3.5: $|\Delta\phi|$ between the dark photon pair in the SIDM signal. *Left*: channel $2\mu 2e$; *Right*: channel 4μ. The dark photon's mass and transverse decay length are kept fixed at 5 GeV and 3 cm, respectively. The distributions from different bound state masses are normalized to unity.

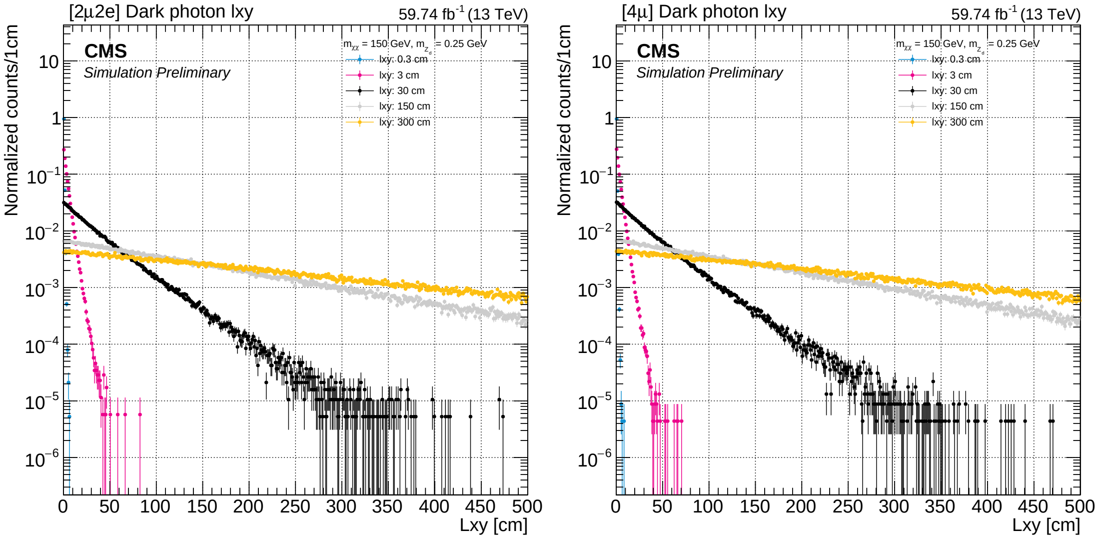

Figure 3.6: The transverse decay length L_{xy} of dark photons in SIDM signal. *Left*: channel $2\mu 2e$; *Right*: channel 4μ. The bound state's mass and the dark photon's mass are kept fixed at 150 GeV and 0.25 GeV, respectively. The distributions from different dark photon lifetimes are normalized to unity.

often cases where a fake muon from reconstruction mistakes (muon track splitting) pass the selection. Other backgrounds do not contribute significantly to the analysis. As stated above, the background MC are not used for the actual prediction but mainly used for getting insight of background source composition and the understanding of distributions. All background samples are produced by CMS Monte Carlo sample generation infrastructure under `RunIIAutumn18` campaign. The dataset names and corresponding cross sections at $\sqrt{s} = 13$TeV are listed in Table.3.3.

Dataset	σ **[pb]**
/TTJets_TuneCP5_13TeV-madgraphMLM-pythia8	491
/DYJetsToLL_M-10to50_TuneCP5_13TeV-madgraphMLM-pythia8	15820
/DYJetsToLL_M-50_TuneCP5_13TeV-madgraphMLM-pythia8	5317
/WW_TuneCP5_13TeV-pythia8	75.91
/WZ_TuneCP5_13TeV-pythia8	27.55
/ZZ_TuneCP5_13TeV-pythia8	12.14
/QCD_Pt-15to20_MuEnrichedPt5_TuneCP5_13TeV_pythia8	2805000
/QCD_Pt-20to30_MuEnrichedPt5_TuneCP5_13TeV_pythia8	2536000
/QCD_Pt-30to50_MuEnrichedPt5_TuneCP5_13TeV_pythia8	1375000
/QCD_Pt-50to80_MuEnrichedPt5_TuneCP5_13TeV_pythia8	377900
/QCD_Pt-80to120_MuEnrichedPt5_TuneCP5_13TeV_pythia8	89730
/QCD_Pt-120to170_MuEnrichedPt5_TuneCP5_13TeV_pythia8	21410
/QCD_Pt-170to300_MuEnrichedPt5_TuneCP5_13TeV_pythia8	7022
/QCD_Pt-300to470_MuEnrichedPt5_TuneCP5_13TeV_pythia8	619.8
/QCD_Pt-470to600_MuEnrichedPt5_TuneCP5_13TeV_pythia8	59.32
/QCD_Pt-600to800_MuEnrichedPt5_TuneCP5_13TeV_pythia8	18.19
/QCD_Pt-800to1000_MuEnrichedPt5_TuneCP5_13TeV_pythia8	3.271
/QCD_Pt-1000toInf_MuEnrichedPt5_TuneCP5_13TeV_pythia8	1.08
/WJetsToLNu_HT-100To200_TuneCP5_13TeV-madgraphMLM-pythia8	1395
/WJetsToLNu_HT-200To400_TuneCP5_13TeV-madgraphMLM-pythia8	407.9
/WJetsToLNu_HT-400To600_TuneCP5_13TeV-madgraphMLM-pythia8	57.48
/WJetsToLNu_HT-600To800_TuneCP5_13TeV-madgraphMLM-pythia8	12.87
/WJetsToLNu_HT-800To1200_TuneCP5_13TeV-madgraphMLM-pythia8	5.366
/WJetsToLNu_HT-1200To2500_TuneCP5_13TeV-madgraphMLM-pythia8	1.074
/WJetsToLNu_HT-2500ToInf_TuneCP5_13TeV-madgraphMLM-pythia8	0.008001

Table 3.3: Background MC datasets

The simulation of the hard process including matrix elements calculation is performed by MadGraph5_aMC@NLO v2.4.2 for $t\bar{t}$+jets, Drell-Yan ($Z/\gamma^* \to ll$) and W+jets samples. Simulations of parton showering and hadronization are performed by PYTHIA 8 v8.230 using CP5 tune [125] in all signal and background samples.

3.1.2 Dataset

This analysis is performed with the certified events collected by CMS detector during full 2018 run period of proton-proton collisions, corresponding to 59.74 fb^{-1}. The dataset names and the associated information is present in table 3.4. In CMS, the collected data are grouped in several "primary datasets" featured by interesting objects in the events that fire the trigger. We use `DoubleMuon` primary dataset since at least two muons are present in final state particles of signal events. A JSON file in table 3.5 is used to filter runs when the detector was in good data-taking condition.

Dataset	$\mathcal{L}$ [fb^{-1}]	Run range
/DoubleMuon/Run2018A-17Sep2018-v2/AOD	14.219	315257-316995
/DoubleMuon/Run2018B-17Sep2018-v1/AOD	6.874	317080-319310
/DoubleMuon/Run2018C-17Sep2018-v1/AOD	6.616	319337-320065
/DoubleMuon/Run2018D-PromptReco-v2/AOD	32.723	320500-325175

Table 3.4: 2018 `DoubleMuon` datasets.

JSON
Cert_314472-325175_13TeV_17SeptEarlyReReco2018ABC_PromptEraD_Collisions18_JSON.txt

Table 3.5: JSON file of certified events for 2018 dataset

Global tags

For CMS MC and data sample production, global tags are used to define a range of conditions which will be input for data reconstruction and analysis, such as the jet energy correction payload, alignment and calibration parameters for several sub-detectors, etc. Table 3.6 summarizes the global tags used in relevant samples for this analysis.

Data	MC
102X_dataRun2_v12 (era ABC) 102X_dataRun2_Prompt_v15 (era D)	102X_upgrade2018_realistic_v20

Table 3.6: Global tags used for 2018 data and MC analysis. This follows the analysis setup recommendations from the CMS PdmV (physics data mc validation) group [25].

3.1.3 Triggers

The majority of lepton triggers in the CMS Run2 trigger menu include a beamspot constraint, which requires the leptons to be consistent with being produced at the beamspot. Due to the macroscopic decay length of dark photons in signal events, we need to rely on lepton triggers without such constraint. Before the start of 2018 data-taking, a set double muon HLT paths without a beamspot constraint were renovated and brought online. These triggers use the **NoVtx** algorithm (table 3.8) and require two standalone muons which are reconstructed with segments built in muon chamber only, without tracker information (**L2Mu** in HLT terminology). The beamspot constraint was removed from the seeding and fitting steps. The lowest muon p_{T} threshold for the trigger is 23 GeV, the maximum $|\eta|$ value is 2.4. Some of the triggers utilize the "cosmic seed" seeding the muon reconstruction, which was originally developed for cosmic muon reconstruction and does not include a beamspot constraint. The L1 seeds used by the triggers are listed in table 3.9. The `L1_SingleMu22` seed was added to two of the HLT paths in order to mitigate the rapid efficiency loss with the increasing displacement at L1. This analysis uses the logical "OR" of the HLT paths in table 3.7.

path	comments
`HLT_DoubleL2Mu23NoVtx_2Cha`	-
`HLT_DoubleL2Mu23NoVtx_2Cha_NoL2Matched`	OR `L1_SingleMu22`
`HLT_DoubleL2Mu23NoVtx_2Cha_CosmicSeed`	cosmic seeding*
`HLT_DoubleL2Mu23NoVtx_2Cha_CosmicSeed_NoL2Matched`	OR `L1_SingleMu22`; cosmic seeding
`HLT_DoubleL2Mu25NoVtx_2Cha_Eta2p4`	$p_{\mathrm{T}} > 25\mathrm{GeV}$; $\lvert\eta\rvert < 2.4$
`HLT_DoubleL2Mu25NoVtx_2Cha_CosmicSeed_Eta2p4`	$p_{\mathrm{T}} > 25\mathrm{GeV}$; $\lvert\eta\rvert < 2.4$; cosmic seeding

Table 3.7: HLT Trigger paths used by the analysis.

name	criteria
N(L2 muons)	$\geqslant 2$
p_{T}	$>$ XX GeV
$\lvert\eta\rvert$	< 2
N(chambers)	$\geqslant 2$
beamspot constraint	No

Table 3.8: Common definition of `DoubleL2MuXXNoVtx_2Cha`

name
`L1_DoubleMu_12_5`
OR `L1_DoubleMu_15_5_SQ`
OR `L1_DoubleMu_15_7`
OR `L1_TripleMu_5_3_3`

Table 3.9: Common L1 seeds of `DoubleL2MuXXNoVtx_2Cha`

3.2 Lepton-jet Reconstruction

The dark photons in our signal events are *displaced* (due to small kinetic mix coupling ϵ_{Z_d}) and *boosted* (because a heavy resonance $\chi\bar{\chi}$ decays to two low-mass dark photons). This section describes the reconstruction used to identify this challenging dark matter signature.

In CMS, particle flow (PF) reconstruction algorithm [26] is currently the de facto event reconstruction used by most analysis, the output of this algorithm is referred to as “PFCandidates”. Because the dark photons are displaced, we cannot fully rely on the usual PFCandiates (PFMuons and PFElectrons) since both of them depend on the result of the interative track building proceduce (more desciption below). For displaced muons, when the dark photons decays beyond the range of iterative tracking, we rely on the dedicated “displacedStandAlone” (DSA) reconstruction algorithm that builds muons from segments in the muon chamber only.

In the remaining of this section, we will overview particle flow algorithm used in CMS first, and bring up the key points of the dedicated displaced muon reconstruction, discuss about the identification choices we made for both PFCandidates and DSAs.

3.2.1 Particle Flow Reconstruction Algorithm in CMS

As described in section 2.2, CMS is composed of multiple layers of subdetectors around the beampipe and interaction point in a cylindrical structure. Each subdetector is designed to make measurements for a specific type or category of experimental signature. Such design leads to a tradition of physics objects based signal reconstruction: jets consists of hadrons and photons, whose energy can be inclusively measured by calorimeters; isolated photons and electrons are primarily reconstructed by electromagnetic calorimeter; muons are measured by muon detectors. The power of particle flow and the improvements it brings in reside on the correlations among more basic elements to identify each final state particle and evaluate their properties based on the combination of the measurements.

The basic particle flow elements include trajectories of charged particles and calorimeter clusters. Tracks are reconstructed with a combinatorial track finder based on kalman-filtering: seed generation with a few hits compatible with a charged-particle trajectory, trajectory building by gathering hits from all tracker layers along propagation under magnetic field, and final fitting to determine track's properties (origin, direction and transverse momentum). To increase the tracking efficiency while maintaining the misreconstruction rate at a low level, several successive iterations are applied with the combinatorial track finder, known as "iterative tracking". The hits associated with selected tracks in previous iterations are masked, the seeding and trajectory building make use of the remaining hits with more relaxed quality criteria, which results in the increased total tracking efficiency without degrading the purity. There are some special treatments for electron and muon track reconstruction. For electrons, due to tracker material, most of the electrons will emit a sizeable fraction of their energy in the form of bremsstrahlung photons before reaching ECAL. When energetic photons radiated, the trajectory building with kalman filter may not be able to accommodate the change in electron momentum, causing the track to be reconstructed with a small number of hits. The Gaussian-sum filter (GSF) is more adapted to electrons as it allows for sudden and substantial energy loss along the trajectory. For muons, both tracks reconstructed by the inner tracker and the muon spectrometer outside the magnet are considered and combined to provide a final track for a muon. The energy deposits in calorimeter are clustered separately in each subdetector: ECAL barrel and endcaps, HCAL barrel and endcaps, and the two preshower layers. The clustering happens in two steps: seeding and cluster growing. First, seeds are identified as cells with energy larger than a given threshold and energy of neighbouring cells. Second, topological clusters are grown from the seed by aggregating cells with at least one corner in common and whose energy higher than the threshold set as twice the noise level. An expectation-maximization algorithm based on a Gaussian-mixture model is then used to reconstruct the clusters within a topological cluster. To maximize the probability of identifying neutral particles while minimizing the rate of misreconstructed energy excess, particle flow also calibrate the calorimeter response to photons and hadrons based on result from testbeam data, radioactive sources and cosmic ray measurements firstly, and initial collision data later on.

Iteration	Name	Seeding	Targeted Tracks
1	InitialStep	pixel triplets	prompt, high p_T
2	DetachedTriplet	pixel triplets	from b hadron decays, $R \leqslant 5\,\mathrm{cm}$
3	LowPtTriplet	pixel triplets	prompt, low p_T
4	PixelPair	pixel pairs	recover high p_T
5	MixedTriplet	pixel+strip triplets	displaced, $R \leqslant 7\,\mathrm{cm}$
6	PixelLess	strip triplets/pairs	very displaced, $R \leqslant 25\,\mathrm{cm}$
7	TobTec	strip triplets/pairs	very displaced, $R \leqslant 60\,\mathrm{cm}$
8	JetCoreRegional	pixel+strip pairs	inside high p_T jets
9	MuonSeededInOut	muon-tagged tracks	muons
10	MuonSeededOutIn	muon detectors	muons

Table 3.10: Iterative tracking seeding configurations and targeted tracks. From [26].

With basic elements at hand, a link algorithm is used to connect these pieces into blocks, laying out the foundation of building final state particles. To avoid quadratically growing computation time, the elements considered by the link procedure are restricted to the nearest neighbour in the (η, ϕ) plane, as obtained with a k-dimensional tree. If two elements are linked, a distance is defined to quantify the quality of the linking. The output of linking are PF blocks which are elements associated by a direct link or an indirect link through common elements. Concretely, a link can be established between a track and a calorimeter cluster, between calorimeter cluster and cluster, among charged particle tracks via a common secondary vertex, and between tracks built by inner tracker and segments built by muon spectrometer. When multiple elements can be linked to a common element, the link is set to the combination with the smallest distance. In each PF block, the identification and reconstruction proceed in orders: First, muon candidates are identified and reconstructed, the corresponding PF elements are removed from PF block. Electron candidates, energetic and isolated photons are identified and reconstructed next, the corresponding tracks and clusters are excluded for further consideration. The remaining elements in the block are subject to cross identifications of charged hadrons, neutral hadrons and photons coming from parton fragmentation, hadronization and decays in jets.

Muons Isolated global muons are first selected by an isolation criterion which requires the p_{T} sum of tracks and E_{T} sum of energy deposits within distance $\Delta R = 0.3$ to muon direction in (η, ϕ) plane not exceeding 10% of the muon p_{T}. For non-isolated global muons, the tight-muon selection is applied, additionally, it is required at least three matching segments found from muon chambers, or calorimeter deposits associated with the track compatible with muon hypothesis. Muons failed tight-muon selection may be kept if its standalone muon track has good quality or the inner track has a high quality fit. After the charged hadron identification (in a later step), muon identification criteria may be revisited with looser criteria if there are elements left.

Electrons, isolated photons In a given PF block, electron candidate is seeded from a GSF track, provided that the associated ECAL cluster is not linked with three or more additional tracks. A photon candidate is seeded from an ECAL supercluster with E_T greater than 10 GeV, with no links to a GSF track. For ECAL-based electron candidates and photon candidates, small energy deposit sum ($\leqslant 10\%$) is required for HCAL cells under the projection of ECAL supercluster. The corrections of ECAL clusters are applied as a function of energy and pseudorapidity to account for the missing energy in the association process. The energy of photon candidates are assigned with this correction and the direction is taken from the supercluster. The energy of electron candidates are assigned by combining the corrected ECAL energy and the GSF track's momentum, the direction is taken from the GSF track.

Hadrons, non-isolated photons After muons, electrons and isolated photons are identified and removed from PF blocks, what remains to be identified are hadrons from jet fragmentation and hadronization. Calorimeter clusters not linked to any tracks will yield photons and neutral hadrons. Within tracker acceptance ($|\eta| \leqslant 2.4$), all ECAL clusters are turned into photons and all HCAL clusters are turned into neutral hadrons. Outside the tracker acceptance, as charged hadrons cannot be distinguished from neutral hadrons, ECAL clusters which are linked with an HCAL cluster are assumed from the same hadron shower and those who are not are turned into photons.

It's worth noting both muon candidates and electron candidates (PFMuons and PFElectrons) depends on the result of iterative tracking. Even though it's very efficient, iterative tracking does not account for highly displaced tracks. Its power is limited up to mid range of barrel tracker, as shown in the iterative seeding configuration table 3.10. For displaced di-electron in the signal, when GSF tracks are not reconstructed, the energy deposit at ECAL will be identified and reconstructed as photon candidates. For displaced di-muon in the signal, when dark photon decays beyond the range where iterative tracking would generate seeds, or tracks failed to be reconstructed inside inner tracker, we consider the dedicated displaced muon reconstruction in CMS as described below.

3.2.2 Displaced Standalone Muon (DSA) Reconstruction in CMS

The global muon reconstruction algorithm used by CMS is optimized for prompt muons, it matches segments in the muon chambers with an inner track in the inner tracker. For displaced muons without an inner track, this analysis uses the DSA muon reconstruction that was developed in CMS before the start of Run 2. The DSA reconstruction follows the same three steps as track building inside the silicon tracker: seed generation, trajectory building, and final fit. Typically, a seed is composed of a state vector (track position, momentum and errors) with a few hits or segments in the DT or CSC, and the parametrization of the state vector involves the interaction point. The DSA algorithm uses the cosmic muon seeding requirement, which differs from the typical seeding in the following ways [126,127]:

- Each seed contains exactly one DT or CSC segment.
- Segment with larger $|y|$ value is preferred.
- State vector direction taken from the segment direction, the parametrization exludes the involvement of the interaction point.

- The momentum of the seed is set downwards.

The Kalman Filter algorithm is used to build the muon trajectory from the cosmic seeds, and afterwards a final fit is performed without the knowledge of the beamspot to avoid bias.

3.2.3 Identification of Lepton-jet Source Candidates

A set of identification criteria are applied to select candidates used as input for the lepton-jet clustering: PFElectrons, PFPhotons, PFMuons, and DSA muons. For PFElectrons, PFPhotons and PFMuons, we use the centrally provided POG IDs in this first-round analysis. For DSA muons, we employ a custom ID and a custom procedure to match DSA muons with PFMuons to avoid duplicate counting.

Electrons

We consider electrons that pass cut-based *loose* ID, which has an average efficiency of $\sim 90\%$ [128]. The variables used for the electron ID include:

- $\sigma_{i\eta i\eta}$: shower shape variable, defined as the energy-weighted standard deviation of a single crystal eta within the 5×5 crystals centered at the crystal with maximum energy.
$$\sigma^2_{i\eta i\eta} = \frac{\sum_i^{5\times5} w_i (i\eta_i - i\eta_{\text{seed}})^2}{\sum_i^{5\times5} w_i}, \quad w_i = \max(0, 4.7 + \ln\frac{E_i}{E_{5\times5}}) \tag{3.1}$$
- $|\Delta\eta_{\text{seed}}|$: tracking based variable, $|\Delta\eta|$ between GSF track and supercluster seed.
- $|\Delta\phi_{\text{in}}|$: tracking based variable, $|\Delta\phi|$ between GSF track and supercluster.

- *H/E*: ratio of the energy deposited in the single closest HCAL tower to the supercluster position inside a cone of $\Delta R = 0.15$ in the (η, ϕ) plane to the energy deposited at ECAL.
- *Isolation*: relative isolation value with effective area corrections. It is calculated by considering all PFCandidates whose distance to the electron in question satisfies $\Delta R < 0.3$ in the (η, ϕ) plane:

  $$\mathrm{Iso} = (\mathrm{Iso}_{\mathrm{ch}} + \mathrm{Iso}_{\mathrm{nh}} + \mathrm{Iso}_{\mathrm{pho}})/p_{\mathrm{T}} \tag{3.2}$$

  , where $\mathrm{Iso}_{\mathrm{ch}}$ is the p_{T} sum of charged hadrons, and $\mathrm{Iso}_{\mathrm{nh}}$ and $\mathrm{Iso}_{\mathrm{pho}}$ are the E_{T} sum of neutral hadrons and photons. Contributions from pileup interactions are estimated by the product of ρ and the effective area and subtracted from each type of isolation such that after the correction, $\mathrm{Iso}_{\mathrm{xx}} = \max(0.0, \mathrm{Iso}_{\mathrm{xx}} - \mathrm{PU})$. ρ is the event-specific average pileup density per unit area in the (η, ϕ) plane, and the effective areas are derived centrally for each type of isolation.
- $|\frac{1}{E} - \frac{1}{p}|$: absolute value of the difference between the ECAL supercluster energy inverse and the GSF track momentum inverse.
- *Expected missing inner hits*: number of missing hits expected for GSF track.
- *Conversion veto*: veto designed to identify electrons from photon conversions.

Additionally, electrons are required to have $p_{\mathrm{T}} > 10\,\mathrm{GeV}$ and $|\eta| < 2.4$.

	superCluster $\lvert\eta\rvert \leqslant 1.479$	superCluster $\lvert\eta\rvert > 1.479$
$\sigma_{i\eta i\eta}(\text{full5} \times 5) <$	0.0112	0.0425
$\lvert\Delta\eta_{\text{seed}}\rvert <$	0.00377	0.00674
$\lvert\Delta\phi_{\text{in}}\rvert <$	0.0884	0.169
H/E$<$	$0.05 + 1.16/E_{\text{SC}} + 0.0324\rho/E_{\text{SC}}$	$0.0441 + 2.54/E_{\text{SC}} + 0.183\rho/E_{\text{SC}}$
relIsoWithEA $<$	$0.112 + 0.506/p_{\text{T}}$	$0.108 + 0.963/p_{\text{T}}$
$\lvert\frac{1}{E} - \frac{1}{p}\rvert <$	0.193	0.111
expected missing inner hits $\leqslant$	1	1
pass conversion veto	yes	yes

Table 3.11: Electron cut-based *loose* ID criteria (V2). The corresponding tag in CMSSW is `egmGsfElectronIDs:cutBasedElectronID-Fall17-94X-V2-loose`.

Photons

We consider photons that pass the cut-based *loose* ID, which has an average efficiency of $\sim 90\%$ [129]. The variables used for the photon ID include:

- *H/E*: same variable used for electron ID.
- $\sigma_{i\eta i\eta}$: same variable used for electron ID.
- *Rho corrected PF charged hadron isolation*: Iso_{ch} in electron ID with ρ correction applied.
- *Rho corrected PF neutral hadron isolation*: Iso_{nh} in electron ID with ρ correction applied.
- *Rho corrected PF photon isolation*: Iso_{pho} in electron ID with ρ correction applied.

	superCluster $\lvert\eta\rvert \leqslant 1.479$	superCluster $\lvert\eta\rvert > 1.479$
H/E $<$	0.04596	0.0590
$\sigma_{i\eta i\eta} <$	0.0106	0.0272
ρ-corrected PF charged hadron Iso $<$	1.694	2.089
ρ-corrected PF neutral hadron Iso $<$	$24.032 + 0.01512 p_{\text{T}} + 0.00002259 p_{\text{T}}^2$	$19.722 + 0.0117 p_{\text{T}} + 0.000023 p_{\text{T}}^2$
ρ-corrected PF photon Iso $<$	$2.876 + 0.004017 p_{\text{T}}$	$4.162 + 0.0037 p_{\text{T}}$

Table 3.12: Photon cut-based *loose* ID criteria (V2). The corresponding tag in CMSSW is `egmPhotonIDs:cutBasedPhotonID-Fall17-94X-V2-loose`.

The exact cut values used in the photon ID are listed in table 3.12. The PF isolation variables in table 3.12 are computed by:

$$\text{corrected PFIso} = \max(\text{PFIso} - \rho \times \text{EA}, 0.0) \tag{3.3}$$

, where EA stands for Effective Area, which is given as a function of photon $|\eta|$. The EA value used for the corresponding tag is shown in table 3.13.

	EA		
eta range	charged hadrons	neutral hadrons	photons
$|\eta| < 1.0$	0.0112	0.0668	0.1113
$1.0 < |\eta| < 1.479$	0.0108	0.1054	0.0953
$1.479 < |\eta| < 2.0$	0.0106	0.0786	0.0619
$2.0 < |\eta| < 2.2$	0.01002	0.0233	0.0837
$2.2 < |\eta| < 2.3$	0.0098	0.0078	0.1070
$2.3 < |\eta| < 2.4$	0.0089	0.0028	0.1212
$|\eta| > 2.4$	0.0087	0.0137	0.1466

Table 3.13: Effective Area (EA) used for photon ρ-corrected PF isolation calculation for 2018 conditions.

Additionally, photons are required to have $p_{\mathrm{T}} > 20\,\mathrm{GeV}$ and $|\eta| < 2.4$.

PF Muons

We consider muons that pass the cut-based *loose* ID [130]. The criteria includes:

- Identified as a muon by PF algorithm.
- Reconstructed either as a global muon or as an arbitrated tracker muon.

Additionally, PF muons are required to have $p_{\mathrm{T}} > 5\,\mathrm{GeV}$ and $|\eta| < 2.4$.

DSA Muons

The identification of DSA muons starts with the multiplicities of hits and segments used to build muon tracks and the transverse momentum uncertainty:

- *Number of DT or CSC stations with segments*: N(DT+CSC) stations $\geqslant 2$.
- *Number of hits in DT or CSC*: N(DT+CSC) hits > 12.
- $\sigma_{p_{\mathrm{T}}}/p_{\mathrm{T}} < 1$

Then the overlap between DSA and loose PF muons are removed with the following checks:

- The ratio of common segments associated with the DSA muon in question and any loose PFMuon must always be smaller than 0.66.
- Each loose PFMuon is extrapolated to the surface containing the innermost hit of the DSA muon in question. The distance between the extrapolated point on the surface and the DSA muon's innermost hit in the (η, ϕ) plane must satisfy $\Delta R > 0.2$.
- The subdetectors providing segments for the DSA muon in question should not be a subset of the subdetectors providing segments for any loose PFMuons.

Finally, DSA muons passing the above overlap checks need to satisfy the following additional requirements:

- $p_{\mathrm{T}} > 10\,\mathrm{GeV}$
- $|\eta| < 2.4$
- $\chi^2/\mathrm{ndof} < 4$

- N(DT) hits > 18 (out of 32 when passing all 4 DT chambers) when N(CSC) hits is 0.

The effect of the ID cuts applied for DSA muons are shown with several N-1 style plots. Figure 3.7 and figure 3.8 show distributions of the DSA muon p_{T} resolution for the 4μ signal sample with $m_{\chi\bar{\chi}} = 500\,\mathrm{GeV}$, $m_{Z_d} = 1.2\,\mathrm{GeV}$, and lxy $= 300\,\mathrm{cm}$ for events split up by the N(DT+CSC) stations cut, the N(DT+CSC) hits cut, the $\sigma_{p_{\mathrm{T}}}/p_{\mathrm{T}}$ cut, the χ^2/ndof cut and the N(DT) hits when N(CSC) hits=0 cut. Each population is normalized to unit area. The events satisfying the cuts have reasonable p_{T} resolution, while the events failing the cut have rather poor p_{T} resolution.

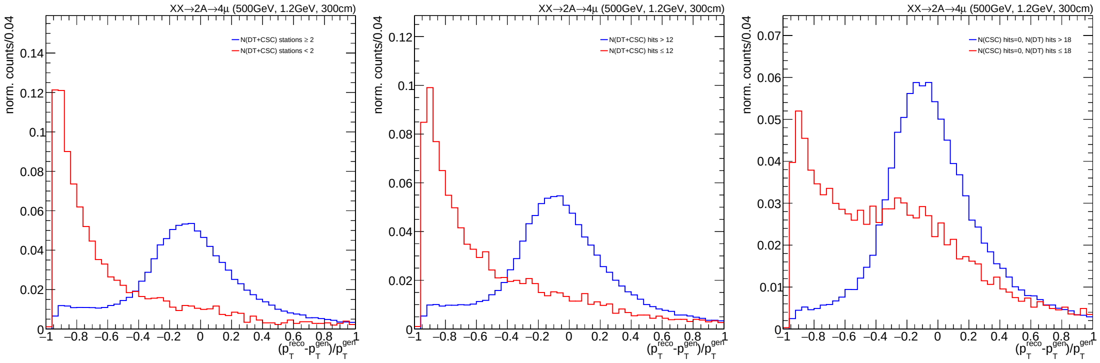

Figure 3.7: DSA muon p_{T} resolution, normalized to unit area, for the 4μ signal sample with $m_{\chi\bar{\chi}} = 500\,\mathrm{GeV}$, $m_{Z_d} = 1.2\,\mathrm{GeV}$, and lxy $= 300\,\mathrm{cm}$ for events with N(DT+CSC) stations $\geqslant$2 and $<$2 separately (*left*), events with N(DT+CSC) hits $>$12 and $\leqslant$12 (*middle*) and events with N(CSC) hits $= 0$ and N(DT) hits $>$18 or $\leqslant$18 (*right*).

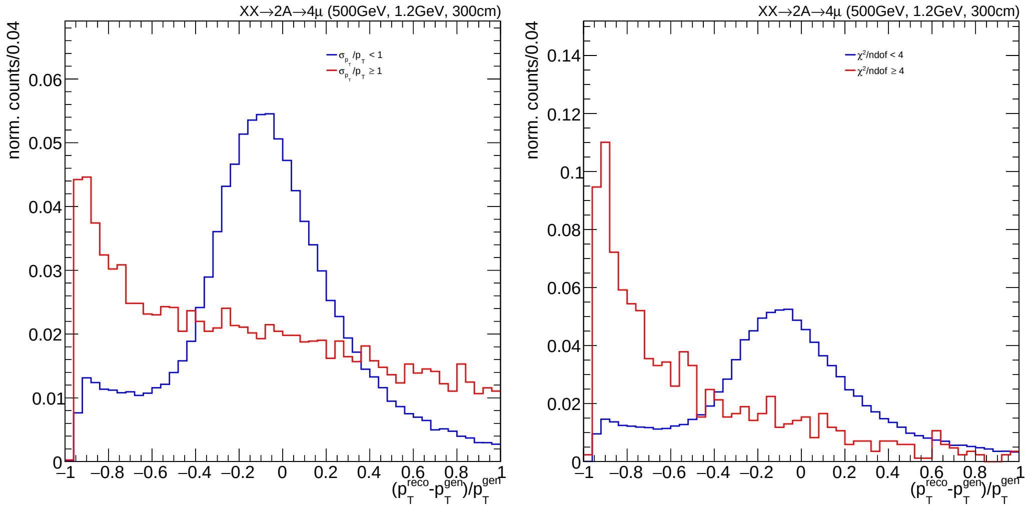

Figure 3.8: DSA muon p_{T} resolution, normalized to unit area, for the 4μ signal sample with $m_{\chi\bar{\chi}} = 500\,\mathrm{GeV}$, $m_{Z_d} = 1.2\,\mathrm{GeV}$, and lxy $= 300\,\mathrm{cm}$ for events with $\sigma_{p_{\mathrm{T}}}/p_{\mathrm{T}} < 1$ and $\geqslant 1$ separately (*left*), and events with $\chi^2/\mathrm{ndof} < 4$ and $\geqslant 4$ separately (*right*).

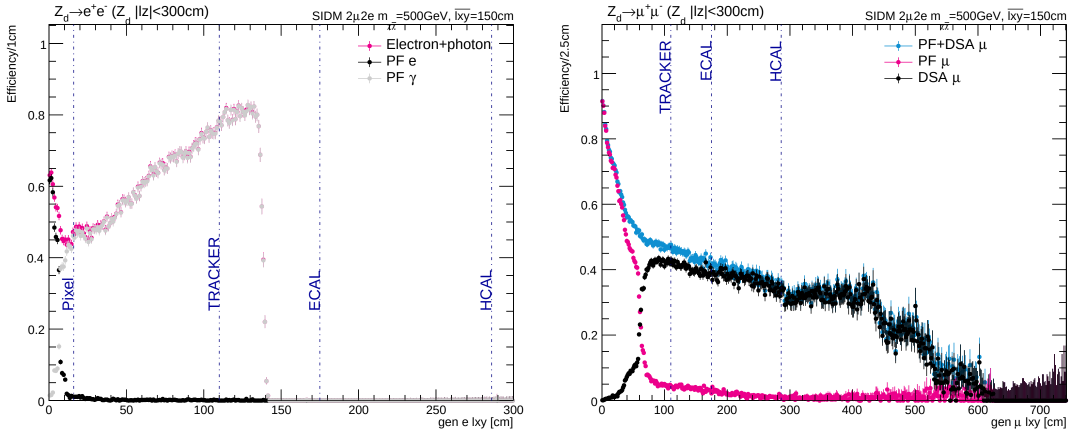

Figure 3.9: ID efficiency for lepton-jet input candidates as a function of gen-level lepton's lxy from signal $2\mu 2$e MC samples. *Left*: $e\gamma$ candidates. PFElectron efficiency quickly falls down to zero due to tight GSF tracking requirements; PFPhoton efficiency starts to pick up and keep increasing up to $\approx 140\,\mathrm{cm}$, corresponding to the ECAL crystal boundary, before it falls down to zero as well. *Right*: muon candidates. PFMuon efficiency drops down to about zero at lxy$\approx 70\,\mathrm{cm}$ due to the limit of iterative tracking; DSAMuon efficiency picks up from there and dominates the rest of the lxy band.

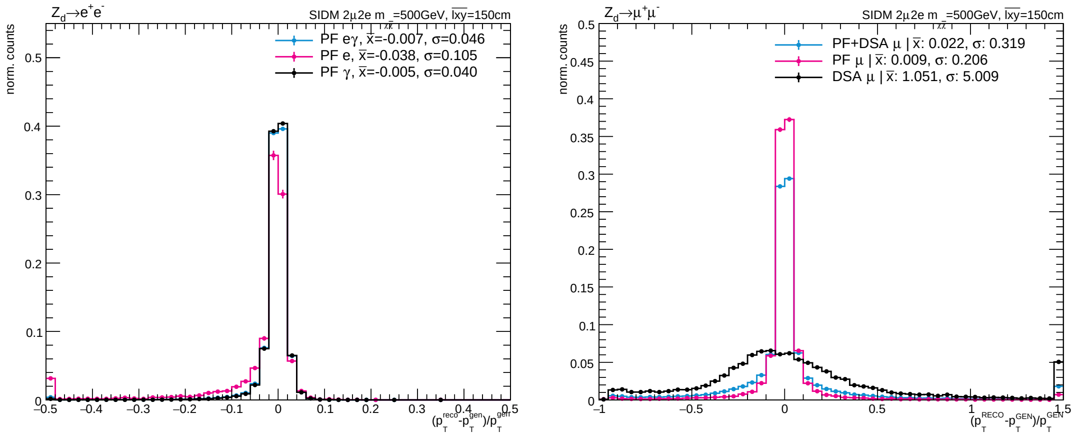

Figure 3.10: p_T resolution for lepton-jet input candidates from signal $2\mu2e$ MC samples. *Left*: $e\gamma$ candidates (PFElectrons in pink, PFPhotons in black, combined in blue). *Right*: muon candidates (PFMuons in pink, DSA muons in black, combined in blue).

Performance

The efficiency of the identification criteria for the lepton-jet input candidates is shown in figure 3.9 for $e\gamma$ candidates (left) and muon candidates (right) as a function of gen-level lepton's lxy. The p_T resolution of input candidates is shown in figure 3.10.

3.2.4 Lepton-jet clustering and categorization

After the source candidate particles have been identified, they are clustered together as lepton-jets using the anti-k_T algorithm [131,132] with a cone size $\Delta R = 0.4$. Those with $p_\mathrm{T} > 30\,\mathrm{GeV}$ and $|\eta| < 2.4$ are kept for further analysis. Lepton-jets are categorized into *EGM-type* and *muon-type* based on the constituents of the lepton-jets. Lepton-jets which contains only electron and photon candidates (0 muon candidates) are labeled as *EGM-type*. Lepton-jets which contains an even number of muon candidates are labeled as *muon-type*. Depending on whether they have DSA muon candidates, muon-type lepton-jets are further categorized into *PFMu-type* (0 DSA muon candidates), and *DSAMu-type* (⩾1 DSA muon candidate). Muon-type lepton-jets with an odd number of muon candidates are not taken into consideration because they do not give the right p_{T} resolution with respect to the dark photon. This usually happens when one of the two muons failed to be reconstructed. To suppress events from B hadron cascade decays (same sign di-muon), the charge sum of all candidates in a muon-type lepton-jet is required to be zero.

The base selections of lepton-jets are summarized in table 3.14. The categorization of lepton-jets that pass our base selection is summarized in table 3.15.

Variable	Value
p_{T}	$> 30\,\mathrm{GeV}$
$\lvert\eta\rvert$	< 2.4
N(DSA+PF muons)%2	$= 0$
$\sum$Q(DSA+PF muons)	$= 0$

Table 3.14: Summary of lepton-jet base selections

Category	Criteria
EGM-type	N(DSA+PF muons) $= 0$
PFMu-type	N(DSA+PF muons)$\geqslant 2$ and N(DSA muons) $= 0$
DSA-type	N(DSA+PF muons)$\geqslant 2$ and N(DSA muons) > 0

Table 3.15: Lepton-jet categories

3.2.5 Lepton-jet reconstruction performance

Figure 3.11 shows the reconstruction efficiency of EGM-type and muon-type lepton-jets as a function of the dark photon's flight distance in the transverse plane. Figure 3.12 shows the p_{T} resolution of EGM-type and muon-type lepton-jets from the simulated signal events. Figure 3.13 shows the reconstructed invariant mass of the lepton-jet pair from samples with $m_{\chi\bar{\chi}} = 100, 500$ and $1000\,\mathrm{GeV}$.

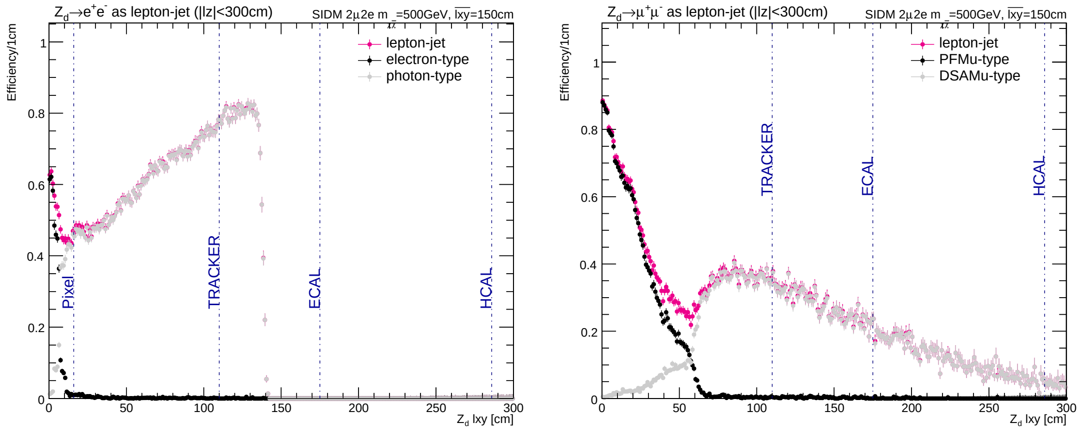

Figure 3.11: Lepton-jet reconstruction efficiency (pink) as a function of the dark photon's flight distance in the transverse plane (lxy) from signal $2\mu 2$e samples. *Left*: EGM-type lepton-jets. The efficiency to reconstruct lepton-jets with at least one PFElectron candidate (black) quickly falls to zero due to the GSF tracking requirement of the PFElectrons reconstruction. The efficiency for photon-type lepton-jets (grey) keeps increasing up to $\sim 140\,\mathrm{cm}$, corresponding to ECAL crystal boundary, before dropping to zero as well. *Right*: muon-type lepton-jets. The PFMu-type efficiency (black) drops down to about zero at lxy $\sim 70\,\mathrm{cm}$ due to the limits of iterative tracking for PFMuons. The DSA muon efficiency (green) picks up from there and dominates the rest of the lxy distribution.

3.3 Simulation corrections

Monte Carlo simulation do not generally perfectly reproduce the data due to the facts of varying running conditions, detector component failure and inefficiencies etc. To better compare the results obtained from simulation and data, and to more accurately predict the expected yield for different signal hypotheses, a set of corrections and scale factors are applied to the simulated samples, they are described in the below.

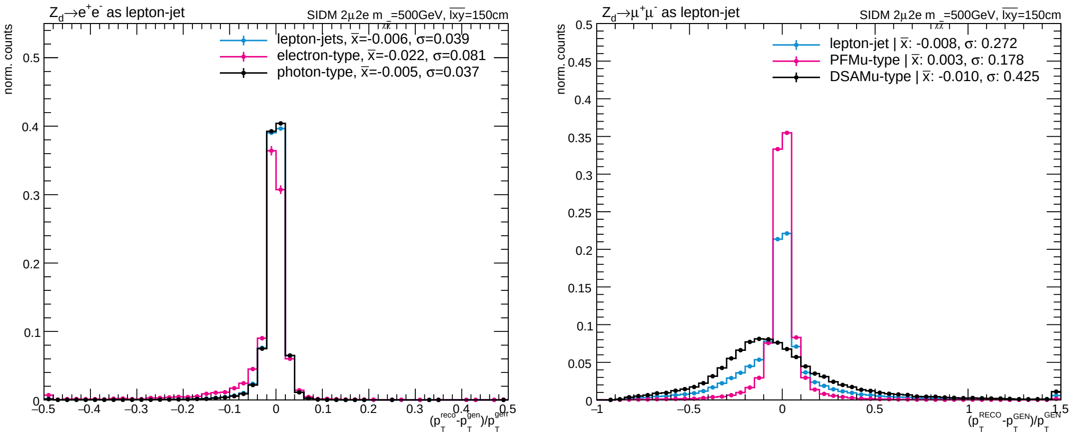

Figure 3.12: Lepton-jet p_{T} resolution from signal 2μ2e samples. *Left*: All EGM-type lepton-jets (blue), electron-type lepton-jets (pink) and photon-type lepton-jets (black). *Right*: muon-type lepton-jets (blue), PFMu-type lepton-jets (pink) and DSA-type lepton-jets (black).

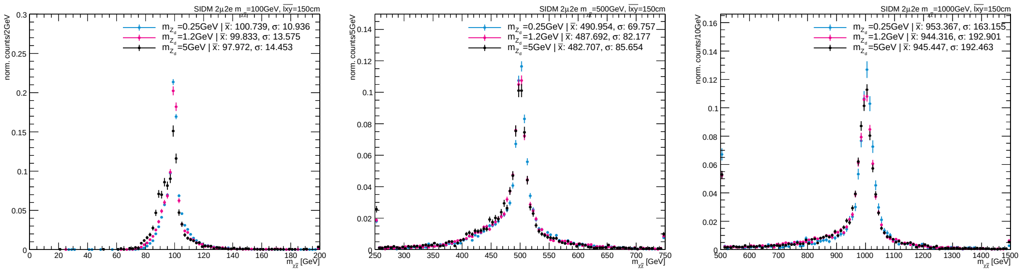

Figure 3.13: Dark matter bound state invariant mass (from *left* to *right*, $m_{\chi\bar{\chi}} = 100, 500, 1000\,\mathrm{GeV}$), reconstructed using lepton-jet pairs in simulated MC signal events.

3.3.1 Pileup corrections

Pileup occurs in CMS due to the high instantaneous luminosity of proton beams in the LHC. In each bunch crossing, several proton-proton interactions in addition to the main hard scatter of interest will add extra tracks and energy deposits to the event. The number of additional vertices varies per event. Although such effects are accounted for in the simulation, the discrepancy persists in the distribution of the number of vertices per event between the data and the simulation. This motivates a reweight applied to the simulated events. Here we follow the standard prescription recommended for pileup corrections.

Figure 3.14 show the observed number of vertices in data compared to the equivalent distribution in simulation (using QCD samples as reference) for 2018.

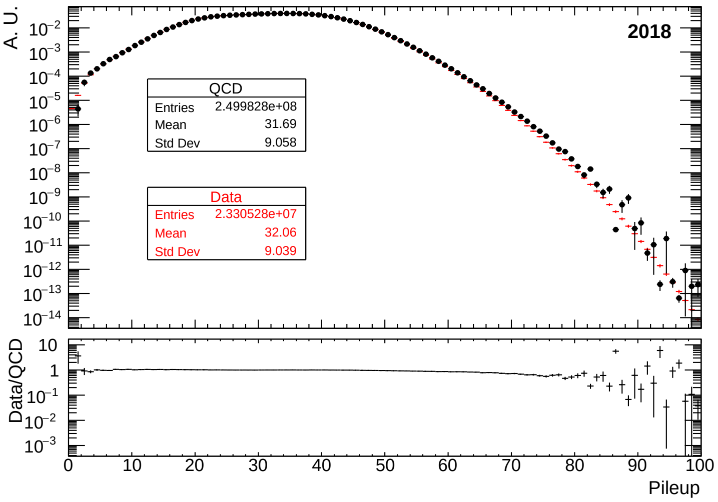

Figure 3.14: True pileup distribution in QCD MC simulation (black) and data (red) for 2018 condition.

3.3.2 Lepton ID scale factors

As discussed in section 3.2.3, we used *loose* POG ID for PF electrons, photons and muons. The difference in identification efficiency between data and simulation is centrally measured by the POG. These scale factors are parameterized by the object (e, γ, μ)'s p_{T} and η.

Figure 3.15 shows the scale factors for cut-based loose electron (left) and photon (right) ID in a 2D map as a function of its p_{T} and ECAL supercluster η.

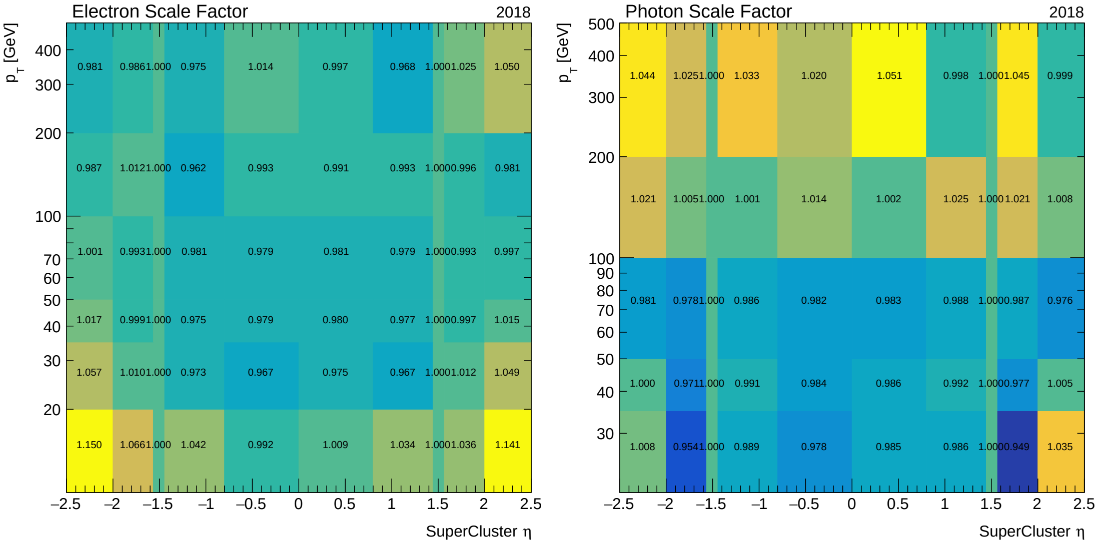

Figure 3.15: Electron (*left*) and photon (*right*) ID scale factors at the "loose" working point as measured by the EGM POG for 2018.

Figure 3.16 shows the scale factor for cut-based loose muon ID as a function of muon p_{T} and η. The left one is the result from POG. However, it only provides scale factors for muons whose p_{T} is as low as 15 GeV. Since our minimum muon p_{T} cut is 5 GeV, the scale factors and associated systematic uncertainties need to be measured additionally. Here we adopt the POG-approved result from $H \to ZZ \to 4l$ analysis group [23] for muons with p_{T} between (5, 20) GeV, shown in the right. For muons with $p_{\mathrm{T}} > 20$ GeV, we use the official result from the POG.

The uncertainties on the scale factors are varied independently, and the resulting differences in the weight are included as systematic uncertainties in the analysis. This will be further discussed later.

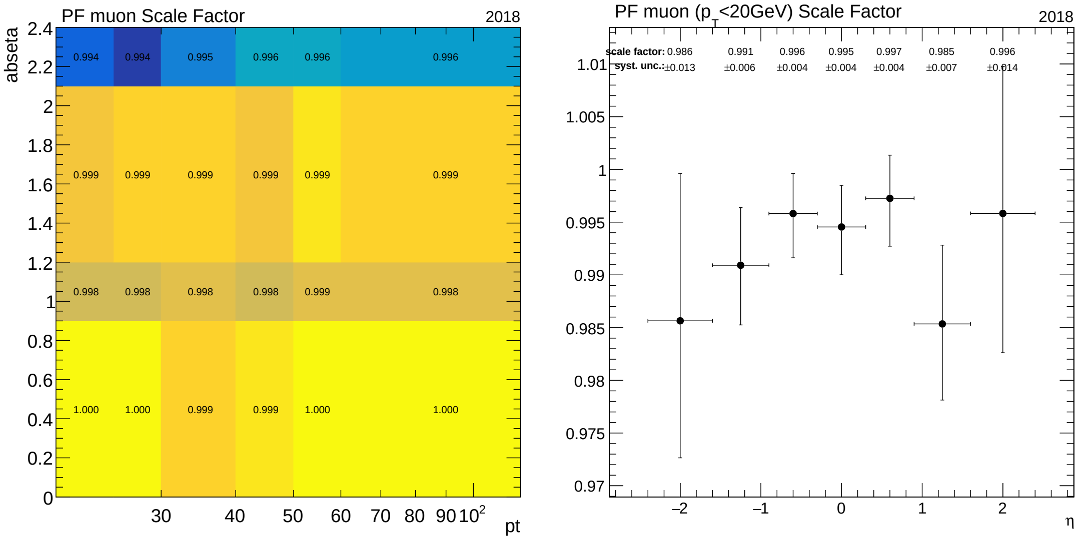

Figure 3.16: Muon ID scale factor at the "loose" working point as measured by the MUON POG for 2018 (*left*, $p_{\mathrm{T}} > 15\,\mathrm{GeV}$), and the ID scale factor for "loose" muons with $p_{\mathrm{T}} < 20\,\mathrm{GeV}$. (*right*)

3.4 Cosmic ray muon veto

Cosmic muons from the atmosphere often cross the CMS detector, and sometimes events collected during pp collisions can randomly pick up such tracks. Typically they would traverse the detector from top to bottom at an arbitrary angle, and thus can be easily removed by requiring the distance of closest approach with respect to the primary vertex to be small. When muons are reconstructed by particle flow, such care is taken and therefore PFMuons are mostly free of cosmic muons. However, DSA muons are more subjective to be from cosmic muons due to the seeding configuration and the absence of the beamspot constraint. Because the signal can be largely displaced from the primary vertex, other handles are used to suppress the contamination from cosmic muons.

3.4.1 Event-level cosmic veto

Sometimes, cosmic muon showers will contain a large number of parallel pairs of cosmic muons. To avoid contamination from those showers, we count all possible pairs of cosmic muons ($p_{\mathrm{T}} > 5\,\mathrm{GeV}, |\eta| < 1.2$), and the number N(parallel pairs) of such pairs with $|\cos\alpha| > 0.99$ is required to be $\leqslant 6$. This selection yields negligible efficiency loss in signal events, as shown in figure 3.17.

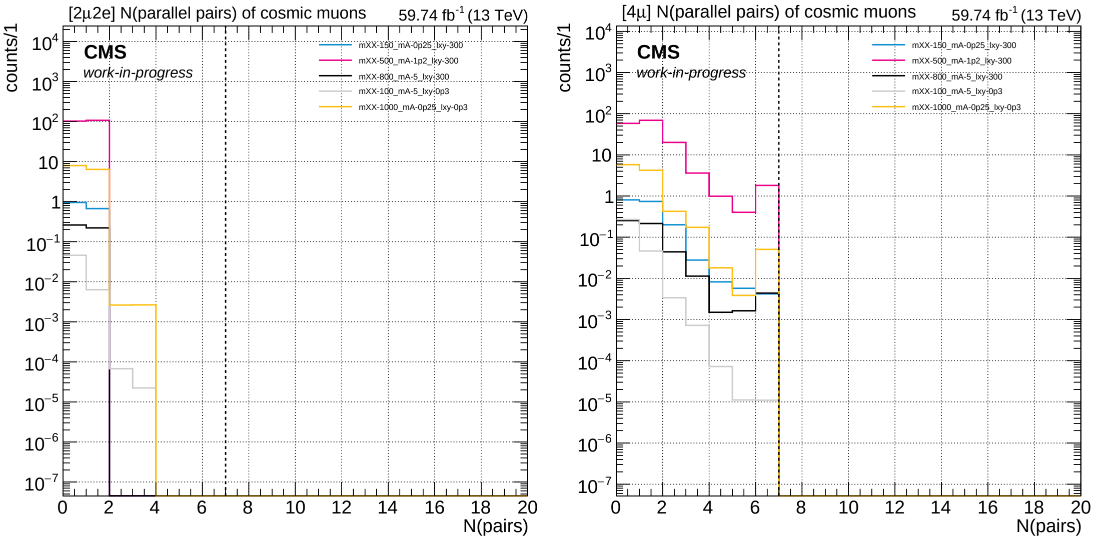

Figure 3.17: Distributions of number of parallel ($|\cos\alpha| > 0.99$) cosmic muons using signal MC for both channels. Events with $N > 6$ parallel muon pairs are rejected and used as a cosmic muon enriched sample.

To study the effect of object-level cuts to reject lepton-jets from cosmic muons, we use the region with $N > 6$ parallel pairs as a cosmic muon enriched region.

3.4.2 Object-level cosmic veto

Parallel cosmic muons can have similar η and ϕ values even when they are actually far apart. To prevent these parallel muons from being clustered into a lepton-jet, we compare the distance of closest approach (DCA) for all track pairs within a lepton-jet. The minimum track-track DCA is required to be less than 20 cm when there are at least 2 tracks. Figure 3.19 shows the distributions of this quantity in data and signal MC on the left. The data sample includes all events with at least two lepton-jets in the cosmics enriched region ($N(\text{parallel}) > 6$). The DCA cut at 20 cm leads to a $\sim 1.6\%$ signal efficiency loss on average while suppressing $\sim 88\%$ cosmic shower events.

Figure 3.18 shows an event display in data where two cosmic tracks get clustered into a lepton-jet but the minimum track-track DCA > 20 cm.

Another handle we use to reject muons from cosmic ray showers is the maximum track |dz| for tracks in a lepton-jet. As shown in figure 3.19 on the right, cosmic ray muons can have large |dz|. We require that lepton-jets satisfy max track $|\text{dz}| \leqslant 40$ cm. This cut results in $\sim 1.2\%$ signal loss on average while suppressing $\sim 99\%$ cosmic shower events.

Cosmic muons crossing the CMS detector will have a trajectory that looks like a straight line (figure 3.20). To take advantage of this feature, we define ΔR_{cosmic} as the following:

$$\Delta R_{\text{cosmic}} = \sqrt{(\eta_1 + \eta_2)^2 + (\pi - \Delta\phi)^2} \tag{3.4}$$

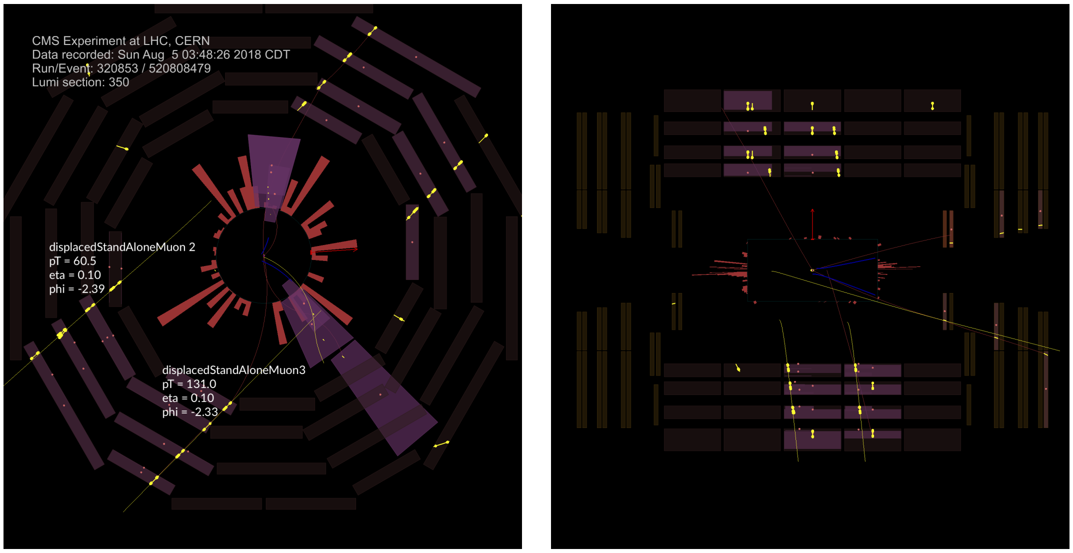

Figure 3.18: Event display of event 520808479 in 2018 data, in run 320853, lumi section 350. *Left*: ρ-ϕ view; *Right*: ρ-z view. A pair of cosmic muons traversed the CMS detector from top to bottom, and they are both reconstructed as DSA muons. The ΔR between the top one (marked as `displacedStandAloneMuon 2`) and the bottom one (marked as `displacedStandAloneMuon 3`) on the left is $\sqrt{(0.1-0.1)^2+(-2.39-(-2.33))^2} \approx 0.06$, less than 0.4. While the distance of closest approach is $> 20\,\text{cm}$ (the cylinder at the center of the figure marks the boundary of Tracker, recall the outer radius of the Tracker is ~ 1.2 m).

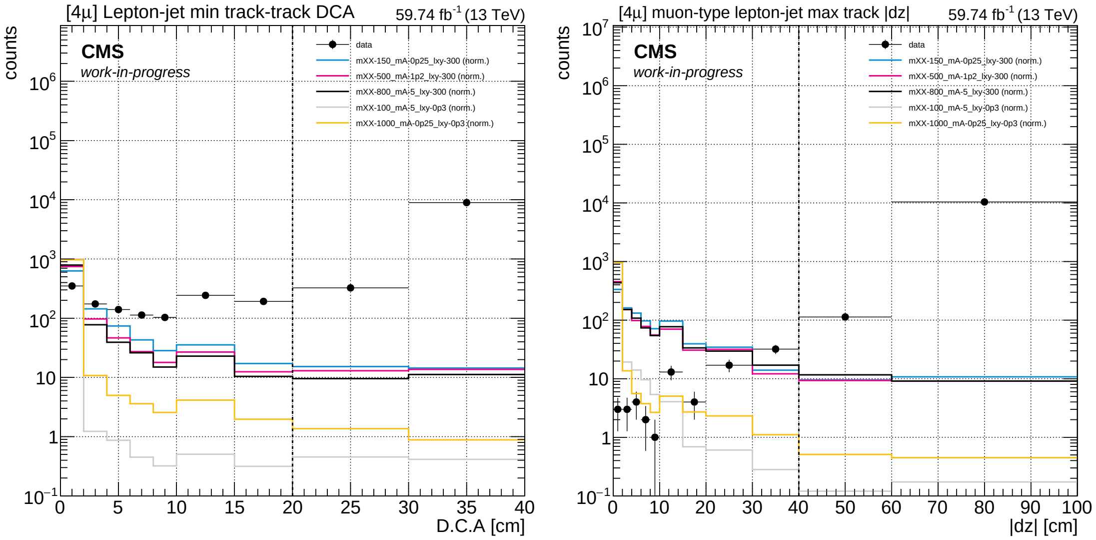

Figure 3.19: Minimum distance of closest approach (DCA) between any two tracks within a lepton-jet (*left*). Max track |dz| of a lepton-jet (*right*). Data points are from cosmic muon enriched (N(parallel) > 6) sample, and signal samples are selected with N(parallel) $\leqslant 6$ and are normalized arbitrarily. Lepton-jets with min $\mathrm{DCA}_{\mathrm{tktk}} > 20\,\mathrm{cm}$ or max track $|\mathrm{dz}| > 40\,\mathrm{cm}$ are treated as being contaminated by cosmics and will be rejected for further consideration.

We calculate $\Delta R_{\mathrm{cosmic}}$ between DSA pairs reconstructed in opposite hemispheres, and between DSA and muon (DT, CSC) segments in opposite hemispheres. Figure 3.21 shows the $\Delta R_{\mathrm{cosmic}}$ distributions from data and arbitrarily normalized signal MC samples. We require $\min(\Delta R_{\mathrm{cosmic}}(\mathrm{DSA}_i, \mathrm{DSA}_j)) > 0.05$, and $\min(\Delta R_{\mathrm{cosmic}}(\mathrm{DSA}_i, \mathrm{DT/CSC\ segement})) > 0.05$ for any DSA muon inside the lepton-jet.

3.4.3 Summary of cosmic veto

The cuts used to suppress cosmic ray showers are shown in table 3.16. After applying these three object-level cuts (min track-track DCA, max track |dz|, and $\Delta R_{\mathrm{cosmic}}$),

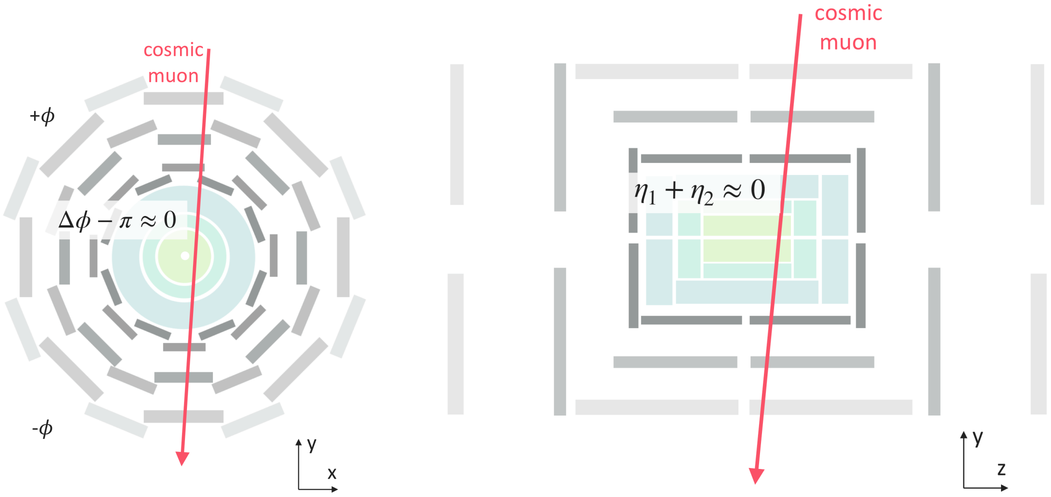

Figure 3.20: Cartoon of a cosmic muon transversing the detector in the x-y (*left*) and y-z (*right*) views.

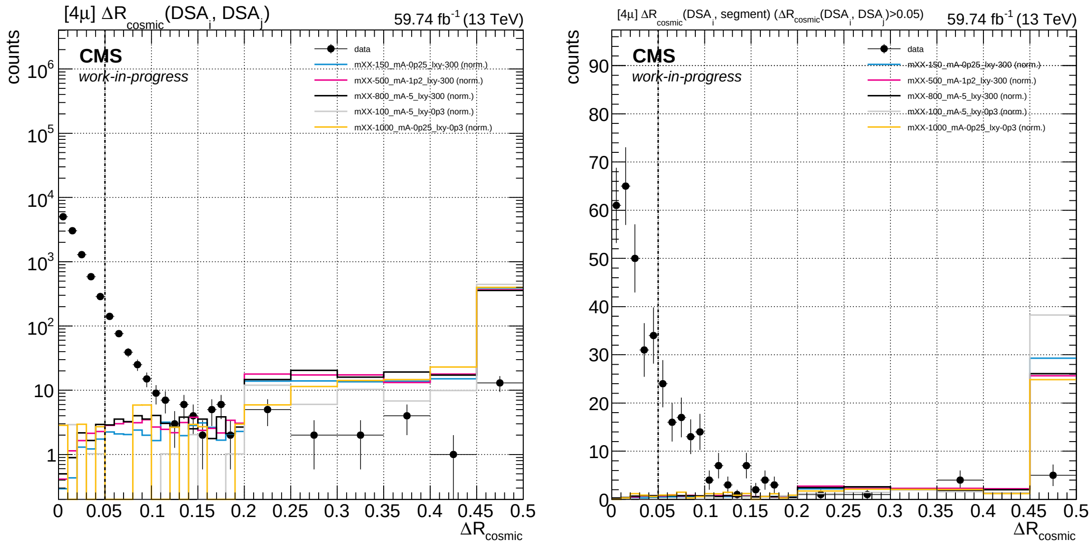

Figure 3.21: Minimum ΔR_{cosmic} between a DSA muon in a lepton-jet and a DSA muon in the opposite hemisphere (*left*). Minimum ΔR_{cosmic} between a DSA muon in a lepton-jet and DT or CSC segments in the opposite hemisphere when $\Delta R_{\text{cosmic}}(\text{DSA}_i, \text{DSA}_j) > 0.05$ (*right*). Data points are from a cosmic muon enriched ($N(\text{parallel}) > 6$) sample, and signal samples are selected with $N(\text{parallel}) \leqslant 6$ and are normalized arbitrarily. DSA-type lepton-jets with $\Delta R_{\text{cosmic}} < 0.05$ are treated as being contaminated by cosmics and will be rejected for further consideration.

there is 0 event that survives out of the 5298 events from the cosmic muon enriched sample. We therefore consider the contamination from cosmic muons to be negligible.

Variable	Value
N(parallel muon pairs)	$\leqslant 6$
Min track-track DCA	$< 20\,\mathrm{cm}$, when N(track)$\geqslant 2$
Max track |dz|	$> 40\,\mathrm{cm}$
$\Delta R_{\mathrm{cosmic}}$	< 0.05

Table 3.16: Summary of cosmic muon veto

3.5 Event and object selections

3.5.1 Search channels

In this analysis, we consider events that have at least 2 lepton-jets passing the base selections and cosmic muon vetoes outlined in the previous sections. We define two search channels based on the decay products of the dark photons. We require one dark photon to decay to a muon pair (for triggering purpose), and the other one can decay to either an electron pair ($2\mu 2e$ channel) or a muon pair (4μ channel). For the $2\mu 2e$ channel, one of the leading two lepton-jets (sorted by p_{T} in descending order) is required to be an EGM-type lepton-jet, and the other one is required to be a muon-type lepton-jet. For the 4μ channel, both of the two leading lepton-jets need to be muon-type. Table 3.17 summarizes the definition of the two search channels.

Channel	Definition
$2\mu 2e$	$\geqslant 2$ lepton-jets, leading two are muon-type + EGM-type.
4μ	$\geqslant 2$ lepton-jets, leading two are muon-type.

Table 3.17: Search channel definitions

3.5.2 Primary vertex filter

Some events recorded have no pp collision vertices and contain only cosmic muons. Events are therefore required to contain at least one well-identified vertex with position (x, y, z) satisfying the following requirements:

- Vertex's number of degrees of freedom > 4.
- $|z| < 24$ mm.
- $\sqrt{x^2 + y^2} < 2$ mm.

This set of requirements is referred to in CMS as the `PrimaryVertexFilter`. Events which do not pass the `PrimaryVertexFilter` will be rejected for further selection.

3.5.3 Displacement cut

The lepton-jets produced in the decay of long-lived dark photons are mostly displaced from the primary vertex, whereas most SM processes only produce prompt muons, whose tracks are associated with the primary vertex. Therefore, by requiring the muon tracks inside the muon-type lepton-jets to be *displaced*, we can suppress most Drell-Yan+jets and di-boson background contributions and enhance the signal significance at the same time.

There are several variables associated with the lepton-jet that can be used to characterize the displacement. The distance between the lepton-jet vertex and the primary vertex in the transverse plane is referred to as $\mathrm{v_{xy}}$, and the $\mathrm{v_{xy}}$ significance is defined as $\mathrm{v_{xy}}/\sigma_{\mathrm{v_{xy}}}$. Cutting on either of these variables, however, will result in additional signal efficiency loss because of the inefficiency of forming a common vertex from the collimated lepton-jet constituents. Instead, it's preferred to considering the $|d0|$ values of tracks within the lepton-jet, where $d0$ is defined as the distance of closest approach with respect to the primary vertex in the transverse plane. The $|d0|$ significance, which is defined as $|d0|/\sigma_{d0}$, takes into account the uncertainty of the measurement and is another displacement variable worth evaluation. After comparing the forward significance $s/\sqrt{b}$ by cutting both variables, $|d0|$ is preferred because it gives higher significance based on evaluation of signal and background MC (section 3.6.5). Because a lepton-jet can contain multiple tracks, we choose to require that the **minimum** $|d0|$ of tracks in the lepton-jet be greater than a threshold. This reduces the chance that a single track happens to have a large $|d0|$ due to mismeasurement or misreconstruction.

On the event level, for the $2\mu 2e$ channel, the displacement cut is applied to the muon-type lepton-jet; for the 4μ channel, the displacement cut is applied to the maximum value of the leading two muon-type lepton-jets, in other words, only one of the two lepton-jets is required to be displaced. Figure 3.22 shows the `mind0` distribution of the muon-type lepton-jets in the $2\mu 2e$ channel and the `mind0` distribution of the most displaced lepton-jet in the 4μ channel in simulated signal and background events. For the signal event selection, we require the lepton-jet's `mind0` to be greater than 0.5 mm for both channels as the initial cuts. The optimization of this cut will be described later.

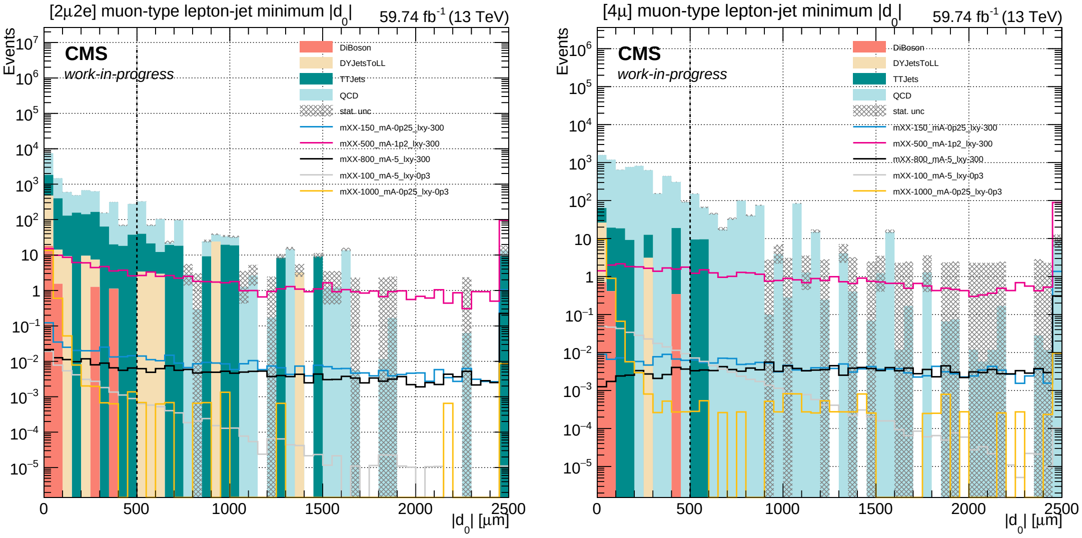

Figure 3.22: *Left*: `mind0` of muon-type lepton-jet for channel $2\mu 2e$; *Right*: maximum `mind0` value of the leading two muon-type lepton-jets for channel 4μ. The initial cut at 0.5 mm is shown as vertical black dashed lines.

3.5.4 Lepton-jet isolation

In signal processes, lepton-jets are produced with little activity nearby. Therefore, a requirement on the lepton-jet isolation can distinguish lepton-jets in signal events from lepton-jets produced by hadronic jets in background events. The lepton-jet isolation is defined as a ratio of two energy sums. The numerator includes PFCandidates (associated with the primary vertex and excluding muon-type candidates) within a cone $\Delta R = 0.5$ with respect to the lepton-jet axis, but not including the constituents of the lepton-jet. The denominator is the numerator value plus the lepton-jet's energy. Thus, the smaller the isolation value, the more isolated the lepton-jet is.

$$\mathrm{Iso}_{\text{lepton-jet}} = \frac{\sum_i E_i(\Delta R(\mathrm{cand}_i, \text{lepton-jet}) < 0.5, \mathrm{cand}_i \notin \text{lepton-jet}, \mathrm{cand}_i \neq \mu\text{-type})}{\text{numerator} + E_{\text{lepton-jet}}} \tag{3.5}$$

On the event level, for the $2\mu2e$ channel, the isolation cut is applied to the EGM-type lepton-jet; for the 4μ channel, the isolation cut is applied to the maximum value of the leading two muon-type lepton-jets, in other words, both lepton-jets are required to be isolated. Figure 3.23 shows the distribution of the EGM-type lepton-jet isolation value for channel $2\mu2e$ and the maximum value of the leading two muon-type lepton-jet isolation for channel 4μ after the displacement cut is applied. For channel $2\mu2e$, we require the EGM-type lepton-jet's isolation to be less than 0.1 as the initial cut; and for channel 4μ, we require the maximum lepton-jet's isolation to be less than 0.2 as the initial cut. The optimization of this cut will be described later.

3.5.5 $|\Delta\phi|$ between the lepton-jet pair

The signal process is a two-body decay of a heavy DM bound state into two light dark photons. Therefore, a back-to-back topology on the beam transverse plane is expected between the two lepton-jets in signal events. This means that we expect a large $|\Delta\phi|$ (absolute ϕ angle difference in the transverse plane) between the lepton-jet pair. Figure 3.24 shows this distribution for each search channel. We require $|\Delta\phi| > 2.2$ as the initial cut. The optimization of this cut will be described later.

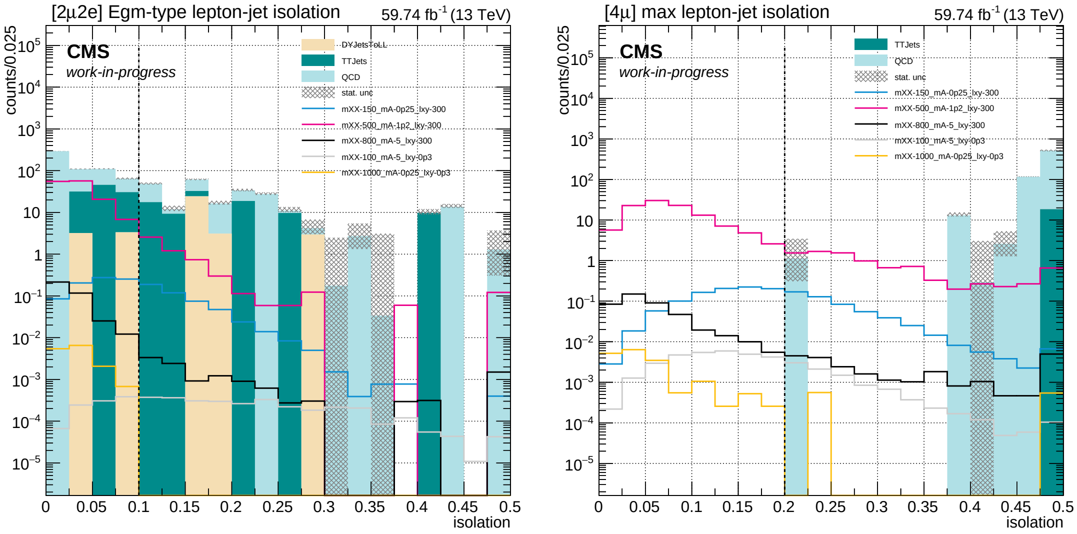

Figure 3.23: *Left*: EGM-type lepton-jet isolation distribution from channel $2\mu 2e$; *Right*: maximum isolation of the leading two muon-type lepton-jets from channel 4μ. The displacement cuts described in section 3.5.3 have been applied. The initial cut at 0.1(0.2) for channel $2\mu 2e(4\mu)$ is shown as vertical black dashed lines.

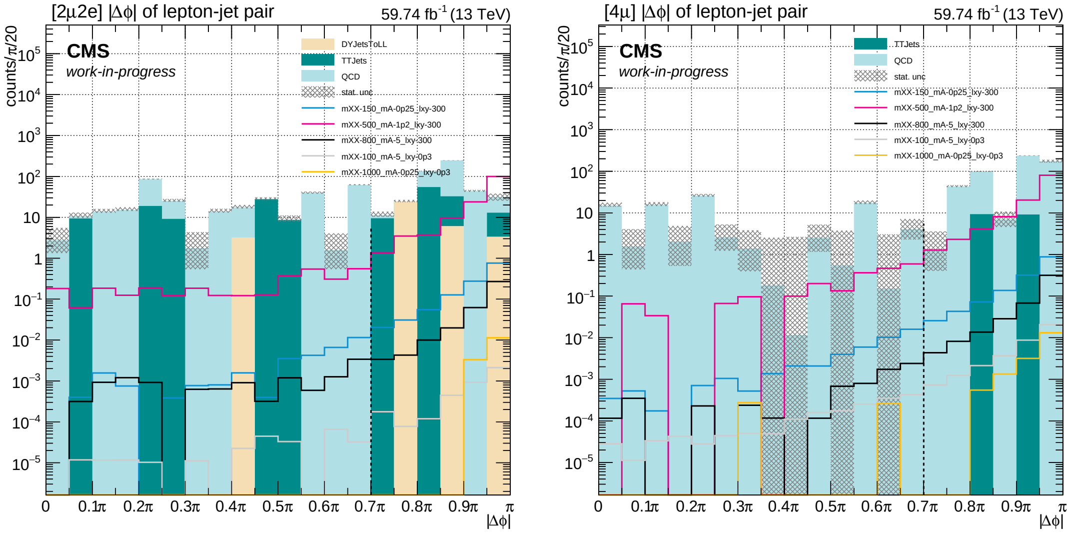

Figure 3.24: $|\Delta\phi|$ between the leading two lepton-jets for channel $2\mu 2e$ (*left*) and channel 4μ (*right*). The displacement cuts described in section 3.5.3 have been applied. The initial cut at 2.2 is shown as vertical black dashed lines.

3.5.6 Summary

We summarize the signal event selections for both search channels in table 3.18.

Variable	Value	
	$2\mu 2e$	4μ
Primary vertex filter	Pass	
Cosmic muon veto	Pass	
Lepton-jet `mind0` *	> 0.5 mm	
Lepton-jet isolation *	< 0.1	< 0.2
Lepton-jet pair $\|\Delta\phi\|$ *	> 2.2	

Table 3.18: Summary of initial signal event selections. The cut value for variable names with a * are going to be optimized later.

3.6 Background estimation

Due to MC simulation limitations, the background estimation is performed with events in data. To avoid potential bias, events passing the full signal region selections are blinded until the very last step of the analysis. The background yield is estimated using control regions which are rich in background events while expected to be free of signal events. We first describe the ABCD method which is used to estimate the background contribution in the signal region, then describe the validation, closure tests and optimization for each channel.

3.6.1 Simple ABCD method

Following the principle of the ABCD method, we use two event-level variables – the first one is the isolation variable associated with the lepton-jet (section 3.5.4) and the

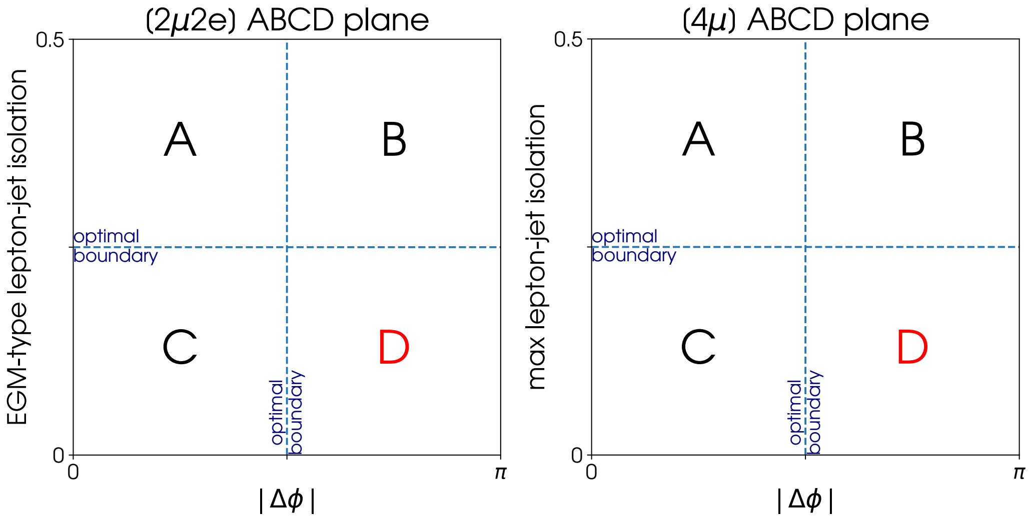

Figure 3.25: ABCD plane definitions for background estimation. Region D, where events have large $|\Delta\phi|$ and small isolation value, is the signal region. Regions A, B, and C are used to estimate the expected background yield in Region D. *Left*: channel $2\mu 2e$, the variable on the vertical axis is the EGM-type lepton-jet's isolation; *Right*: channel 4μ, the variable on the vertical axis is the maximum isolation of the two leading lepton-jets.

second one is the $|\Delta\phi|$ between the pair of lepton-jets (section 3.5.5) – to define a 2D plane, as sketched in figure 3.25. The number of events in signal region D, where events have large $|\Delta\phi|$ and small isolation value, is estimated from the other 3 regions – A, B and C using the following equation:

$$N_D^{\text{est}} = \frac{N_B \times N_C}{N_A} \tag{3.6}$$

The statistical uncertainties on the yields in regions A, B, and C propagate to region D through the following equation:

$$\begin{aligned}\delta N_D^{\text{est}} &= N_D^{\text{est}}\sqrt{(\frac{\delta N_A}{N_A})^2 + (\frac{\delta N_B}{N_B})^2 + (\frac{\delta N_C}{N_C})^2} \\ &\approx N_D^{\text{est}}\sqrt{(\frac{\sqrt{N_A}}{N_A})^2 + (\frac{\sqrt{N_B}}{N_B})^2 + (\frac{\sqrt{N_C}}{N_C})^2} \\ &= N_D^{\text{est}}\sqrt{\frac{1}{N_A} + \frac{1}{N_B} + \frac{1}{N_C}}\end{aligned} \tag{3.7}$$

3.6.2 ABCD validation regions

To validate that this method works, we will need a control region that is similar to our signal region but free of signal events. So we want a region that has a similar background composition as that of the signal region (figure 3.23, figure 3.24), i.e. minimal DY+jets and dominated by QCD/$t\bar{t}$+jets events.

For both channels, we define a validation region (VR) by using a single muon as a proxy for a muon-type lepton-jet. This allows us to construct validation regions with sufficient statistics to study the closure of the background estimation method. The proxy muons must pass the same selections as muons used in the lepton-jet clustering. For the channel $2\mu 2e$ validation region, we select events that have one EGM-type lepton-jet, 0 muon-type lepton-jets, and a single muon. For the channel 4μ validation region, we require that there is only one muon-type lepton-jet, 0 EGM-type lepton-jets, and a single muon. As such, the proxy events are orthogonal to the signal region. Events in the validation region must pass the same displacement requirements as our signal region (`mind0` > 0.5 mm for both channels).

To minimize signal contamination in the validation region and to suppress DY+jets events, we require there to be at least one tight b-jet in the event, where b-jets are required to satisfy $p_\mathrm{T} > 30\,\mathrm{GeV}$, $|\eta| < 2.5$, and pass the tight working point of the DeepCSV algorithm [133, 134]. The tight working point gives the lowest mistag rate. Figure 3.26 shows the b-jet multiplicity of proxy events for both channels.

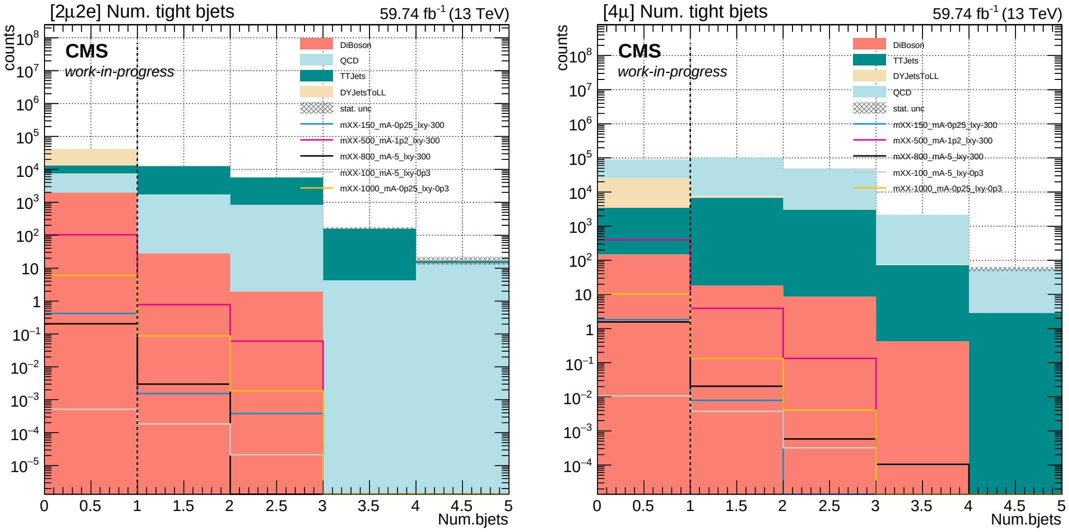

Figure 3.26: Distributions of the number of b-jets tagged by the DeepCSV algorithm's tight working point in proxy events for both channels (no displacement cut is applied). Events with $N_{b\text{-jet}} > 0$ are used for the validation regions.

Signal Sample $[(m_{\chi\bar{\chi}}, m_{Z_d}), \mathrm{lxy}]$	N_A	N_B	N_C	N_D
(150, 0.25) GeV, 300 cm	0	0	0	0
(500, 1.2) GeV, 300 cm	0	0	0.06	0.72
(800, 5) GeV, 300 cm	0	0	0	0
(100, 5) GeV, 0.3 cm	0	0	0	0
(1000, 0.25) GeV, 0.3 cm	0	0	0	0
Data in validation region (VR)	253	221	235	236

Table 3.19: Event counts of representative signal MC and data for $2\mu 2e$ channel in the validation ABCD plane. Region A,B,C,D are separated by the initial boundary Iso=0.1 and $|\Delta\phi| = 2.2$ as in table 3.18.

Sample Name $[(m_{\chi\bar{\chi}}, m_{Z_d}), \text{lxy}]$	N_A	N_B	N_C	N_D
(150, 0.25) GeV, 300 cm	0	0	0	0
(500, 1.2) GeV, 300 cm	0	0.3	0.07	1.99
(800, 5) GeV, 300 cm	0	0	0	0.01
(100, 5) GeV, 0.3 cm	0	0	0	0
(1000, 0.25) GeV, 0.3 cm	0	0	0	0
Data in validation region (VR)	762	2808	80	286

Table 3.20: Event counts of representative signal MC and data for 4μ channel in the validation ABCD plane. Region A,B,C,D are separated by the initial boundary Iso=0.2 and $|\Delta\phi| = 2.2$ as in table 3.18.

For reference, the event counts of several signal MC samples after applying the validation region definitions are listed in table 3.19 for channel $2\mu 2e$ and in table 3.20 for channel 4μ. From those, we can see that the contamination from signal events in the validation regions is negligible.

Correlation check in the validation region

One of the primary assumptions of the ABCD method is that the two variables are uncorrelated. To check the correlation in the validation regions, we plot the ratio of events with large isolation values to events with small isolation values as a function of $|\Delta\phi|$ and vice versa. This is shown in figure 3.27 for the $2\mu 2e$ channel and figure 3.28 for the 4μ channel. In all four ratio plots, the ratio is consistent with a constant and does not indicate any obvious correlation between the variables.

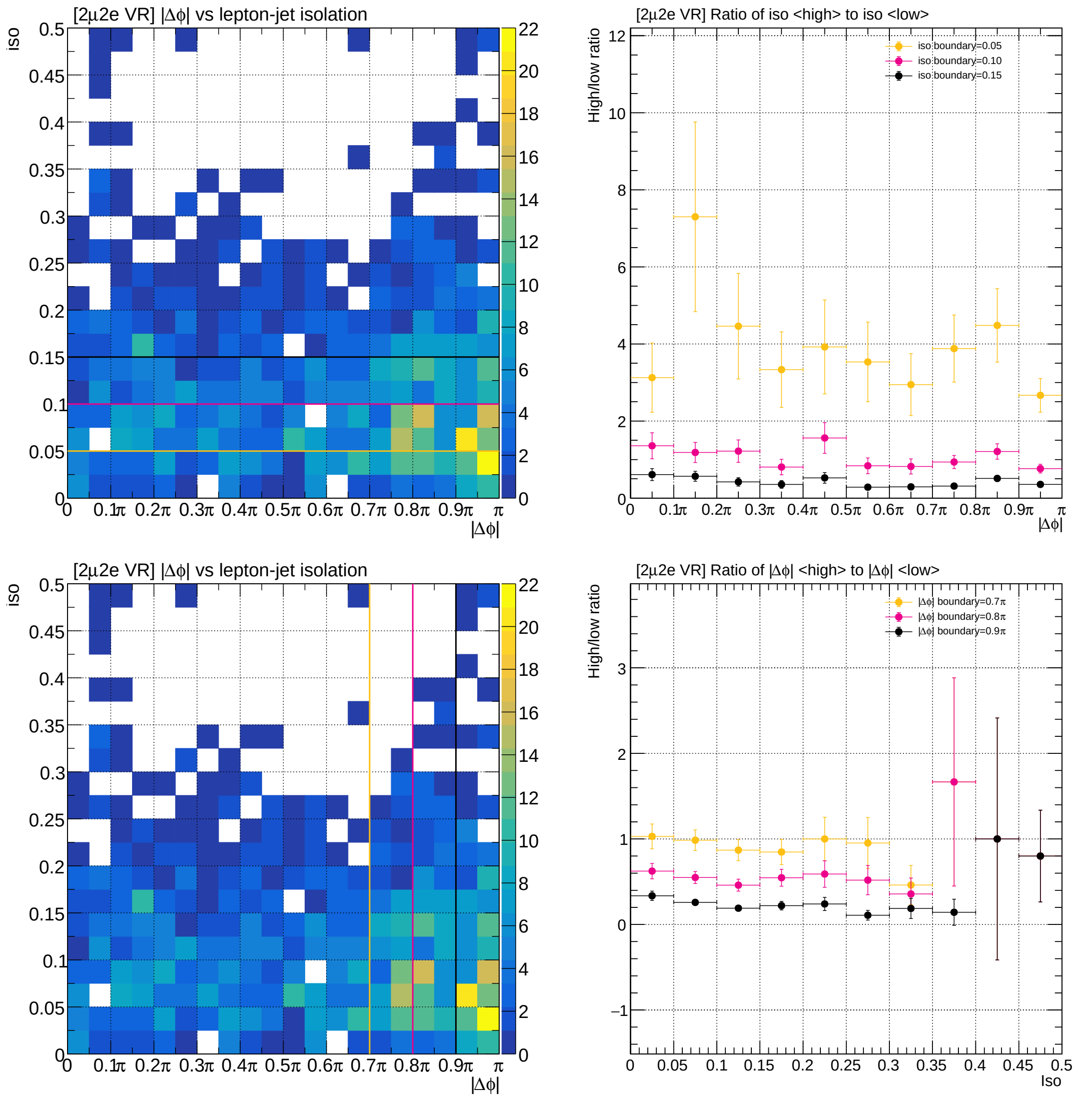

Figure 3.27: Correlation check between the two variables used to construct the ABCD plane for channel $2\mu2$e. *Top right*, ratio between EGM-type lepton-jet isolation (Iso) $\geqslant$ and $< 0.05, 0.1, 0.15$ as a function of $|\Delta\phi|$. *Bottom right*, ratio between $|\Delta\phi| \geqslant$ and $< 0.7\pi, 0.8\pi, 0.9\pi$ as a function of Iso.

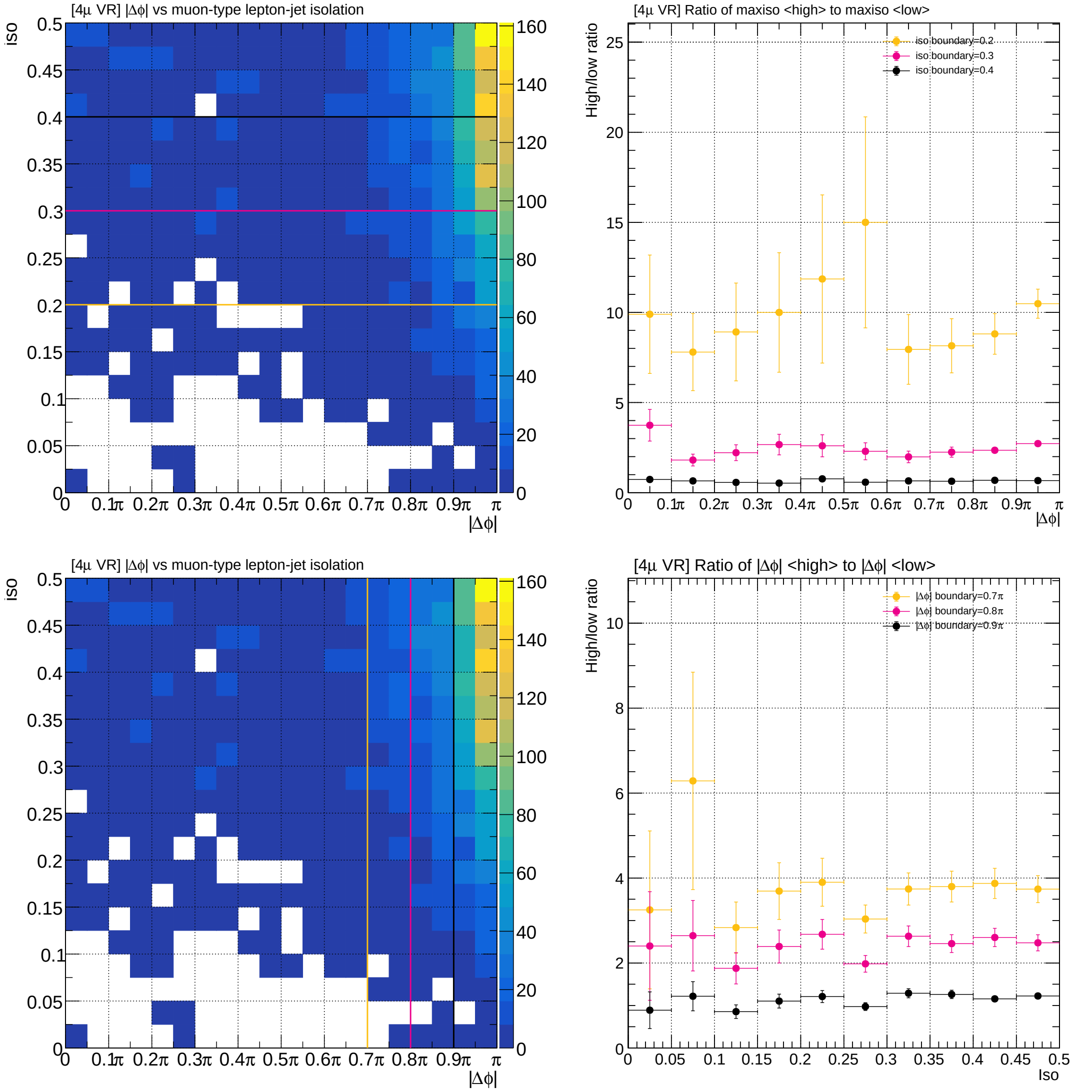

Figure 3.28: Correlation check between the two variables used to construct the ABCD plane for channel 4μ. *Top right*, ratio between muon-type lepton-jet isolation (Iso) $\geqslant$ and $<$ $0.2, 0.3, 0.4$ as a function of $|\Delta\phi|$. *Bottom right*, ratio between $|\Delta\phi|$ $\geqslant$ and $< 0.7\pi, 0.8\pi, 0.9\pi$ as a function of Iso.

$\lvert\Delta\phi\rvert$	Iso	N_A	N_B	N_C	N_D^{obs}	N_D^{pred}	$\lvert N_D^{\text{obs}} - N_D^{\text{pred}}\rvert / N_D^{\text{obs}}$
0.7π	0.05	388	354	100	103 ± 10.15	91.24 ± 11.32	11.4%
0.7π	0.10	253	221	235	236 ± 15.36	205.28 ± 23.16	13.0%
0.7π	0.15	146	128	342	329 ± 18.14	299.84 ± 39.76	8.9%
0.8π	0.05	485	257	125	78 ± 8.83	66.24 ± 7.82	15.1%
0.8π	0.10	312	162	298	173 ± 13.15	154.73 ± 17.46	10.6%
0.8π	0.15	175	99	435	236 ± 15.36	246.09 ± 33.12	4.3%
0.9π	0.05	606	136	152	51 ± 7.14	34.11 ± 4.26	33.1%
0.9π	0.10	393	81	365	106 ± 10.30	75.23 ± 9.99	29.0%
0.9π	0.15	225	49	533	138 ± 11.75	116.08 ± 18.98	15.9%

Table 3.21: Event counts in the ABCD plane for the validation region of the $2\mu 2e$ channel. The uncertainties on the yields in D are statistical only.

$\lvert\Delta\phi\rvert$	Iso	N_A	N_B	N_C	N_D^{obs}	N_D^{pred}	$\lvert N_D^{\text{obs}} - N_D^{\text{pred}}\rvert / N_D^{\text{obs}}$
0.7π	0.2	762	2808	80	286 ± 16.91	294.80 ± 35.09	3.1%
0.7π	0.3	589	2231	253	863 ± 29.38	958.31 ± 74.84	11.0%
0.7π	0.4	326	1239	516	1855 ± 43.07	1961.12 ± 149.52	5.7%
0.8π	0.2	1031	2539	113	253 ± 15.91	278.28 ± 28.12	10.0%
0.8π	0.3	798	2022	346	770 ± 27.75	876.71 ± 59.71	13.9%
0.8π	0.4	443	1122	701	1670 ± 40.87	1775.44 ± 120.09	6.3%
0.9π	0.2	1630	1940	181	185 ± 13.60	215.42 ± 17.57	16.4%
0.9π	0.3	1266	1554	545	571 ± 23.90	668.98 ± 38.24	17.2%
0.9π	0.4	714	851	1097	1274 ± 35.69	1307.49 ± 77.21	2.6%

Table 3.22: Event counts in the ABCD plane for the validation region of the 4μ channel. The uncertainties on the yields in D are statistical only.

3.6.3 Closure tests

To check the closure of the ABCD method, the number of events in each region is summarized in table 3.21 for channel $2\mu 2e$ and in table 3.22 for channel 4μ. The uncertainties are statistical only. Within uncertainty of 35%, the method closes.

Then we use the same initial values for the lepton-jet isolation (0.1/0.2 for channel 2μ2e/4μ) and $\lvert\Delta\phi\rvert$ (2.2) to separate the validation events into regions in the ABCD plane as the starting point for the following optimization in section 3.6.5 and section 3.6.6.

3.6.4 Validation region Data/MC plots

Figure 3.29 shows Data/MC comparisons for some variables of interest, including number of tight b-jets, isolation and $|\Delta\phi|$ variables etc., of channel $2\mu2e$ in the validation region.

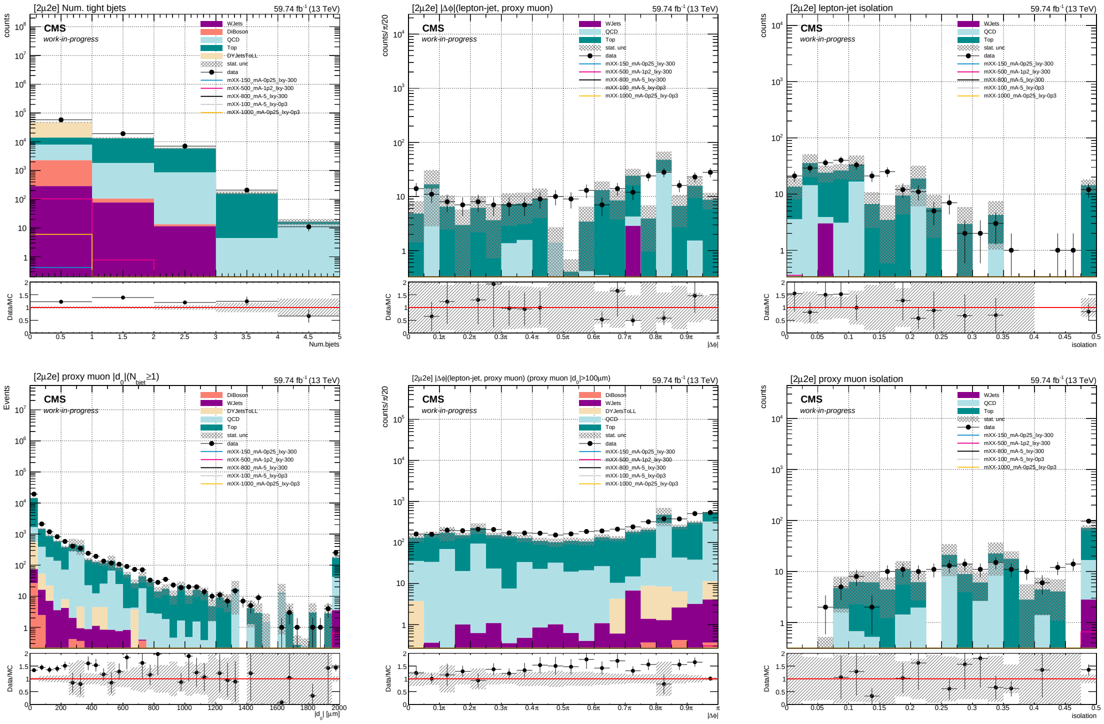

Figure 3.29: Data/MC distributions of channel $2\mu2e$ in the validation region. *Top* row - *left*: number of "tight" b-jets in the event; *middle*: $|\Delta\phi|$(lepton-jet, proxy muon) when `mind0`$>$ 1.5 mm; *right*: $\mathrm{Iso}_{\text{lepton-jet}}$ when `mind0`$>$ 1.5 mm. *Bottom* row - *left*: lepton-jet `mind0` when $N_{b\text{-jet}} \geqslant 1$; *middle*: $|\Delta\phi|$(lepton-jet, proxy muon) when `mind0`$>$ 0.1 mm; *right*: $\mathrm{Iso}_{\text{proxy-muon}}$ when `mind0`$>$ 1.5 mm.

Figure 3.30 shows Data/MC comparisons for the same set of variables of channel 4μ in the validation region.

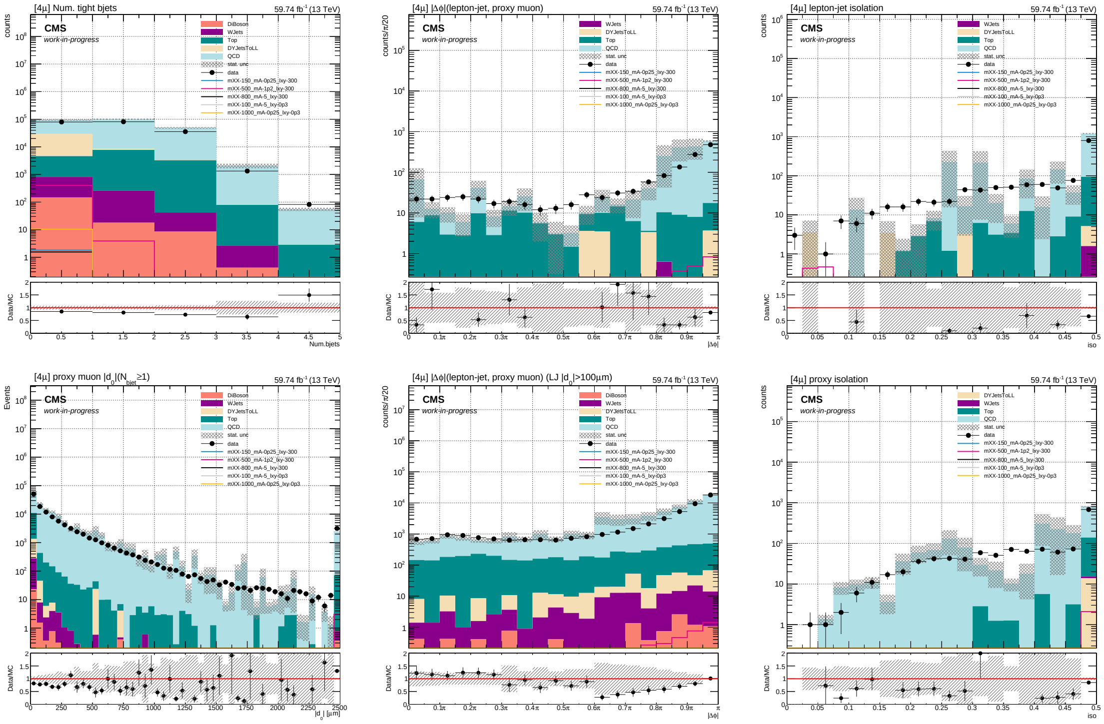

Figure 3.30: Data/MC distributions of channel 4μ in the validation region. *Top* row - *left*: number of "tight" b-jets in the event; *middle*: $|\Delta\phi|$(lepton-jet, proxy muon) when `mind0`$>$ 1 mm; *right*: $\mathrm{Iso}_{\text{lepton-jet}}$ when `mind0`$>$ 1 mm. *Bottom* row - *left*: lepton-jet `mind0` when $N_{b\text{-jet}} \geqslant 1$; *middle*: $|\Delta\phi|$(lepton-jet, proxy muon) when `mind0`$>$ 0.1 mm; *right*: $\mathrm{Iso}_{\text{proxy-muon}}$ when `mind0`$>$ 1 mm.

3.6.5 Optimization of the displacement cut

The displacement cut introduced in section 3.5.3 is important to reduce SM prompt background events and to enhance displaced signal sensitivities. In this section, we discuss the optimization of this displacement cut for each channel, which include the choice of the variable and the corresponding optimal cut value.

The displacement cut variable

As mentioned in section 3.5.3, variables associated with muon track's $|d0|$ inside the muon-type lepton-jet are preferred over the vertex-related variables due to the additional vertexing efficiency loss. Here we consider two variable categories: $|d0|$ and $d0$ significance ($|d0|/\sigma_{d0}$). As both variables are associated with a single track, to promote as a quantity representing a muon-type lepton-jet (containing $\geqslant$ 2 tracks), the minimal, average and maximum value among all tracks inside a lepton-jet are evaluated for comparison. They are denoted as `mind0`, `aved0`, `maxd0` and `mind0sig`, `aved0sig`, `maxd0sig`, respectively.

Figure 3.31 displays the distributions (top row) and significance (forward $s/\sqrt{b}$, bottom row) for `mind0`, `aved0`, `maxd0` (left to right) of the muon-type lepton-jet for channel $2\mu 2e$. After comparison, `mind0` is preferred among the three because it gives higher significance for most signal points. Figure 3.32 displays the distributions (top row) and significance (forward $s\sqrt{b}$, bottom row) for `mind0sig`, `aved0sig`, `maxd0sig` (left to right) of the muon-type lepton-jet for channel $2\mu 2e$. The significance curves for these three variables

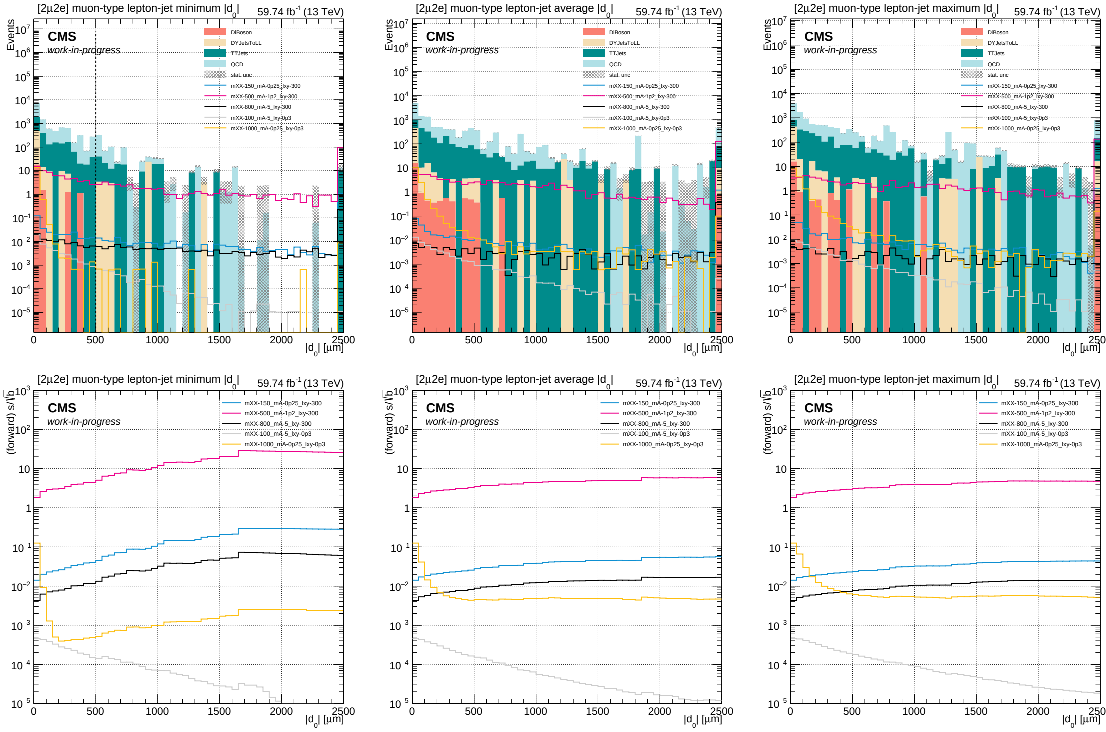

Figure 3.31: Displacement variables associated with the track $|d_0|$ of muon-type lepton-jets for channel $2\mu 2$e. On the *top* row, the distributions of minimum, average and maximum $|d_0|$ are displayed from left to right. On the *bottom* row, forward $s/\sqrt{b}$ of corresponding variables are displayed from *left* to *right*.

are quite similar. We use the `mind0sig` as a representative to compare against `mind0` to determine the final choices.

Figure 3.33 displays the distributions (top row) and significance (forward $s\sqrt{b}$, bottom row) for `mind0` and `mind0sig` (left to right) of the muon-type lepton-jet for channel $2\mu 2e$. After comparison, `mind0` is determined to be the optimal displacement variable for this channel becaus of its higher significance.

Figure 3.34 displays the distributions (top row) and significance (forward $s/\sqrt{b}$, bottom row) for the maximum `mind0`, `aved0`, `maxd0` (left to right) of the two muon-type

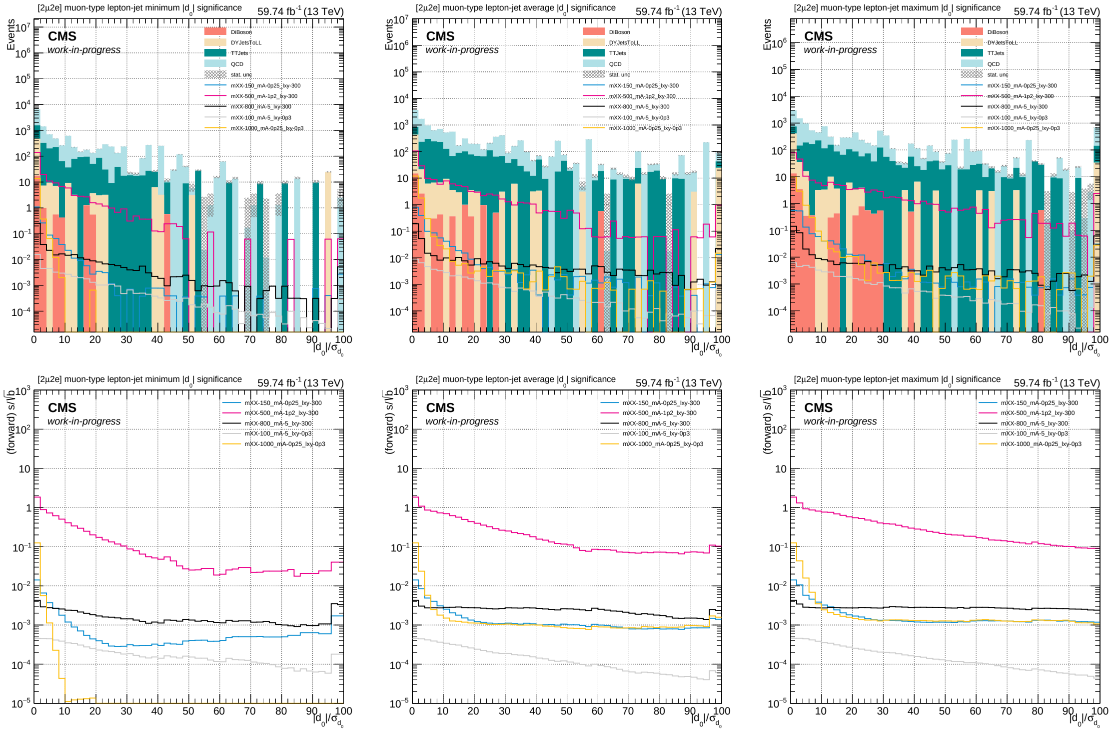

Figure 3.32: Displacement variables associated with the track d_0 significance of muon-type lepton-jets for channel 2μ2e. On the *top* row, the distributions of minimum, average and maximum d_0 significance are displayed from *left* to *right*. On the *bottom* row, forward $s/\sqrt{b}$ of corresponding variables are displayed from *left* to *right*.

lepton-jets for channel 4μ. After comparison, `mind0` is preferred out of the three because it gives higher significance for most signal points. Figure 3.35 displays the distributions (top row) and significance (forward $s\sqrt{b}$, bottom row) for maximum `mind0sig`, `aved0sig`, `maxd0sig` (left to right) of the two muon-type lepton-jets for channel 4μ. The significance curves for these three variables are quite similar. We use the `mind0sig` as a representative to compare against `mind0` to determine the final choices.

Figure 3.36 displays the distributions (top row) and significance (forward $s\sqrt{b}$, bottom row) of maximum `mind0` and `mind0sig` (left to right) of the two muon-type lepton-

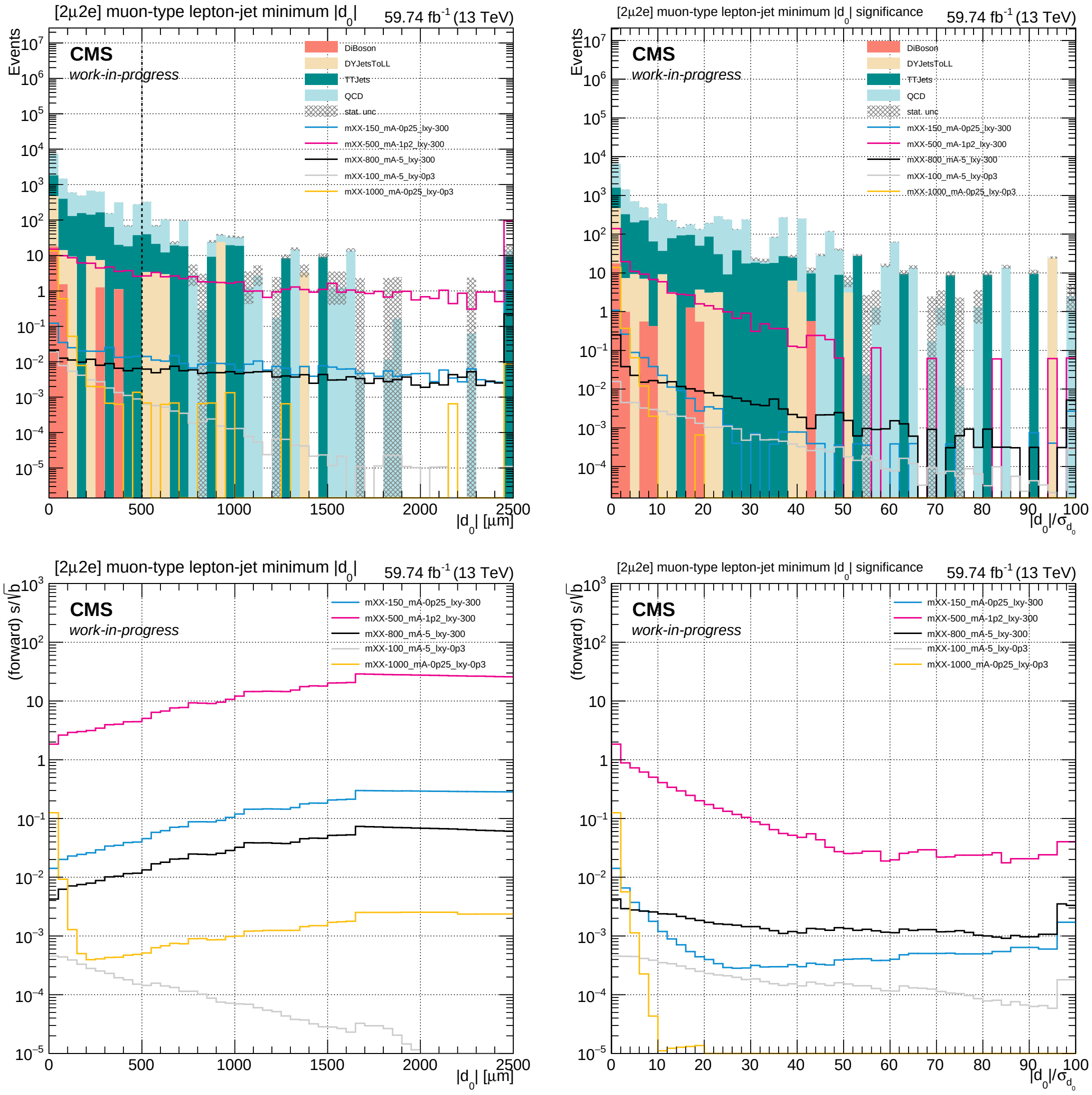

Figure 3.33: Muon-type lepton-jet $|d_0|$ (*top left*) and d_0 significance (*top right*) distributions for channel 2μ2e. Forward $s/\sqrt{b}$ distributions are included in the *bottom*, *left* for $|d_0|$ and *right* for d_0 significance.

jets for channel 4μ. After comparison, `mind0` is determined to be the displacement variable for this channel due to higher significance.

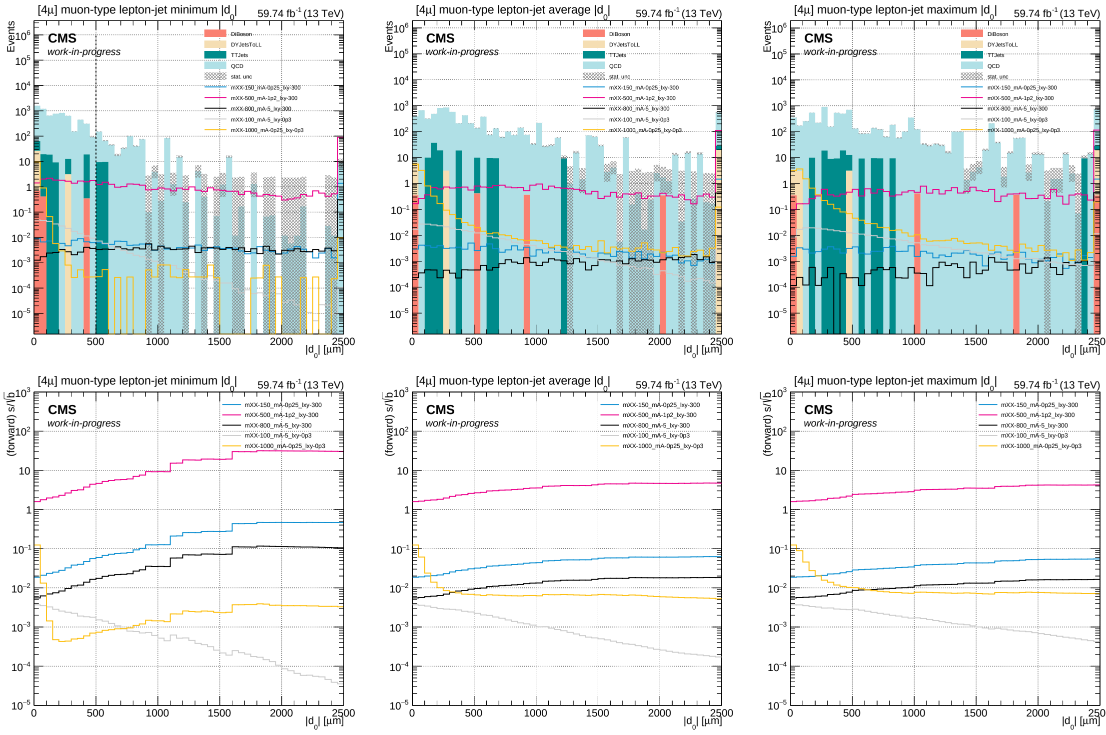

Figure 3.34: Displacement variables associated with track $|d_0|$ of the more displaced muon-type lepton-jet for channel 4μ. On the *top* row, the distributions of minimum, average and maximum $|d_0|$ are displayed from left to right. On the *bottom* row, forward $s/\sqrt{b}$ of corresponding variables are displayed from *left* to *right*.

In summary, we use the `mind0` variable for the purpose of applying a displacement cut for both channels. For the $2\mu 2e$ channel, we use the muon-type lepton-jet's `mind0`; for the 4μ channel, we use the maximum `mind0` of the two muon-type lepton-jets.

The displacement cut value

Due to the limited statistics of the background MC in the displaced regioin, the optimal cut value for the displacement variable `mind0` is determined by making use of proxy events in the validation region (described in section 3.6.2) in data. We take the `mind0` shape of the muon-type lepton-jets in proxy events of the 4μ channel as the background shape

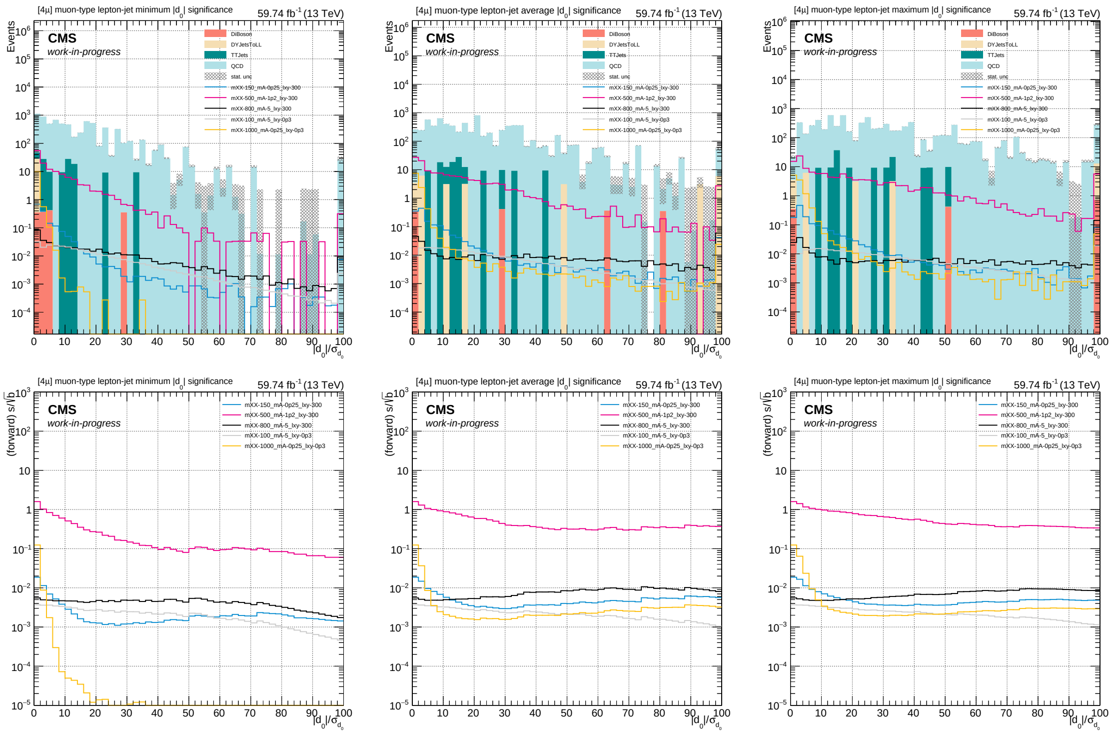

Figure 3.35: Displacement variables associated with track d_0 significance of the more displaced muon-type lepton-jet for channel 4μ. On the *top* row, the distributions of minimum, average and maximum d_0 significance are displayed from left to right. On the *bottom* row, forward $s/\sqrt{b}$ of corresponding variables are displayed from *left* to *right*.

and normalize the distribution to the signal region. We then calculate the cut significance with the asymptotic discovery significance Z_A (equation (3.8), from [135]):

$$Z_A = \sqrt{2\left((s+b)\ \ln\left[\frac{(s+b)(b+\sigma_b^2)}{b^2+(s+b)\sigma_b^2}\right] - \frac{b^2}{\sigma_b^2}\ \ln\left[1+\frac{\sigma_b^2 s}{b(b+\sigma_b^2)}\right]\right)} \tag{3.8}$$

, where s is the number of signal events in signal region D, b is the number of proxy events in validation region D, and σ_b is the uncertainty from proxy events in validation region A, B, C:

$$\sigma_b = b \times \sqrt{\frac{1}{N_A^{\mathrm{VR}}} + \frac{1}{N_B^{\mathrm{VR}}} + \frac{1}{N_C^{\mathrm{VR}}}}$$

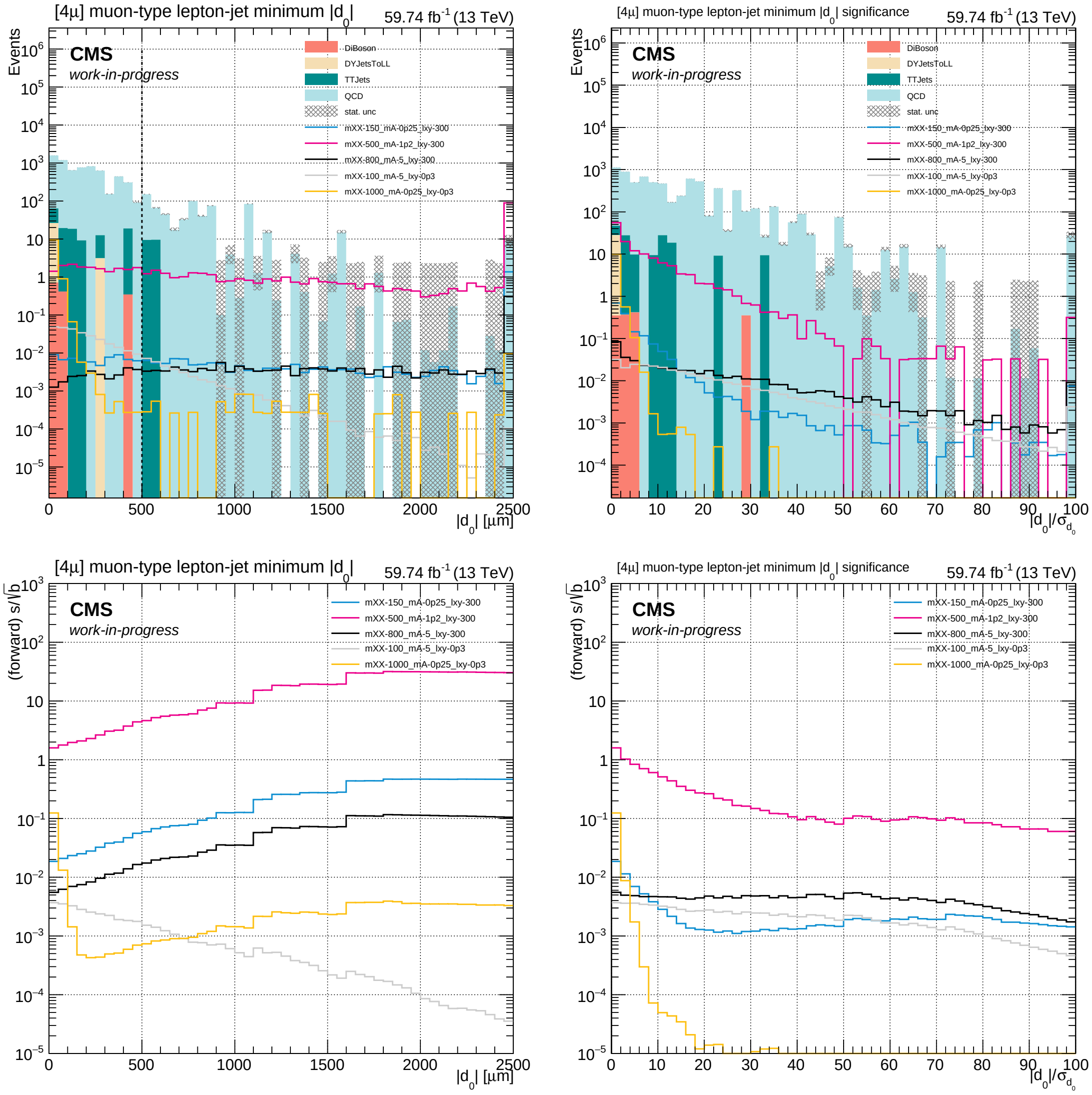

Figure 3.36: Maximum muon-type lepton-jet $|d_0|$ (*top left*) and max d_0 significance (*top right*) distributions for channel 4μ. Forward $s/\sqrt{b}$ distributions are included in the *bottom*, *left* for $|d_0|$ and *right* for d_0 significance.

The ABCD regions are separated by initial boundaries as described in section 3.6.3: Iso=0.1 (0.2) for the $2\mu2e$ (4μ) channels and $|\Delta\phi| = 2.2$ in both channels.

Figure 3.37 displays the `mind0` distribution of muon-type lepton-jets in proxy events for the 4μ channel. The blue data points correspond to inclusive events and the

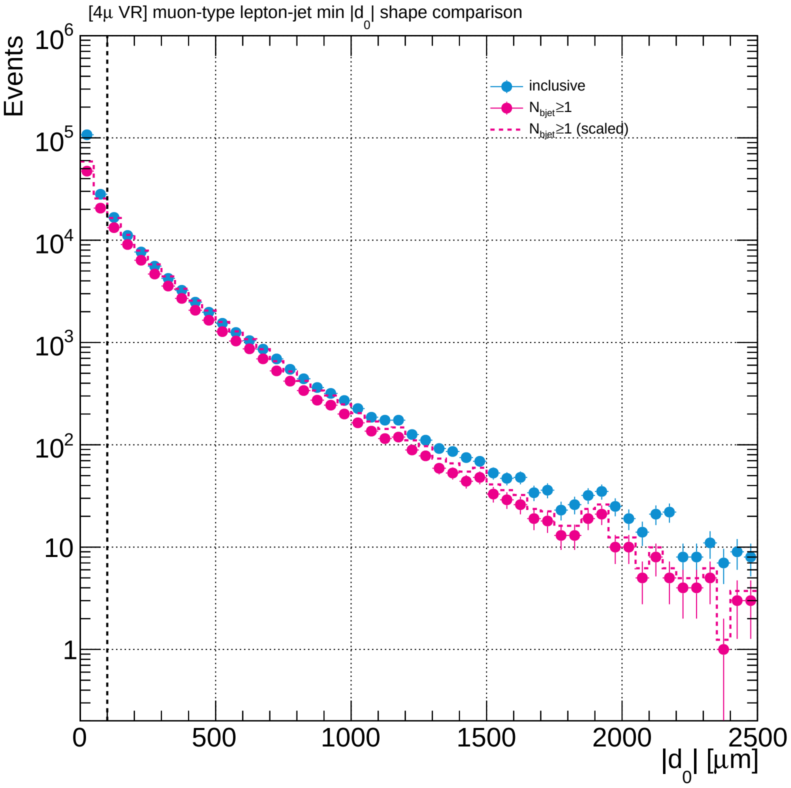

Figure 3.37: Distributions of muon-type lepton-jet $|d0|$ from proxy events of channel 4μ. The inclusive distribution is marked by blue dots, and events with > 0 b-jets are marked by pink dots. The distribution in pink is scaled up in the pink dashed line to show that the distributions after $|d0| > 0.1$ mm are comparable between the two, which justifies 0.1 mm as a starting point for the displacement cut optimization.

pink data points correspond to events with $\geqslant 1$ b-jets tagged. As shown from figure 3.26, events with 0 b-jets tagged have large contribution from DY+jets process and events with $\geqslant 1$ b-jets tagged are dominated by QCD/$t\bar{t}$+jets processes and mininal DY+jets contribution. By scaling up the pink data points, we can see the distributions of blue dots and pink dashed line are comparable starting from 0.1 mm, which suggests 0.1 mm as a starting point for the displacement cut optimization. We take the shape of pink dots after 0.1 mm as the background shape for the following significance calculation.

The normalization factor comes from the ratio of the number of events between signal region and validation region in the low $|\Delta\phi|$ region, as in equation (3.9):

$$N = \text{Tot}_{\text{VR}} \times \frac{(|\Delta\phi| < 2.2)_{\text{SR}}}{(|\Delta\phi| < 2.2)_{\text{VR}}} \tag{3.9}$$

For channel $2\mu 2e$, we have

$$N_{2\mu 2e} = 4759 \times \frac{1591}{2476} \sim 2939.3$$

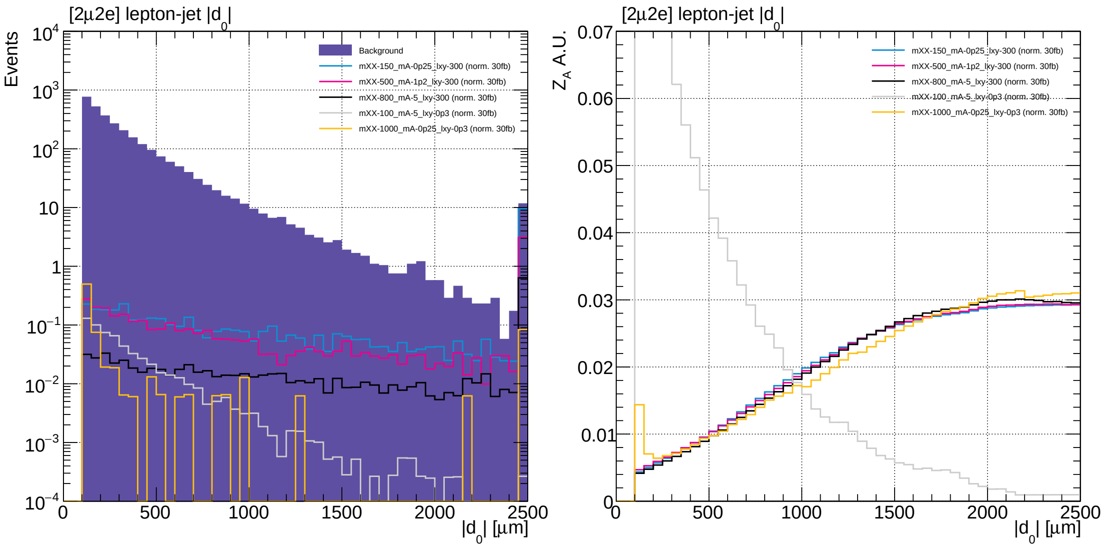

Figure 3.38: Muon-type lepton-jet $|d0|$ distribution (*left*) for channel 2μ2e. Normalized Z_A distribution (*right*). The background shape is taken from the muon-type lepton-jet's $|d0|$ distribution in proxy events for the $2\mu 2e$ channel and scaled to the signal region.

Figure 3.38 displays the distributions of the signal and background distributions on the left and significance Z_A on the right. For most signals, starting from 1.5 mm, the significance curves start to become flat, which indicates 1.5 mm to be an optimal cut for this channel.

For channel 4μ, we have

$$N_{4\mu} = 30142 \times \frac{374}{6717} \sim 1678.3$$

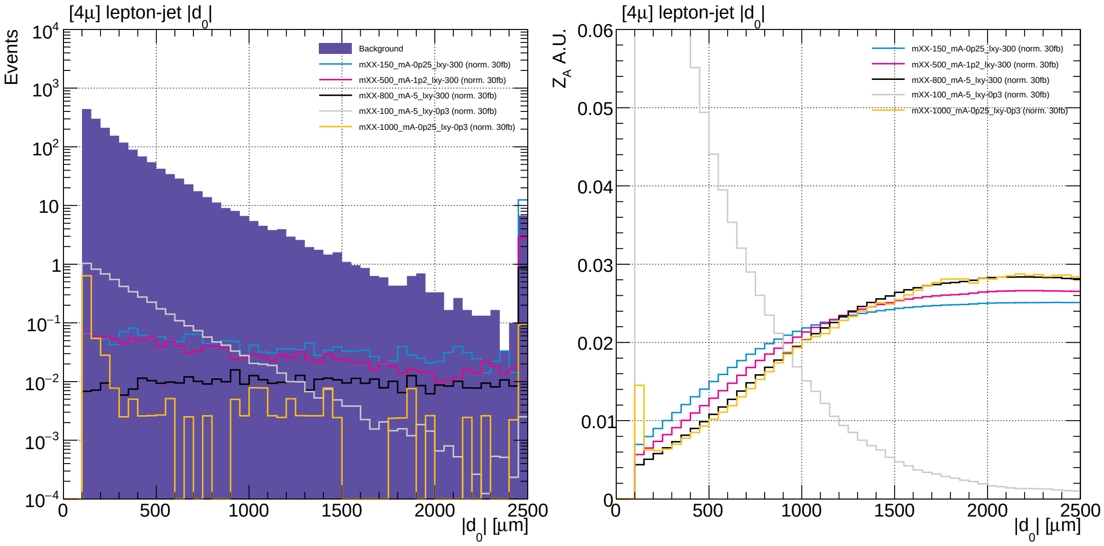

Figure 3.39: Maximum muon-type lepton-jet $|d0|$ distribution (*left*) for channel 4μ. Normalized Z_A distribution (*right*). The background shape is taken from the muon-type lepton-jet's $|d0|$ distribution in proxy events for the 4μ channel and scaled to the signal region.

Figure 3.39 displays the distributions of the signal and background distributions on the left and significance Z_A on the right. For most signals, starting from 1 mm, the significance curves start to become flat, which indicates 1 mm to be an optimal cut for this channel.

In summary, the optimal `mind0` cut value is 1.5 mm for channel $2\mu 2e$, and 1 mm for channel 4μ. As a reminder, for channel $2\mu 2e$, it is the `mind0` of the muon-type lepton-jet; for channel 4μ, it is the maximum `mind0` of the two muon-type lepton-jets.

3.6.6 Optimization of ABCD boundaries

The boundaries that define the ABCD regions are optimized per signal point to maximize the analysis sensitivity. The optimization procedure uses the data in the validation region and the signal MC in the signal region. The data in the VR is normalized to the data yields in the signal region using the ratio of event yields for the signal region to the yields in the VR for $|\Delta\phi| < 2.2$ after applying the displacement cut. This is equivalent to the procedure for optimizing the displacement cut. The scaled ABCD distributions in the validation regions are shown on the left in figure 3.40 and figure 3.41 for channel 2μ2e and channel 4μ, respectively.

As part of the optimization procedure, we want to ensure that there will be a reasonable number of events remaining in each region after the boundaries are defined. To guarantee this, we limit the optimization region as the area where at least 3 events are present in regions A, B, and C when the boundaries are defined. Both VR and SR ($|\Delta\phi| < 2.2$) are used to define the optimization region. In region $|\Delta\phi| < 2.2$, the intersection between the result from VR and the result from SR are used, in region $|\Delta\phi| > 2.2$, the result from VR is used. The combined optimization region is shown on the right in figure 3.40 for the 2μ2e channel and figure 3.41 for the 4μ channel.

To optimize the ABCD bins, we use the asymptotic approximation of discovery sensitivity based on Asimov datasets [135] as a proxy of the optimal exclusion sensitivity (equation (3.8)). For this optimization, b is the bin's predicted background yield, σ_b is the uncertainty on that prediction, and s is the expected signal yield. The usual expression

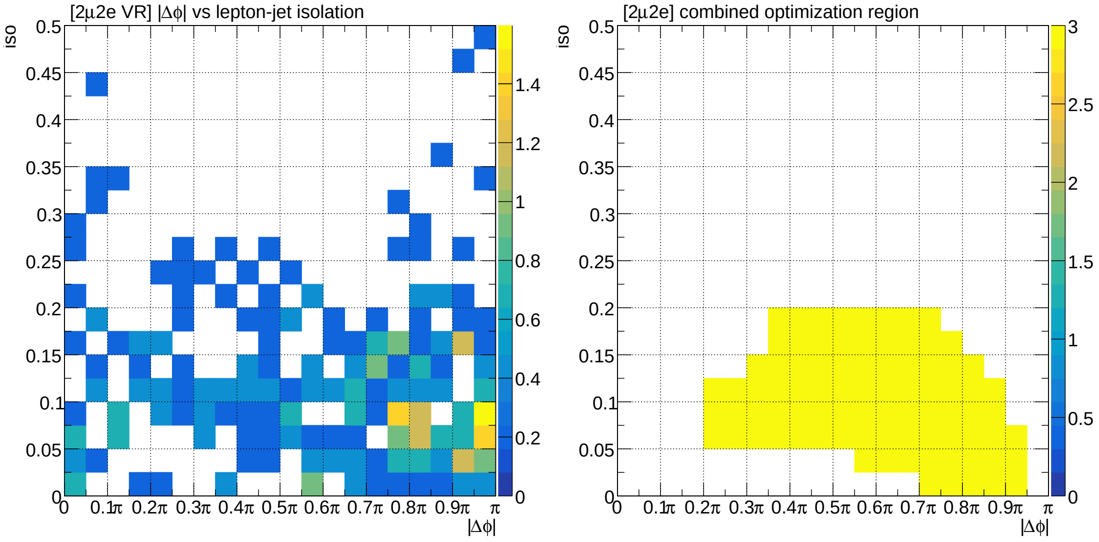

Figure 3.40: ABCD distribution in the validation region for channel $2\mu2$e, scaled to SR (*left*). The combined optimization region (*right*), where N_A, N_B, N_C all have $\geqslant 3$ events when boundaries are defined.

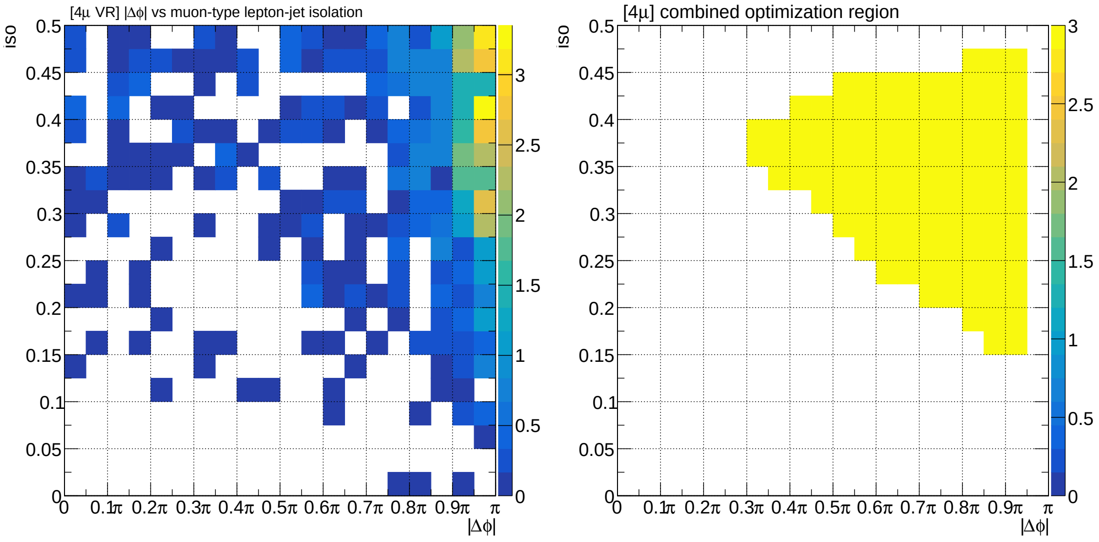

Figure 3.41: ABCD distribution in the validation region for channel 4μ, scaled to SR (left). The combined optimization region (right), where N_A, N_B, N_C all have $\geqslant 3$ events when boundaries are defined inside.

$s/\sqrt{s+b}$ used to estimate sensitivity is not particularly adequate here because it does not include any uncertainties, so it can not only overestimate the sensitivity, but also shift the optimal bin edges away from their true location. Equation (3.8) reduces to its more well-known forms in the limit of zero uncertainty and of small s/b ratios:

$$\sigma_b \to 0 \Rightarrow Z_A = \sqrt{2\left[(s+b)\ln\left(1+\frac{s}{b}\right) - s\right]}, \tag{3.10}$$

$$s \ll b \Rightarrow Z_A = \frac{s}{\sqrt{b}}. \tag{3.11}$$

The error σ_b is taken as the uncertainty on the prediction due to Poisson fluctuations in bins A, B, and C:

$$\sigma_b = b \times \sqrt{\frac{1}{N_A^{\text{pred}}} + \frac{1}{N_B^{\text{pred}}} + \frac{1}{N_C^{\text{pred}}}}. \tag{3.12}$$

, where N_A^{pred}, N_B^{pred}, and N_C^{pred} are the predicted yields in regions A, B, and C (for a given set of boundaries) using the VR normalized to the SR, as described above.

For the 2μ2e channel, figure 3.42 shows the ABCD distributions from the scaled data in the VR and the distributions from several representative signal MC samples and the optimal boundaries found per signal point. Figure 3.43 shows the Asimov significance Z_A in the optimization area, where each bin represents the significance if the ABCD boundaries passed through that point. The optimal values are identified by open crosses in the plot. The corresponding plots for the 4μ channel are shown in figure 3.44 and figure 3.45.

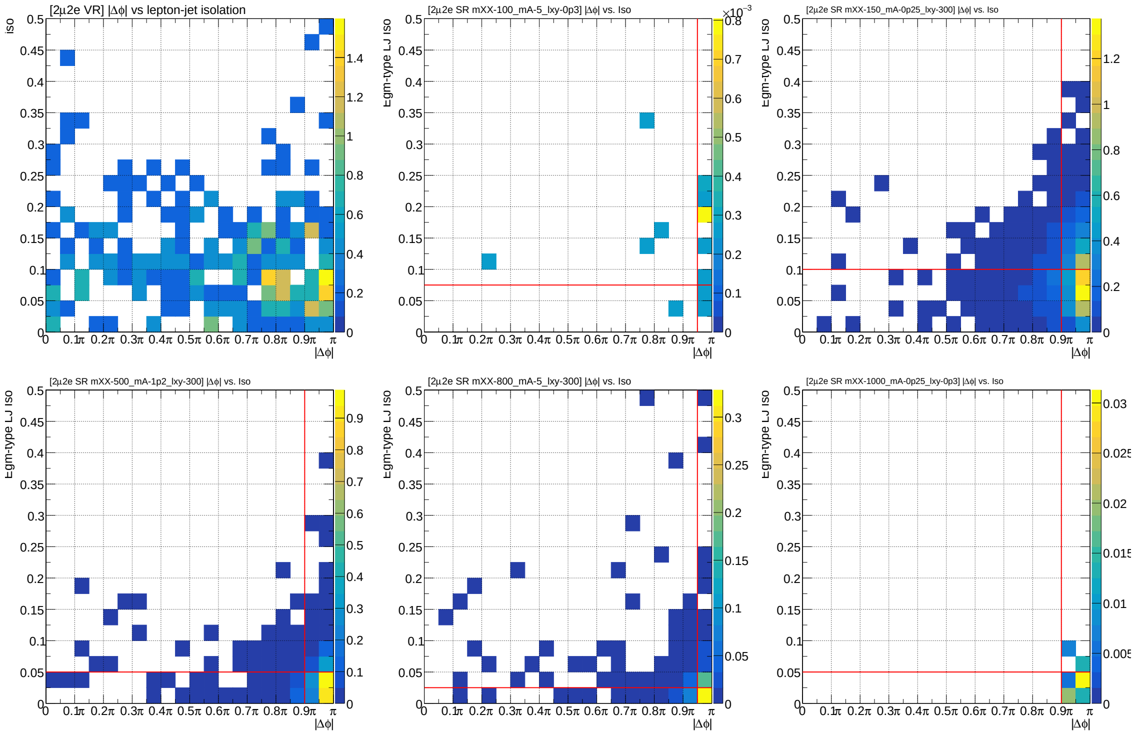

Figure 3.42: ABCD distribution in the validation region for channel 2μ2e, scaled to SR (*top left*), and ABCD distributions in the signal regions for various signal MC (the remaining five plots). The red lines indicate the optimal boundaries.

After the boundary optimization procedure is repeated for all signal parameter points, it turns out that many signal points result in common or very close optimized boundaries due to similar signal distributions in the ABCD plane after the selection. To simplify the boundary definitions without affecting the significance much, we categorize all the signal points into 3 boundary combinations for the 4μ channel and 2 boundary combinations for the 2$\mu 2e$ channel. They are listed in table 3.23. The association between the signal sample and the boundary is shown in section 3.6.6 for the 4μ channel and in section 3.6.6 for the 2$\mu 2e$ channel.

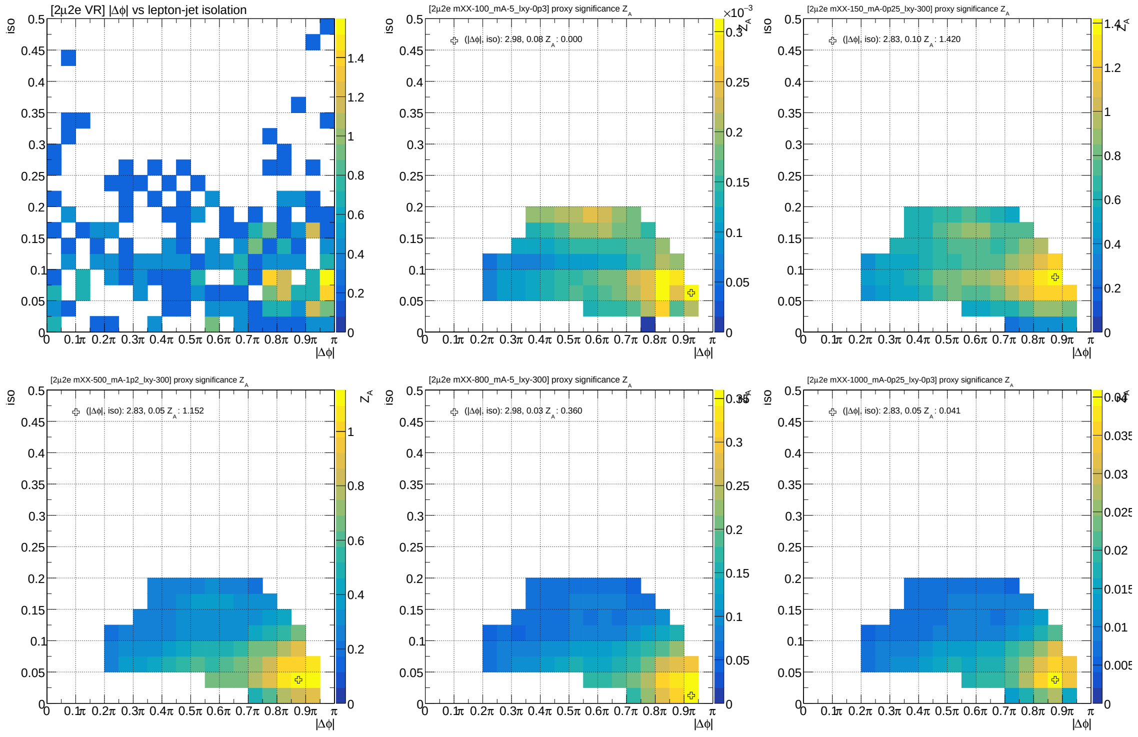

Figure 3.43: ABCD distribution in the validation region for channel 2μ2e, scaled to SR (*top left*), and the Z_A distributions in the signal regions for various signal MC (the remaining five plots). Open crosses indicate the highest significance value within the optimization region, which is the intersection of the optimal ABCD boundaries.

Channel	Boundary ($\Delta\phi$, Iso)
$2\mu 2e$	(0.9π, 0.05)
	(0.9π, 0.10)
4μ	(0.9π, 0.20)
	(0.9π, 0.25)
	(0.9π, 0.30)

Table 3.23: Optimized boundaries for both search channels

3.7 Systematic uncertainties

The dominant systematic uncertainty is the closure uncertainty associated with how well the background prediction method matches the observed rate in the orthogonal validation region. Also, there are systematic uncertainties associated with the lepton iden-

$m_{\chi\bar{\chi}}$ [GeV]	m_{Z_d} [GeV]	Z_d $c\tau$ [mm]				
		0.3 cm	3 cm	30 cm	150 cm	300 cm
100	0.25	🟥 0.02	🟦 0.2	🟩 2	🟩 10	🟩 20
	1.2	🟥 0.096	🟦 0.96	🟦 9.6	🟩 48	🟩 96
	5	🟦 0.4	🟦 4	🟦 40	🟩 200	🟩 400
150	0.25	🟦 0.013	🟦 0.13	🟦 1.3	🟦 6.7	🟦 13
	1.2	🟦 0.064	🟦 0.64	🟦 6.4	🟦 32	🟦 64
	5	🟦 0.27	🟦 2.7	🟦 27	🟦 130	🟦 270
200	0.25	🟦 0.01	🟦 0.1	🟦 1	🟦 5	🟦 10
	1.2	🟦 0.048	🟦 0.48	🟦 4.8	🟦 24	🟦 48
	5	🟦 0.2	🟦 2	🟦 20	🟦 100	🟦 200
500	0.25	🟦 0.004	🟦 0.04	🟦 0.4	🟦 2	🟦 4
	1.2	🟦 0.019	🟦 0.19	🟦 1.9	🟦 9.6	🟦 19
	5	🟦 0.08	🟦 0.8	🟦 8	🟦 40	🟦 80
800	0.25	🟦 0.0025	🟦 0.025	🟦 0.25	🟦 1.2	🟦 2.5
	1.2	🟦 0.012	🟦 0.12	🟦 1.2	🟦 6	🟦 12
	5	🟦 0.05	🟦 0.5	🟦 5	🟦 25	🟦 50
1000	0.25	🟦 0.002	🟦 0.02	🟦 0.2	🟦 1	🟦 2
	1.2	🟦 0.0096	🟦 0.096	🟦 0.96	🟦 4.8	🟦 9.6
	5	🟦 0.04	🟦 0.4	🟦 4	🟦 20	🟦 40

Boundary ($\Delta\phi$, Iso): 🟦 (0.9π, 0.2) 🟩 (0.9π, 0.25) 🟥 (0.9π, 0.3)

Table 3.24: The association between the signal sample and the boundary for channel 4μ. The boundary choices are color coded.

$m_{\chi\bar{\chi}}$ [GeV]	m_{Z_d} [GeV]	Z_d $c\tau$ [mm]				
		0.3 cm	3 cm	30 cm	150 cm	300 cm
100	0.25	0.02	🟨 0.2	🟨 2	🟨 10	🟨 20
	1.2	0.096	🟨 0.96	🟨 9.6	🟨 48	🟨 96
	5	🟨 0.4	🟨 4	🟨 40	🟨 200	🟨 400
150	0.25	🟨 0.013	🟨 0.13	🟨 1.3	🟨 6.7	🟨 13
	1.2	0.064	🟨 0.64	🟨 6.4	🟨 32	🟨 64
	5	🟨 0.27	🟨 2.7	🟨 27	🟨 130	🟨 270
200	0.25	🟨 0.01	🟨 0.1	🟨 1	🟨 5	🟨 10
	1.2	🟨 0.048	🟨 0.48	🟨 4.8	🟨 24	🟨 48
	5	🟨 0.2	🟨 2	🟨 20	🟨 100	🟨 200
500	0.25	🟥 0.004	🟥 0.04	🟥 0.4	🟥 2	🟥 4
	1.2	🟥 0.019	🟥 0.19	🟥 1.9	🟥 9.6	🟥 19
	5	0.08	🟥 0.8	🟥 8	🟥 40	🟥 80
800	0.25	🟥 0.0025	🟥 0.025	🟥 0.25	🟥 1.2	🟥 2.5
	1.2	🟥 0.012	🟥 0.12	🟥 1.2	🟥 6	🟥 12
	5	0.05	🟥 0.5	🟥 5	🟥 25	🟥 50
1000	0.25	🟥 0.002	🟥 0.02	🟥 0.2	🟥 1	🟥 2
	1.2	🟥 0.0096	🟥 0.096	🟥 0.96	🟥 4.8	🟥 9.6
	5	0.04	🟥 0.4	🟥 4	🟥 20	🟥 40

Boundary ($\Delta\phi$, Iso): 🟥 (0.9π, 0.05) 🟨 (0.9π, 0.1)

Table 3.25: The association between the signal sample and the boundary for channel $2\mu 2e$. The boundary choices are color coded. There are a few prompt signal samples that do not have a colored background because there is no event left after the displacement cut, which therefore yields no significance.

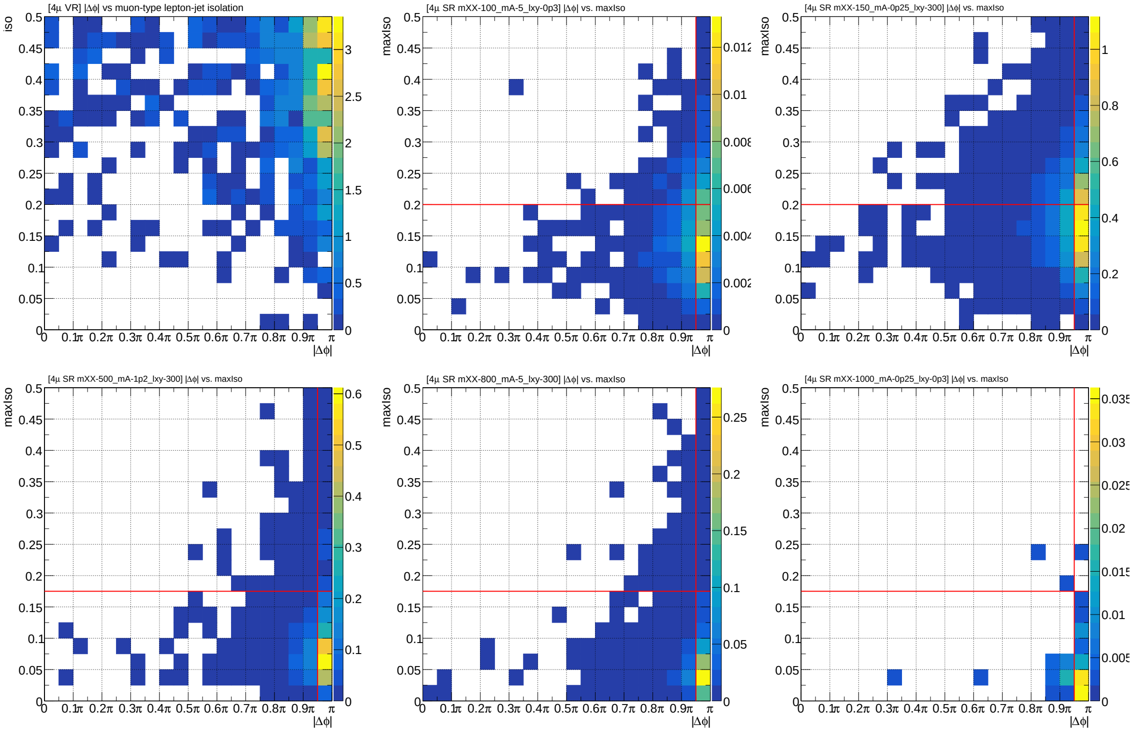

Figure 3.44: ABCD distribution in the validation region for channel 4μ, scaled to SR (*top left*), and ABCD distributions in the signal regions for various signal MC (the remaining five plots). The red lines indicate the optimal boundaries.

tification, which are subdominant and impact the signal predictions from MC. They are the same across all ABCD bins. The treatment of correlations between systematic effects is done according to the official recommended procedures when available.

3.7.1 Luminosity

The uncertainty associated with the measurement of integrated luminosity is taken from the Lumi POG [136] as 2.5% for 2018. This uncertainty is applied to the simulation signal samples when scaling the MC yields to the measured luminosity.

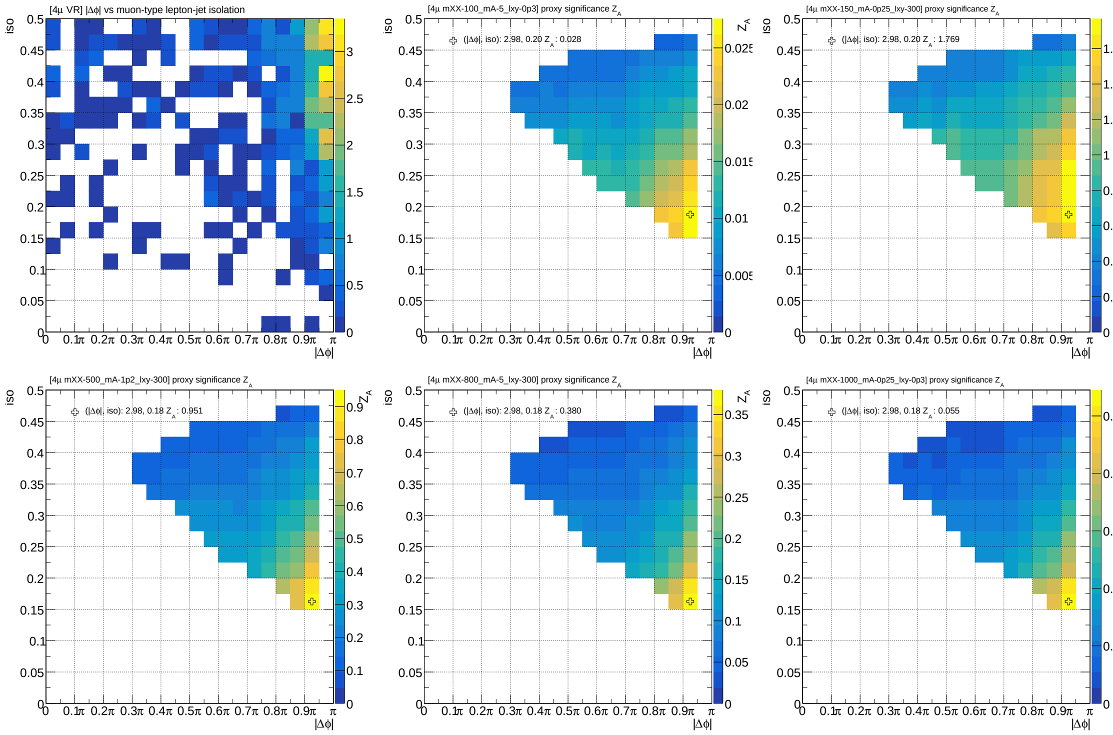

Figure 3.45: ABCD distribution in the validation region for channel 4μ, scaled to SR (*top left*), and the Z_A distributions in the signal regions for various signal MC (the remaining five plots). Open crosses indicate the highest significance value within the optimization region, which is the intersection of the optimal ABCD boundaries.

3.7.2 Lepton ID scale factor

The lepton ID scale factor accounts for the difference between the data and MC simulation when applying the identification criteria. As discussed in section 3.3.2, we employ the results from the POGs for PF electrons, photons and muons at the *loose* working points mostly. Here we also employ the systematic uncertainties associated with those measurements from the POG. (For muons with $p_{\mathrm{T}} < 20\,\mathrm{GeV}$, we use the result from the study performed for the $H \to ZZ \to 4l$ analysis [23].)

Figure 3.46 shows the systematic uncertainty of the scale factor for the cut-based loose electron (left) and photon (right) IDs in a 2D map as a function of its p_{T} and ECAL superCluster η.

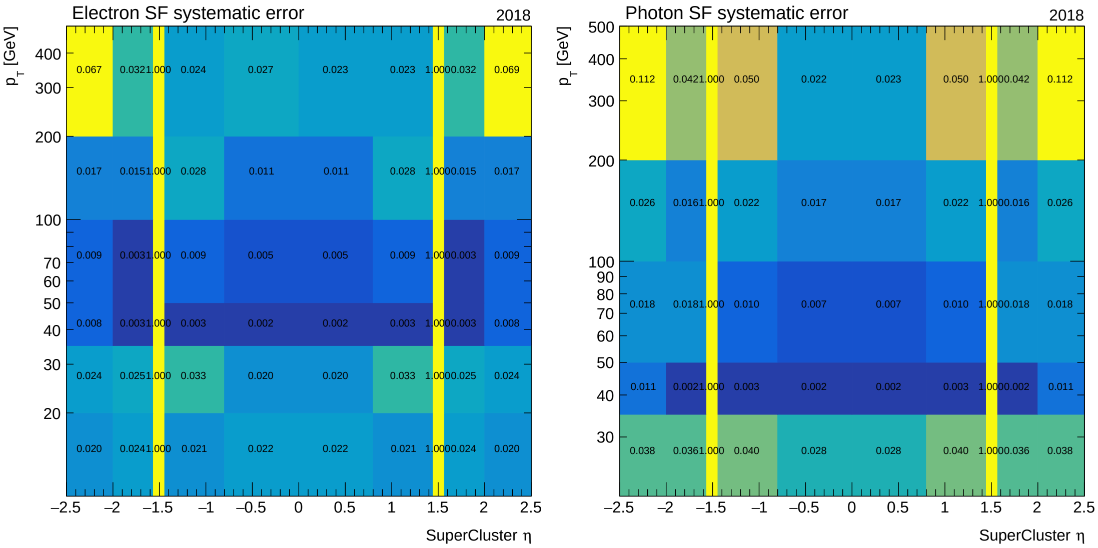

Figure 3.46: Systematic uncertainties for electron (*left*) and photon (*right*) ID scale factors at the "loose" working point as measured by the EGM POG for 2018.

Figure 3.47 shows the systematic uncertainty of the scale factor for the cut-based loose muon ID as a function of muon p_{T} and η.

The uncertainties are propagated by distorting the signal yield in the ABCD plane with varying the lepton ID scale factor ± the systematic uncertainty per object in the two lepton-jets. The distribution of the maximum yield variation percentage of all signal samples (table 3.2) is then obtained. The percent uncertainty that includes 95% of the cumulative distribution is assigned as the systematic uncertainty due to this type of lepton ID scale factor. Figure 3.48 displays the distributions of the percentage difference from the nominal

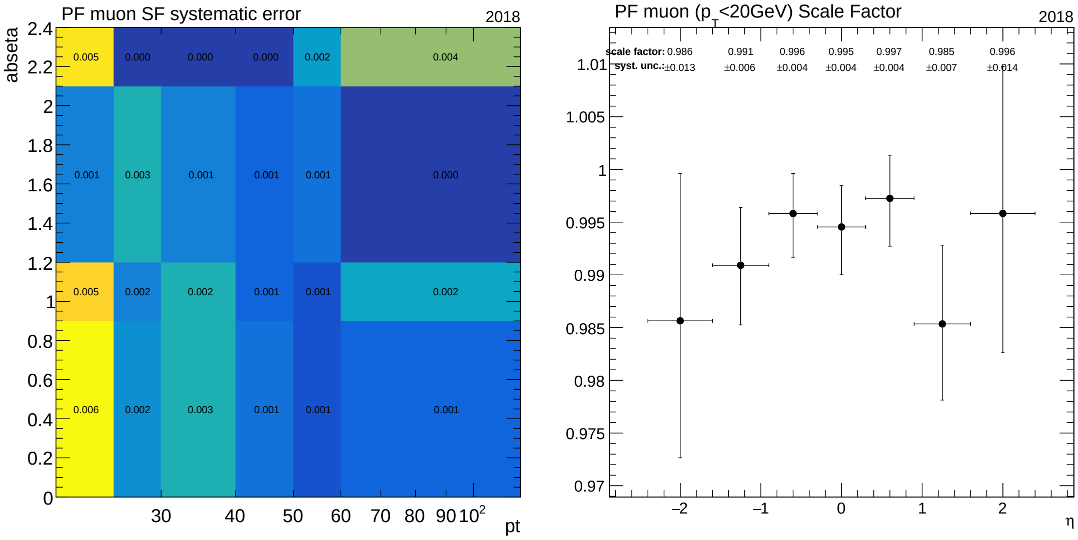

Figure 3.47: Systematic uncertainties for muon ID scale factor at the “loose” working point as measured by the MUON POG for 2018 (*left*, $p_\mathrm{T} > 15\,\mathrm{GeV}$; *right*, $p_\mathrm{T} < 20\,\mathrm{GeV}$. [23])

for PF electrons, photons and muons for channel $2\mu 2e$. Figure 3.49 displays the distribution of the percentage difference from the nominal for PF muons for channel 4μ. Table 3.26 lists the systematic uncertainties assigned for each object ID for the two search channels.

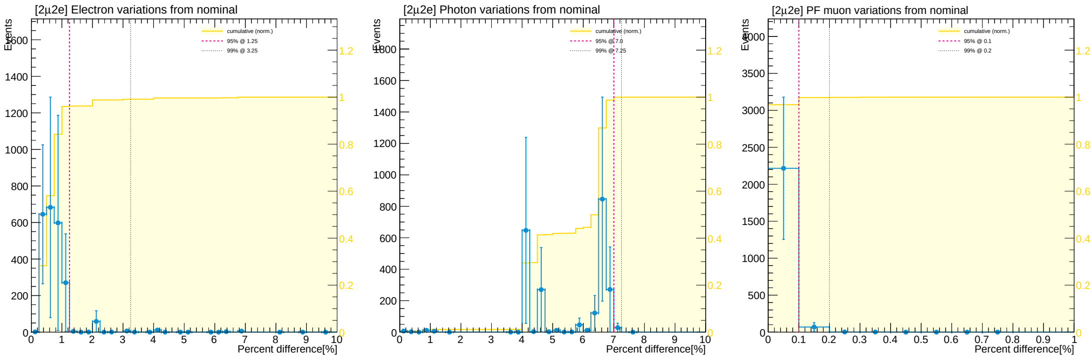

Figure 3.48: Maximum percentage difference of signal yields from nominal in the ABCD plane after applying ± lepton ID systematic uncertainties for PF electron (*left*), photon (*middle*) and muon (*right*) for channel $2\mu 2e$. The yellow filled distributions show the cumulative distributions. The pink (black) dashed vertical line marks the percentage difference at which the cumulative distribution arrives at 95% (99%).

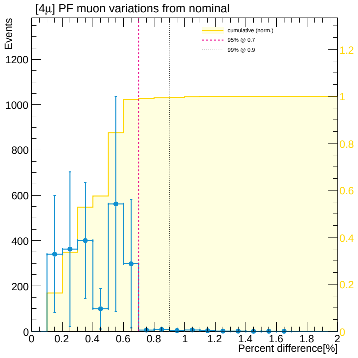

Figure 3.49: Maximum percentage difference of signal yields in ABCD plane from nominal after applying ± lepton ID systematic uncertainties for PF muon for channel 4μ. The yellow filled distributions show the cumulative distributions. The pink (black) dashed vertical line marks the percentage difference at which the cumulative distribution arrives at 95% (99%).

Channel	Object	Uncertainty
$2\mu 2e$	Electron	1.25%
	Photon	7.0%
	PF Muon	0.1%
4μ	PF Muon	0.7%

Table 3.26: Systematic uncertainties assigned due to lepton ID.

3.7.3 Closure of ABCD method for optimized boundaries

Due to the non-perfect independence between the two variables used to construct the ABCD plane, the closure of the ABCD method is evaluated and added as one source of systematic uncertainty. We obtain such uncertainty from the validation region in data. It is done by comparing the predicted yields in region D from region A, B, C against the observed yield. To reduce the influence of statistical fluctuations, the bin edges are varied locally around each boundary and the calculation is repeated. The average is then taken

Channel	Boundary ($\Delta\phi$, Iso)	Uncertainty
$2\mu 2e$	$(0.9\pi,\ 0.05)$	25.2%
	$(0.9\pi,\ 0.10)$	43.6%
4μ	$(0.9\pi,\ 0.20)$	19.2%
	$(0.9\pi,\ 0.25)$	27.2%
	$(0.9\pi,\ 0.30)$	15.6%

Table 3.27: Closure uncertainties.

as a measure of the uncertainty. Such procedure is performed for each optimized boundary from section 3.6.6, and the result is summarized in table 3.27.

3.8 Expected limits

The data is blinded in the signal region D for various boundaries, therefore the *expected* observation in region D, as in 3.6, is used to estimate the expected limits on the production cross section of the DM bound state. For the statistical treatment we use the Higgs combination tool, `combine`, with a new functionality [137] that was introduced to handle non linear relations between different regions, as needed for the ABCD method described above. In this approach the data card contains the observed number of events and the expectation (signal + background) for each of the four ABCD regions. A likelihood function is built that contains these ABCD regions and the explicit relation among them, which can be described by

$$L = \prod_{i}^{\text{ABCD}} \text{Poisson}(n_i|\text{bkg}_i + \mu \cdot \text{sig}_i) \times \prod_{j}^{\text{nuisances}} \text{Constraints}(\theta_j) \tag{3.13}$$

, where the 4 regions are included with Poisson pdfs and the term Constraints refers to either Gaussian or log normal pdfs that model the dependency on systematic uncertainties. In this analysis, the pdfs for all systematic uncertainties are assumed to follow a log-normal distribution. The expected limits are then calculated using the CLs criterion [138, 139], a modified frequentist approach, to place limits at the 95% confidence level. It is defined as

$$\mathrm{CL_s} = \frac{p_\mu}{1 - p_b} \tag{3.14}$$

. The p-value p_μ quantifies the compatibility of the data with the signal+background hypothesis, while p-value $1 - p_b$ quantifies the compatibility of the data with the background-only hypothesis. They are defined as

$$p_\mu = \int_{q_{\mathrm{obs}}}^{+\infty} P(q, \mu) \mathrm{d}q \tag{3.15}$$

$$1 - p_b = \int_{q_{\mathrm{obs}}}^{+\infty} P(q, 0) \mathrm{d}q \tag{3.16}$$

, where q is the test statistic, defined as

$$q = -2 \ln \frac{L_{\mu s+b}}{L_{\mu_0 s+b}} \tag{3.17}$$

, in which μ is the signal strength. For a certain confidence level $1 - \alpha$, signal models with values of $\mathrm{CL_s}$ such that $\mathrm{CL_s} \leqslant \alpha$ are excluded at a confidence level of $1 - \alpha$. The 95% confidence level upper limit on the signal strength μ is therefore the value of μ such that $\mathrm{CL_s} = 0.05$.

Figures 3.50–3.55 are plots of the expected upper limits on $\sigma(pp \to \chi\bar{\chi} \to Z_d Z_d)$ for various DM bound state mass $m_{\chi\bar{\chi}}$ and dark photon mass m_{Z_d} as a function of c times dark photon's mean proper lifetime, $c\tau$. They are obtained in an imagined ensemble of similar experiments having only background events. The spread of upper limits about the median in such an ensemble of background-only experiments is indicated by green bands containing the central 68% quantile, and by yellow bands containing the central 95%

quantile. Tables 3.28–3.33 summarize the median, ±1σ and ±2σ upper limits for various signal parameters ($m_{\chi\bar{\chi}}$, m_{Z_d}, $c\tau$).

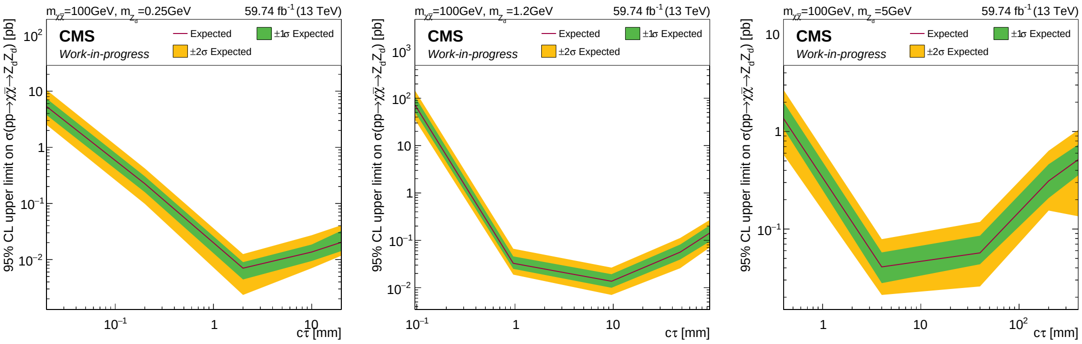

Figure 3.50: 95% CL upper limit on $\sigma(pp \to \chi\bar{\chi} \to Z_d Z_d)$ for $m_{\chi\bar{\chi}} = 100\,\text{GeV}$ for $m_{Z_d} = 0.25\,\text{GeV}$ (*left*), 1.2 GeV (*middle*), 5 GeV (*right*). The red line represents the median expected limits; the green shaded band shows the central 68% quantile; the yellow shaded band shows the central 95% quantile.

m_{Z_d} [GeV]	$c\tau$ [mm]	expected-2σ [pb]	expected-1σ [pb]	expected [pb]	expected+1σ [pb]	expected+2σ [pb]
0.25	0.02	2.52	3.77	5.34	7.39	1.05×10^{1}
	0.2	9.84×10^{-2}	1.59×10^{-1}	2.25×10^{-1}	3.05×10^{-1}	4.22×10^{-1}
	2	2.34×10^{-3}	4.42×10^{-3}	7.03×10^{-3}	9.00×10^{-3}	1.25×10^{-2}
	10	7.03×10^{-3}	9.43×10^{-3}	1.36×10^{-2}	1.85×10^{-2}	2.72×10^{-2}
	20	1.17×10^{-2}	1.42×10^{-2}	2.03×10^{-2}	3.27×10^{-2}	4.09×10^{-2}
1.2	0.096	3.52×10^{1}	5.09×10^{1}	7.20×10^{1}	1.08×10^{2}	1.45×10^{2}
	0.96	1.89×10^{-2}	2.50×10^{-2}	3.27×10^{-2}	4.58×10^{-2}	6.64×10^{-2}
	9.6	7.03×10^{-3}	9.97×10^{-3}	1.37×10^{-2}	1.93×10^{-2}	2.66×10^{-2}
	48	2.58×10^{-2}	3.94×10^{-2}	5.64×10^{-2}	8.16×10^{-2}	1.12×10^{-1}
	96	7.08×10^{-2}	9.48×10^{-2}	1.43×10^{-1}	2.07×10^{-1}	2.70×10^{-1}
5	0.4	5.81×10^{-1}	1.07	1.36	2.02	2.68
	4	2.11×10^{-2}	2.79×10^{-2}	4.09×10^{-2}	5.76×10^{-2}	7.88×10^{-2}
	40	2.58×10^{-2}	4.36×10^{-2}	5.69×10^{-2}	8.55×10^{-2}	1.18×10^{-1}
	200	1.55×10^{-1}	2.08×10^{-1}	3.11×10^{-1}	4.62×10^{-1}	6.36×10^{-1}
	400	1.35×10^{-1}	3.56×10^{-1}	5.16×10^{-1}	7.36×10^{-1}	1.04

Table 3.28: 95% CL expected upper limits on $\sigma(pp \to \chi\bar{\chi} \to Z_d Z_d)$ for signal samples with DM bound state mass $m_{\chi\bar{\chi}} = 100\,\text{GeV}$.

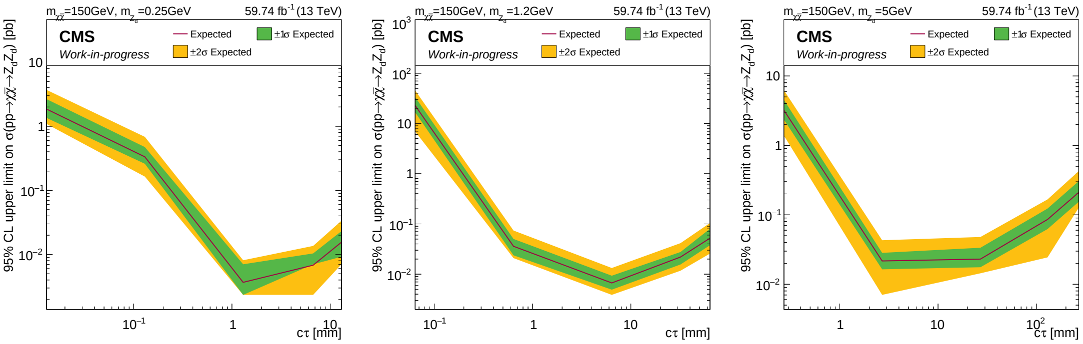

Figure 3.51: 95% CL upper limit on $\sigma(pp \to \chi\bar{\chi} \to Z_d Z_d)$ for $m_{\chi\bar{\chi}} = 150\,\text{GeV}$ for $m_{Z_d} = 0.25\,\text{GeV}$ (*left*), $1.2\,\text{GeV}$ (*middle*), $5\,\text{GeV}$ (*right*). The red line represents the median expected limits; the green shaded band shows the central 68% quantile; the yellow shaded band shows the central 95% quantile.

m_{Z_d} [GeV]	$c\tau$ [mm]	expected-2σ [pb]	expected-1σ [pb]	expected [pb]	expected+1σ [pb]	expected+2σ [pb]
0.25	0.013	1.09	1.35	1.86	2.65	3.70
	0.13	1.64×10^{-1}	2.60×10^{-1}	3.34×10^{-1}	4.74×10^{-1}	6.84×10^{-1}
	1.3	2.34×10^{-3}	2.34×10^{-3}	3.68×10^{-3}	7.03×10^{-3}	8.13×10^{-3}
	6.7	2.34×10^{-3}	7.03×10^{-3}	6.81×10^{-3}	1.04×10^{-2}	1.36×10^{-2}
	13	7.03×10^{-3}	9.21×10^{-3}	1.55×10^{-2}	2.31×10^{-2}	3.36×10^{-2}
1.2	0.064	6.90	1.66×10^{1}	2.27×10^{1}	3.35×10^{1}	4.53×10^{1}
	0.64	2.09×10^{-2}	2.38×10^{-2}	3.59×10^{-2}	5.03×10^{-2}	7.40×10^{-2}
	6.4	3.87×10^{-3}	4.92×10^{-3}	6.69×10^{-3}	9.32×10^{-3}	1.33×10^{-2}
	32	1.17×10^{-2}	1.56×10^{-2}	2.19×10^{-2}	2.76×10^{-2}	4.15×10^{-2}
	64	2.58×10^{-2}	3.78×10^{-2}	5.23×10^{-2}	8.04×10^{-2}	1.05×10^{-1}
5	0.27	1.39	2.36	3.22	4.54	6.25
	2.7	7.03×10^{-3}	1.64×10^{-2}	2.17×10^{-2}	2.83×10^{-2}	4.30×10^{-2}
	27	1.44×10^{-2}	1.76×10^{-2}	2.30×10^{-2}	3.36×10^{-2}	4.79×10^{-2}
	130	2.44×10^{-2}	6.24×10^{-2}	8.58×10^{-2}	1.23×10^{-1}	1.67×10^{-1}
	270	1.27×10^{-1}	1.54×10^{-1}	2.10×10^{-1}	3.05×10^{-1}	4.26×10^{-1}

Table 3.29: 95% CL expected upper limits on $\sigma(pp \to \chi\bar{\chi} \to Z_d Z_d)$ for signal samples with DM bound state mass $m_{\chi\bar{\chi}} = 150\,\text{GeV}$.

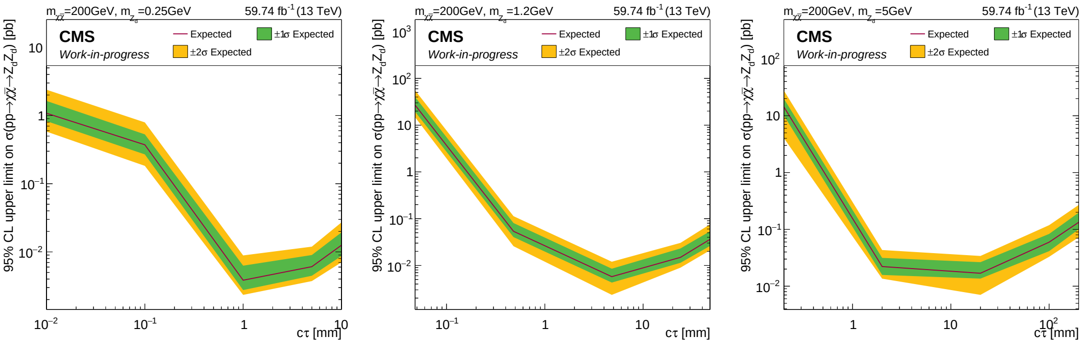

Figure 3.52: 95% CL upper limit on $\sigma(pp \to \chi\bar{\chi} \to Z_dZ_d)$ for $m_{\chi\bar{\chi}} = 200\,\text{GeV}$ for $m_{Z_d} = 0.25\,\text{GeV}$ (*left*), 1.2 GeV (*middle*), 5 GeV (*right*). The red line represents the median expected limits; the green shaded band shows the central 68% quantile; the yellow shaded band shows the central 95% quantile.

m_{Z_d} [GeV]	$c\tau$ [mm]	expected-2σ [pb]	expected-1σ [pb]	expected [pb]	expected+1σ [pb]	expected+2σ [pb]
0.25	0.01	5.81×10^{-1}	8.28×10^{-1}	1.08	1.64	2.39
	0.1	1.83×10^{-1}	2.69×10^{-1}	3.72×10^{-1}	5.29×10^{-1}	7.93×10^{-1}
	1	2.34×10^{-3}	2.76×10^{-3}	3.84×10^{-3}	6.28×10^{-3}	8.88×10^{-3}
	5	3.73×10^{-3}	4.47×10^{-3}	6.08×10^{-3}	9.00×10^{-3}	1.19×10^{-2}
	10	7.03×10^{-3}	8.73×10^{-3}	1.25×10^{-2}	1.93×10^{-2}	2.71×10^{-2}
1.2	0.048	1.47×10^{1}	1.92×10^{1}	2.67×10^{1}	3.98×10^{1}	5.51×10^{1}
	0.48	2.58×10^{-2}	4.04×10^{-2}	5.37×10^{-2}	8.07×10^{-2}	1.13×10^{-1}
	4.8	2.34×10^{-3}	4.29×10^{-3}	5.75×10^{-3}	8.50×10^{-3}	1.20×10^{-2}
	24	8.96×10^{-3}	1.14×10^{-2}	1.49×10^{-2}	2.31×10^{-2}	3.03×10^{-2}
	48	2.11×10^{-2}	2.61×10^{-2}	3.62×10^{-2}	5.37×10^{-2}	7.58×10^{-2}
5	0.2	4.05	1.01×10^{1}	1.43×10^{1}	2.00×10^{1}	2.78×10^{1}
	2	1.36×10^{-2}	1.58×10^{-2}	2.22×10^{-2}	3.15×10^{-2}	4.33×10^{-2}
	20	7.03×10^{-3}	1.36×10^{-2}	1.69×10^{-2}	2.65×10^{-2}	3.40×10^{-2}
	100	3.29×10^{-2}	4.14×10^{-2}	5.96×10^{-2}	8.32×10^{-2}	1.19×10^{-1}
	200	7.27×10^{-2}	1.00×10^{-1}	1.33×10^{-1}	1.97×10^{-1}	2.69×10^{-1}

Table 3.30: 95% CL expected upper limits on $\sigma(pp \to \chi\bar{\chi} \to Z_dZ_d)$ for signal samples with DM bound state mass $m_{\chi\bar{\chi}} = 200\,\text{GeV}$.

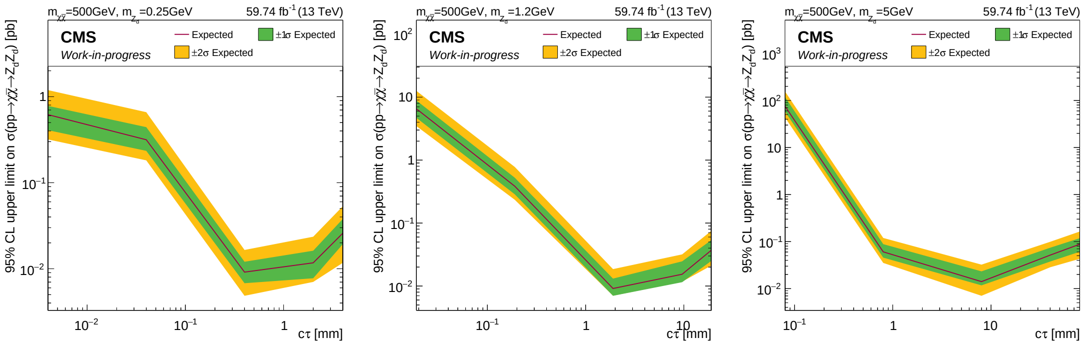

Figure 3.53: 95% CL upper limit on $\sigma(pp \to \chi\bar{\chi} \to Z_d Z_d)$ for $m_{\chi\bar{\chi}} = 500\,\text{GeV}$ for $m_{Z_d} = 0.25\,\text{GeV}$ (*left*), $1.2\,\text{GeV}$ (*middle*), $5\,\text{GeV}$ (*right*). The red line represents the median expected limits; the green shaded band shows the central 68% quantile; the yellow shaded band shows the central 95% quantile.

m_{Z_d} [GeV]	$c\tau$ [mm]	expected-2σ [pb]	expected-1σ [pb]	expected [pb]	expected+1σ [pb]	expected+2σ [pb]
0.25	0.004	3.19×10^{-1}	4.08×10^{-1}	6.18×10^{-1}	7.82×10^{-1}	1.19
	0.04	1.82×10^{-1}	2.35×10^{-1}	3.16×10^{-1}	4.43×10^{-1}	6.61×10^{-1}
	0.4	4.85×10^{-3}	6.79×10^{-3}	9.14×10^{-3}	1.21×10^{-2}	1.65×10^{-2}
	2	7.03×10^{-3}	7.75×10^{-3}	1.17×10^{-2}	1.62×10^{-2}	2.36×10^{-2}
	4	1.17×10^{-2}	1.93×10^{-2}	2.59×10^{-2}	3.79×10^{-2}	5.32×10^{-2}
1.2	0.019	3.46	4.68	6.51	8.82	1.25×10^{1}
	0.19	2.34×10^{-1}	2.86×10^{-1}	3.85×10^{-1}	5.25×10^{-1}	7.78×10^{-1}
	1.9	7.03×10^{-3}	6.99×10^{-3}	9.13×10^{-3}	1.31×10^{-2}	1.86×10^{-2}
	9.6	1.17×10^{-2}	1.15×10^{-2}	1.54×10^{-2}	2.47×10^{-2}	3.18×10^{-2}
	19	2.11×10^{-2}	2.50×10^{-2}	3.70×10^{-2}	5.35×10^{-2}	7.51×10^{-2}
5	0.08	4.36×10^{1}	5.83×10^{1}	7.57×10^{1}	1.19×10^{2}	1.56×10^{2}
	0.8	3.52×10^{-2}	4.56×10^{-2}	6.05×10^{-2}	8.81×10^{-2}	1.19×10^{-1}
	8	7.03×10^{-3}	1.17×10^{-2}	1.41×10^{-2}	2.33×10^{-2}	3.23×10^{-2}
	40	2.84×10^{-2}	3.76×10^{-2}	5.15×10^{-2}	7.40×10^{-2}	9.89×10^{-2}
	80	4.30×10^{-2}	6.08×10^{-2}	8.78×10^{-2}	1.18×10^{-1}	1.63×10^{-1}

Table 3.31: 95% CL expected upper limits on $\sigma(pp \to \chi\bar{\chi} \to Z_d Z_d)$ for signal samples with DM bound state mass $m_{\chi\bar{\chi}} = 500\,\text{GeV}$.

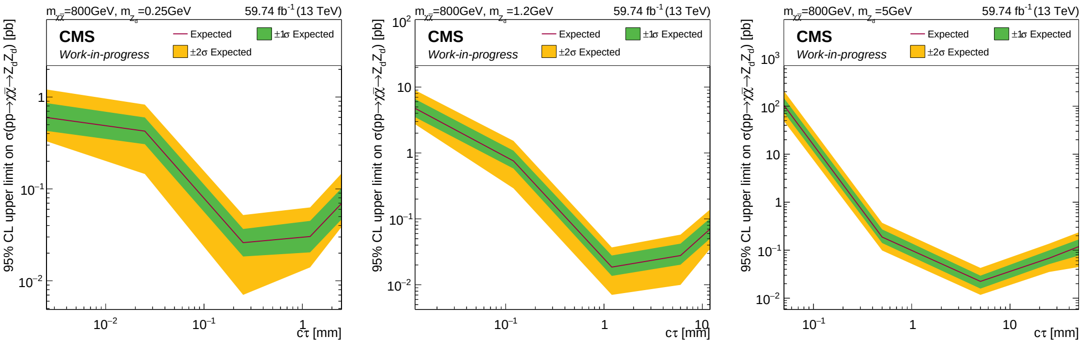

Figure 3.54: 95% CL upper limit on $\sigma(pp \to \chi\bar{\chi} \to Z_d Z_d)$ for $m_{\chi\bar{\chi}} = 800\,\mathrm{GeV}$ for $m_{Z_d} = 0.25\,\mathrm{GeV}$ (*left*), $1.2\,\mathrm{GeV}$ (*middle*), $5\,\mathrm{GeV}$ (*right*). The red line represents the median expected limits; the green shaded band shows the central 68% quantile; the yellow shaded band shows the central 95% quantile.

m_{Z_d} [GeV]	$c\tau$ [mm]	expected-2σ [pb]	expected-1σ [pb]	expected [pb]	expected+1σ [pb]	expected+2σ [pb]
0.25	0.0025	3.30×10^{-1}	4.28×10^{-1}	5.99×10^{-1}	8.59×10^{-1}	1.21
	0.025	1.45×10^{-1}	3.07×10^{-1}	4.26×10^{-1}	5.99×10^{-1}	8.27×10^{-1}
	0.25	7.03×10^{-3}	1.84×10^{-2}	2.60×10^{-2}	3.67×10^{-2}	5.20×10^{-2}
	1.2	1.40×10^{-2}	2.04×10^{-2}	3.04×10^{-2}	4.49×10^{-2}	6.29×10^{-2}
	2.5	3.85×10^{-2}	4.65×10^{-2}	6.92×10^{-2}	1.01×10^{-1}	1.47×10^{-1}
1.2	0.012	2.72	3.49	4.75	6.56	8.96
	0.12	2.91×10^{-1}	5.80×10^{-1}	7.57×10^{-1}	1.08	1.53
	1.2	7.03×10^{-3}	1.36×10^{-2}	1.86×10^{-2}	2.78×10^{-2}	3.69×10^{-2}
	6	9.97×10^{-3}	2.02×10^{-2}	2.78×10^{-2}	4.21×10^{-2}	5.77×10^{-2}
	12	3.52×10^{-2}	5.03×10^{-2}	7.01×10^{-2}	1.02×10^{-1}	1.39×10^{-1}
5	0.05	4.92×10^{1}	7.47×10^{1}	1.05×10^{2}	1.48×10^{2}	2.08×10^{2}
	0.5	9.84×10^{-2}	1.41×10^{-1}	1.87×10^{-1}	2.71×10^{-1}	3.71×10^{-1}
	5	1.17×10^{-2}	1.58×10^{-2}	2.24×10^{-2}	2.94×10^{-2}	4.27×10^{-2}
	25	3.52×10^{-2}	5.12×10^{-2}	6.81×10^{-2}	9.91×10^{-2}	1.37×10^{-1}
	50	4.45×10^{-2}	7.73×10^{-2}	1.19×10^{-1}	1.67×10^{-1}	2.36×10^{-1}

Table 3.32: 95% CL expected upper limits on $\sigma(pp \to \chi\bar{\chi} \to Z_d Z_d)$ for signal samples with DM bound state mass $m_{\chi\bar{\chi}} = 800\,\mathrm{GeV}$.

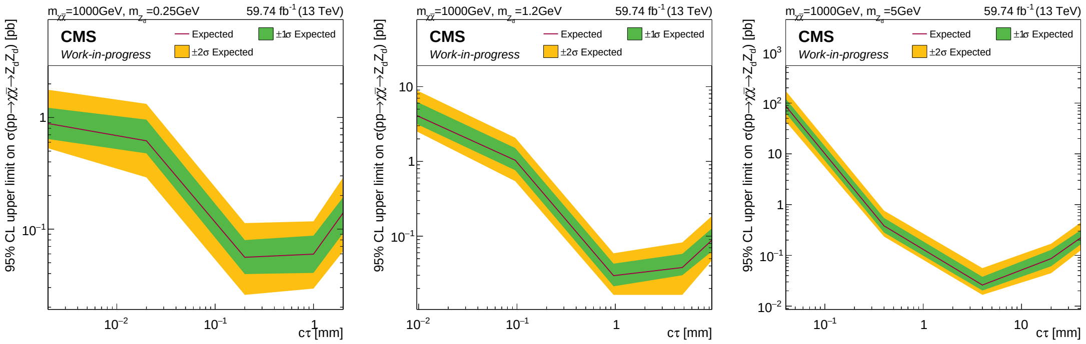

Figure 3.55: 95% CL upper limit on $\sigma(pp \to \chi\bar{\chi} \to Z_dZ_d)$ for $m_{\chi\bar{\chi}} = 1000\,\text{GeV}$ for $m_{Z_d} = 0.25\,\text{GeV}$ (*left*), $1.2\,\text{GeV}$ (*middle*), $5\,\text{GeV}$ (*right*). The red line represents the median expected limits; the green shaded band shows the central 68% quantile; the yellow shaded band shows the central 95% quantile.

m_{Z_d} [GeV]	$c\tau$ [mm]	expected-2σ [pb]	expected-1σ [pb]	expected [pb]	expected+1σ [pb]	expected+2σ [pb]
0.25	0.002	5.30×10^{-1}	6.41×10^{-1}	8.83×10^{-1}	1.22	1.77
	0.02	2.91×10^{-1}	4.77×10^{-1}	6.18×10^{-1}	9.57×10^{-1}	1.32
	0.2	2.58×10^{-2}	3.96×10^{-2}	5.60×10^{-2}	7.98×10^{-2}	1.13×10^{-1}
	1	2.94×10^{-2}	4.06×10^{-2}	5.97×10^{-2}	8.75×10^{-2}	1.18×10^{-1}
	2	6.33×10^{-2}	9.21×10^{-2}	1.40×10^{-1}	1.93×10^{-1}	2.90×10^{-1}
1.2	0.0096	2.51	3.16	4.10	6.26	8.92
	0.096	5.44×10^{-1}	7.62×10^{-1}	1.04	1.51	2.07
	0.96	1.64×10^{-2}	2.13×10^{-2}	2.96×10^{-2}	4.29×10^{-2}	5.90×10^{-2}
	4.8	1.64×10^{-2}	3.00×10^{-2}	3.81×10^{-2}	5.80×10^{-2}	8.25×10^{-2}
	9.6	4.76×10^{-2}	6.27×10^{-2}	8.84×10^{-2}	1.27×10^{-1}	1.86×10^{-1}
5	0.04	4.36×10^{1}	6.37×10^{1}	8.75×10^{1}	1.22×10^{2}	1.74×10^{2}
	0.4	2.34×10^{-1}	2.81×10^{-1}	3.81×10^{-1}	5.44×10^{-1}	7.60×10^{-1}
	4	1.67×10^{-2}	2.03×10^{-2}	2.60×10^{-2}	3.78×10^{-2}	5.61×10^{-2}
	20	4.45×10^{-2}	6.09×10^{-2}	8.63×10^{-2}	1.28×10^{-1}	1.70×10^{-1}
	40	1.25×10^{-1}	1.65×10^{-1}	2.22×10^{-1}	3.13×10^{-1}	4.44×10^{-1}

Table 3.33: 95% CL expected upper limits on $\sigma(pp \to \chi\bar{\chi} \to Z_dZ_d)$ for signal samples with DM bound state mass $m_{\chi\bar{\chi}} = 1000\,\text{GeV}$.

Chapter 4

Summary and Remarks

This thesis presents an on-going search for self-interacting dark matter bound state decaying to two dark force carrier – dark photons, which further decays into two pairs of leptons (one dark photon decays to muon pair for triggering, the other one decays to either electron or muon pair). This search makes use of pp collision data collected by the CMS detector in 2018 at $\sqrt{s} = 13\,\mathrm{TeV}$ corresponding to 59.74 fb^{-1} of total integrated luminosity during Run2 of LHC. As a first-round analysis, the search strategy was conceived to be general in terms of wide DM bound state mass range and focused more on displaced signals. Multiple experimental signatures, including collimated leptons, photons and displaced muons, are considered in a combined reconstructed object – lepton-jets. The signal requires the presence of two lepton-jets with large azimuthal angle in the beam transverse plane. The results are reported in terms of 95% CL upper limits on the DM bound state production cross section $\sigma(pp \to \chi\bar{\chi} \to Z_d Z_d)$, assuming $\mathrm{Br}(\chi\bar{\chi} \to Z_d Z_d)$ is 100%. Only the expected limits are reported, while the observed limits will follow once this analysis is approved inside the collaboration.

On top of this first-round analysis, several potential improvements have already been seen, and a few areas could be further investigated to increase sensitivities. This analysis is only making use of 2018 data due to choices of the displaced double muon triggers. Triggering on $Z_d \to e^+e^-$ is possible (e.g. single photon trigger) but the efficiency varies depending on the kinematics, especially on the p_{T} of the dark photon. For Run3 of LHC, additional triggers targeting for long-lived signatures are foreseen to be designed and put online, which will enhance the signal triggering efficiencies. Triggers which target multiple muons in a small cone or jets with high $E_{\mathrm{HCAL}/E_{\mathrm{ECAL}}}$ ratio would definitely help with the efficiencies for events with dark photons decayed inside HCAL region. On the object level, more detailed studies could be carried out separately depending on where the long-lived dark photon decays, since the experimental signature would be different and could be better exploited. On the background estimation, the total amount of the background events would be different for low DM bound state mass signal and high DM bound state mass signal if the invariant mass of the lepton-jet pair is used. This analysis is more focused on the displaced signal by using a displacement cut on the muons. The prompt signal region is also possible to cover, especially in the high mass region.

The long-lived dark photon is an interesting scenario which could bridge the visible SM sector and the invisible dark sector. The exploration of such long-lived experimental signature is getting more attractions and rapid developments recently. Self-interacting dark matter could be one underlying theory for dark matter, and its search at high energy collider would help with the further development of the theory. This thesis provides a contribution on exploring such two interesting topics, hoping to open a gate for a new territory awaiting more studies to be injected.

Bibliography

[1] E. Corbelli and P. Salucci, “The extended rotation curve and the dark matter halo of M33”, *Monthly Notices of the Royal Astronomical Society* **311** (2000), no. 2, 441–447.

[2] F. Lenzen, S. Schindler, and O. Scherzer, “Automatic detection of arcs and arclets formed by gravitational lensing”, *Astronomy & Astrophysics* **416** (2004), no. 1, 391–401.

[3] M. Tegmark et al., “The three-dimensional power spectrum of galaxies from the sloan digital sky survey”, *The Astrophysical Journal* **606** (2004), no. 2, 702.

[4] S.-H. Oh et al., “High-resolution mass models of dwarf galaxies from LITTLE THINGS”, *The Astronomical Journal* **149** (2015), no. 6, 180.

[5] M. Kaplinghat, S. Tulin, and H.-B. Yu, “Dark matter halos as particle colliders: unified solution to small-scale structure puzzles from dwarfs to clusters”, *Physical Review Letters* **116** (2016), no. 4, 041302.

[6] A. Kamada, M. Kaplinghat, A. B. Pace, and H.-B. Yu, “Self-interacting dark matter can explain diverse galactic rotation curves”, *Physical review letters* **119** (2017), no. 11, 111102.

[7] S. Tulin and H.-B. Yu, “Dark Matter Self-interactions and Small Scale Structure”, *Phys. Rept.* **730** (2018) 1–57, `doi:10.1016/j.physrep.2017.11.004`, `arXiv:1705.02358`.

[8] K. A. Oman et al., “The unexpected diversity of dwarf galaxy rotation curves”, *Monthly Notices of the Royal Astronomical Society* **452** (2015), no. 4, 3650–3665.

[9] M. Boylan-Kolchin, J. S. Bullock, and M. Kaplinghat, “The Milky Way’s bright satellites as an apparent failure of λCDM”, *Monthly Notices of the Royal Astronomical Society* **422** (2012), no. 2, 1203–1218.

[10] M. Rocha et al., “Cosmological simulations with self-interacting dark matter–I. Constant-density cores and substructure”, *Monthly Notices of the Royal Astronomical Society* **430** (2013), no. 1, 81–104.

[11] A. H. Peter, M. Rocha, J. S. Bullock, and M. Kaplinghat, "Cosmological simulations with self-interacting dark matter–II. Halo shapes versus observations", *Monthly Notices of the Royal Astronomical Society* **430** (2013), no. 1, 105–120.

[12] Y. Tsai, T. Xu, and H.-B. Yu, "Displaced lepton jet signatures from self-interacting dark matter bound states", *Journal of High Energy Physics* **2019** (2019), no. 8, 131.

[13] E. Mobs, "The CERN accelerator complex - 2019. Complexe des accélérateurs du CERN - 2019", Jul, 2019. General Photo. `http://cds.cern.ch/record/2684277`.

[14] CERN, "Diagram of an LHC dipole magnet. Schéma d'un aimant dipôle du LHC", Jun, 1999. `https://cds.cern.ch/record/40524`.

[15] J.-L. Caron, "Computed magnetic flux in the LHC dipole. Champ magnetique (calcule) dans le dipole LHC.", Mar, 1998. `http://cds.cern.ch/record/841503`.

[16] CMS Collaboration, "TWiki: CMS Luminosity - Public Results". `https://twiki.cern.ch/twiki/bin/view/CMSPublic/LumiPublicResults`.

[17] CMS Collaboration, "CMS detector design". `http://cms.web.cern.ch/news/cms-detector-design`.

[18] CMS Collaboration, "Particle-flow reconstruction and global event description with the CMS detector", *JINST* **12** (2017), no. 10, P10003, `doi:10.1088/1748-0221/12/10/P10003`, `arXiv:1706.04965`.

[19] CMS Collaboration, "Alignment of the CMS muon system with cosmic-ray and beam-halo muons", *Journal of Instrumentation* **5** (2010), no. 03, T03020.

[20] CMS Collaboration, "The Phase-2 Upgrade of the CMS Tracker",.

[21] CMS Collaboration, "The CMS Level-1 electron and photon trigger: for Run II of LHC", *Journal of Instrumentation* **12** (2017), no. 02, C02014.

[22] P. Ilten, Y. Soreq, M. Williams, and W. Xue, "Serendipity in dark photon searches", *JHEP* **06** (2018) 004, `doi:10.1007/JHEP06(2018)004`, `arXiv:1801.04847`.

[23] CMS Collaboration, "Developments on Muon efficiency measurements with 2016, 2017 and 2018 data for HZZ4l analysis". `https://indico.cern.ch/event/902727/contributions/3800052/attachments/2015863/3448934/v4_Status_report_muon_TnP2018_tahir_POG_Meeting_06.04.2020.pdf`.

[24] O. S. Brning et al., "LHC Design Report". CERN Yellow Reports: Monographs. CERN, Geneva, 2004. `doi:10.5170/CERN-2004-003-V-1`.

[25] CMS Collaboration, "PdmVAnalysisSummaryTable < CMS < TWiki". `https://twiki.cern.ch/twiki/bin/viewauth/CMS/PdmVAnalysisSummaryTable`.

[26] CMS Collaboration, “Particle-flow reconstruction and global event description with the CMS detector”, *JINST* **12** (2017), no. 10, P10003, `doi:10.1088/1748-0221/12/10/P10003`, `arXiv:1706.04965`.

[27] ATLAS Collaboration, “Observation of a new particle in the search for the Standard Model Higgs boson with the ATLAS detector at the LHC”, *Physics Letters B* **716** (Sep, 2012) 1–29, `doi:10.1016/j.physletb.2012.08.020`.

[28] CMS Collaboration, “Observation of a new boson at a mass of 125 GeV with the CMS experiment at the LHC”, *Physics Letters B* **716** (Sep, 2012) 30–61, `doi:10.1016/j.physletb.2012.08.021`.

[29] F. Englert and R. Brout, “Broken Symmetry and the Mass of Gauge Vector Mesons”, *Phys. Rev. Lett.* **13** (Aug, 1964) 321–323, `doi:10.1103/PhysRevLett.13.321`.

[30] G. S. Guralnik, C. R. Hagen, and T. W. B. Kibble, “Global Conservation Laws and Massless Particles”, *Phys. Rev. Lett.* **13** (Nov, 1964) 585–587, `doi:10.1103/PhysRevLett.13.585`.

[31] T. W. B. Kibble, “Symmetry Breaking in Non-Abelian Gauge Theories”, *Phys. Rev.* **155** (Mar, 1967) 1554–1561, `doi:10.1103/PhysRev.155.1554`.

[32] M. S. Roberts and R. N. Whitehurst, “The rotation curve and geometry of M31 at large galactocentric distances.”, *The Astrophysical Journal* **201** (1975) 327–346.

[33] M. Roberts and A. Rots, “Comparison of rotation curves of different galaxy types”, *Astronomy and Astrophysics* **26** (1973) 483–485.

[34] V. C. Rubin and W. K. Ford Jr, “Rotation of the Andromeda nebula from a spectroscopic survey of emission regions”, *The Astrophysical Journal* **159** (1970) 379.

[35] A. Bosma, “21-cm line studies of spiral galaxies. II. The distribution and kinematics of neutral hydrogen in spiral galaxies of various morphological types.”, *The Astronomical Journal* **86** (1981) 1825–1846.

[36] V. C. Rubin, W. K. Ford Jr, and N. Thonnard, “Rotational properties of 21 SC galaxies with a large range of luminosities and radii, from NGC 4605/R= 4kpc/to UGC 2885/R= 122 kpc”, *The Astrophysical Journal* **238** (1980) 471–487.

[37] C. Carignan and K. Freeman, “Basic parameters of dark halos in late-type spirals”, *The Astrophysical Journal* **294** (1985) 494–501.

[38] Y. Sofue and V. Rubin, “Rotation curves of spiral galaxies”, *Annual Review of Astronomy and Astrophysics* **39** (2001), no. 1, 137–174.

[39] J. Ostriker, P. Peebles, and A. Yahil, “The size and mass of galaxies and the mass of the universe”, 1974.

[40] J. Einasto, A. Kaasik, and E. Saar, “Dynamic evidence on massive coronas of galaxies”, *Nature* **250** (1974), no. 5464, 309–310.

[41] S. Gershtein and Y. B. Zeldovich, “Rest mass of muonic neutrino and cosmology”, *Jetp Lett* **4** (1966), no. 120-122, 1.

[42] R. Cowsik and J. McClelland, “An upper limit on the neutrino rest mass”, *Physical Review Letters* **29** (1972), no. 10, 669.

[43] A. Szalay and G. Marx, “Neutrino rest mass from cosmology”, *Astronomy and Astrophysics* **49** (1976) 437–441.

[44] S. D. White, C. Frenk, and M. Davis, “Clustering in a neutrino-dominated universe”, *The Astrophysical Journal* **274** (1983) L1–L5.

[45] S. D. White, M. Davis, and C. S. Frenk, “The size of clusters in a neutrino-dominated universe”, *Monthly Notices of the Royal Astronomical Society* **209** (1984), no. 1, 27P–31P.

[46] P. Hut and S. D. White, “Can a neutrino-dominated universe be rejected?”, *Nature* **310** (1984), no. 5979, 637–640.

[47] H. Goldberg, “Constraint on the photino mass from cosmology”, *Physical Review Letters* **50** (1983), no. 19, 1419.

[48] G. Jungman, M. Kamionkowski, and K. Griest, “Supersymmetric dark matter”, *Physics Reports* **267** (1996), no. 5-6, 195–373.

[49] G. Servant and T. M. Tait, “Is the lightest Kaluza-Klein particle a viable dark matter candidate?”, *Nuclear Physics B* **650** (2003), no. 1-2, 391–419.

[50] H.-C. Cheng, J. L. Feng, and K. T. Matchev, “Kaluza-klein dark matter”, *Physical review letters* **89** (2002), no. 21, 211301.

[51] J. Preskill, M. B. Wise, and F. Wilczek, “Cosmology of the invisible axion”, *Physics Letters B* **120** (1983), no. 1-3, 127–132.

[52] R. D. Peccei and H. R. Quinn, “Cp Conservation in the Presence of Instantons”, *Phys. Rev. Lett.* **38** (1977), no. ITP-568-STANFORD, 1440–1443.

[53] BICEP2, Keck Array Collaboration, “Bicep2 / Keck Array x: Constraints on Primordial Gravitational Waves using Planck, WMAP, and New BICEP2/Keck Observations through the 2015 Season”, *Phys. Rev. Lett.* **121** (2018) 221301, `doi:10.1103/PhysRevLett.121.221301`, `arXiv:1810.05216`.

[54] V. Springel, C. S. Frenk, and S. D. White, “The large-scale structure of the Universe”, *Nature* **440** (2006), no. 7088, 1137–1144.

[55] S. Trujillo-Gomez, A. Klypin, J. Primack, and A. J. Romanowsky, “Galaxies in λCDM with halo abundance matching: Luminosity-velocity relation, baryonic mass-velocity relation, velocity function, and clustering”, *The Astrophysical Journal* **742** (2011), no. 1, 16.

[56] E. Komatsu et al., “Seven-year wilkinson microwave anisotropy probe (WMAP*) observations: cosmological interpretation”, *The Astrophysical Journal Supplement Series* **192** (2011), no. 2, 18.

[57] K. Freese, M. Lisanti, and C. Savage, “Colloquium: Annual modulation of dark matter”, *Reviews of Modern Physics* **85** (2013), no. 4, 1561.

[58] J. Dubinski and R. Carlberg, “The structure of cold dark matter halos”, *The Astrophysical Journal* **378** (1991) 496–503.

[59] J. F. Navarro, “The structure of cold dark matter halos”, in *Symposium-international astronomical union*, volume 171, pp. 255–258, Cambridge University Press. 1996.

[60] J. F. Navarro, C. S. Frenk, and S. D. White, “A universal density profile from hierarchical clustering”, *The Astrophysical Journal* **490** (1997), no. 2, 493.

[61] B. Moore et al., “Cold collapse and the core catastrophe”, *Monthly Notices of the Royal Astronomical Society* **310** (1999), no. 4, 1147–1152.

[62] R. A. Flores and J. R. Primack, “Observational and theoretical constraints on singular dark matter halos”, *arXiv preprint astro-ph/9402004* (1994).

[63] G. Kauffmann, S. D. White, and B. Guiderdoni, “The formation and evolution of galaxies within merging dark matter haloes”, *Monthly Notices of the Royal Astronomical Society* **264** (1993), no. 1, 201–218.

[64] B. Moore et al., “Dark matter substructure within galactic halos”, *The Astrophysical Journal Letters* **524** (1999), no. 1, L19.

[65] A. Klypin, A. V. Kravtsov, O. Valenzuela, and F. Prada, “Where are the missing galactic satellites?”, *The Astrophysical Journal* **522** (1999), no. 1, 82.

[66] J. Zavala et al., “The velocity function in the local environment from λCDM and λWDM constrained simulations”, *The Astrophysical Journal* **700** (2009), no. 2, 1779.

[67] M. A. Zwaan, M. J. Meyer, and L. Staveley-Smith, “The velocity function of gas-rich galaxies”, *Monthly Notices of the Royal Astronomical Society* **403** (2010), no. 4, 1969–1977.

[68] M. Boylan-Kolchin, J. S. Bullock, and M. Kaplinghat, “Too big to fail? the puzzling darkness of massive Milky Way subhaloes”, *Monthly Notices of the Royal Astronomical Society: Letters* **415** (2011), no. 1, L40–L44.

[69] M. Vogelsberger, J. Zavala, and A. Loeb, “Subhaloes in self-interacting galactic dark matter haloes”, *Monthly Notices of the Royal Astronomical Society* **423** (2012), no. 4, 3740–3752.

[70] J. Zavala, M. Vogelsberger, and M. G. Walker, “Constraining self-interacting dark matter with the milky way’s dwarf spheroidals”, *Monthly Notices of the Royal Astronomical Society: Letters* **431** (2013), no. 1, L20–L24.

[71] O. D. Elbert et al., “Core formation in dwarf haloes with self-interacting dark matter: no fine-tuning necessary”, *Monthly Notices of the Royal Astronomical Society* **453** (2015), no. 1, 29–37.

[72] A. Schneider et al., “Hints against the cold and collisionless nature of dark matter from the galaxy velocity function”, *Monthly Notices of the Royal Astronomical Society* **470** (2017), no. 2, 1542–1558.

[73] J. F. Navarro, V. R. Eke, and C. S. Frenk, “The cores of dwarf galaxy haloes”, *Monthly Notices of the Royal Astronomical Society* **283** (1996), no. 3, L72–L78.

[74] F. Governato et al., “Bulgeless dwarf galaxies and dark matter cores from supernova-driven outflows”, *Nature* **463** (2010), no. 7278, 203–206.

[75] S. Colombi, S. Dodelson, and L. M. Widrow, “Large scale structure tests of warm dark matter”, *arXiv preprint astro-ph/9505029* (1995).

[76] P. Bode, J. P. Ostriker, and N. Turok, “Halo formation in warm dark matter models”, *The Astrophysical Journal* **556** (2001), no. 1, 93.

[77] V. Iršič et al., “New constraints on the free-streaming of warm dark matter from intermediate and small scale Lyman-α forest data”, *Phys. Rev. D* **96** (Jul, 2017) 023522, `doi:10.1103/PhysRevD.96.023522`.

[78] M. Viel, G. D. Becker, J. S. Bolton, and M. G. Haehnelt, “Warm dark matter as a solution to the small scale crisis: New constraints from high redshift Lyman-α forest data”, *Physical Review D* **88** (2013), no. 4, 043502.

[79] N. Menci, A. Grazian, M. Castellano, and N. Sanchez, “A stringent limit on the warm dark matter particle masses from the abundance of z= 6 galaxies in the Hubble frontier fields”, *The Astrophysical Journal Letters* **825** (2016), no. 1, L1.

[80] A. V. Macciò et al., “Cores in warm dark matter haloes: a Catch 22 problem”, *Monthly Notices of the Royal Astronomical Society* **424** (2012), no. 2, 1105–1112.

[81] D. N. Spergel and P. J. Steinhardt, “Observational evidence for self-interacting cold dark matter”, *Physical review letters* **84** (2000), no. 17, 3760.

[82] M. Vogelsberger and J. Zavala, “Direct detection of self-interacting dark matter”, *Monthly Notices of the Royal Astronomical Society* **430** (2013), no. 3, 1722–1735.

[83] S.-H. Oh et al., “Dark and luminous matter in THINGS dwarf galaxies”, *The Astronomical Journal* **141** (2011), no. 6, 193.

[84] J. L. Feng, M. Kaplinghat, and H.-B. Yu, “Halo-shape and relic-density exclusions of Sommerfeld-enhanced dark matter explanations of cosmic ray excesses”, *Physical Review Letters* **104** (2010), no. 15, 151301.

[85] S. Tulin, H.-B. Yu, and K. M. Zurek, “Beyond collisionless dark matter: particle physics dynamics for dark matter halo structure”, *Physical Review D* **87** (2013), no. 11, 115007.

[86] L. Ackerman, M. R. Buckley, S. M. Carroll, and M. Kamionkowski, “Dark matter and dark radiation”, *Physical Review D* **79** (2009), no. 2, 023519.

[87] J. L. Feng, M. Kaplinghat, H. Tu, and H.-B. Yu, “Hidden charged dark matter”, *Journal of Cosmology and Astroparticle Physics* **2009** (2009), no. 07, 004.

[88] M. R. Buckley and P. J. Fox, “Dark matter self-interactions and light force carriers”, *Physical Review D* **81** (2010), no. 8, 083522.

[89] A. Loeb and N. Weiner, “Cores in dwarf galaxies from dark matter with a Yukawa potential”, *Physical Review Letters* **106** (2011), no. 17, 171302.

[90] S. Tulin, H.-B. Yu, and K. M. Zurek, “Resonant dark forces and small-scale structure”, *Physical Review Letters* **110** (2013), no. 11, 111301.

[91] B. Holdom, “Two U(1)’s and Epsilon Charge Shifts”, *Phys. Lett.* **166B** (1986) 196–198, `doi:10.1016/0370-2693(86)91377-8`.

[92] R. Foot and R. Volkas, “Explaining ω baryon 0.2 ω dark through the synthesis of ordinary matter from mirror matter: a more general analysis”, *Physical Review D* **69** (2004), no. 12, 123510.

[93] M. Pospelov, A. Ritz, and M. Voloshin, “Secluded wimp dark matter”, *Physics Letters B* **662** (2008), no. 1, 53–61.

[94] N. Arkani-Hamed, D. P. Finkbeiner, T. R. Slatyer, and N. Weiner, “A theory of dark matter”, *Physical Review D* **79** (2009), no. 1, 015014.

[95] CDF Collaboration, “Search for anomalous production of multiple leptons in association with W and Z bosons at CDF”, *Phys. Rev. D* **85** (2012) 092001, `doi:10.1103/PhysRevD.85.092001`, `arXiv:1202.1260`.

[96] D0 Collaboration, “Search for dark photons from supersymmetric hidden valleys”, *Phys. Rev. Lett.* **103** (2009) 081802, `doi:10.1103/PhysRevLett.103.081802`, `arXiv:0905.1478`.

[97] D0 Collaboration, “Search for Events with Leptonic Jets and Missing Transverse Energy in $\mathbf{p\bar{p}}$ Collisions at $\sqrt{\mathbf{s}} = \mathbf{1.96}$ TeV”, *Phys. Rev. Lett.* **105** (2010) 211802, `doi:10.1103/PhysRevLett.105.211802`, `arXiv:1008.3356`.

[98] CMS Collaboration, “Search for Light Resonances Decaying into Pairs of Muons as a Signal of New Physics”, *JHEP* **07** (2011) 098, `doi:10.1007/JHEP07(2011)098`, `arXiv:1106.2375`.

[99] CMS Collaboration, “Search for a Non-Standard-Model Higgs Boson Decaying to a Pair of New Light Bosons in Four-Muon Final States”, *Phys. Lett. B* **726** (2013) 564–586, `doi:10.1016/j.physletb.2013.09.009`, `arXiv:1210.7619`.

[100] CMS Collaboration, “A search for pair production of new light bosons decaying into muons”, *Phys. Lett. B* **752** (2016) 146–168, `doi:10.1016/j.physletb.2015.10.067`, `arXiv:1506.00424`.

[101] CMS Collaboration, “Search for dark photons in decays of Higgs bosons produced in association with Z bosons in proton-proton collisions at $\sqrt{s} = 13$ TeV”, *JHEP* **10** (2019) 139, `doi:10.1007/JHEP10(2019)139`, `arXiv:1908.02699`.

[102] ATLAS Collaboration, “Search for displaced muonic lepton jets from light Higgs boson decay in proton-proton collisions at $\sqrt{s} = 7$ TeV with the ATLAS detector”, *Phys. Lett. B* **721** (2013) 32–50, `doi:10.1016/j.physletb.2013.02.058`, `arXiv:1210.0435`.

[103] ATLAS Collaboration, “A search for prompt lepton-jets in pp collisions at $\sqrt{s} = 7$ TeV with the ATLAS detector”, *Phys. Lett. B* **719** (2013) 299–317, `doi:10.1016/j.physletb.2013.01.034`, `arXiv:1212.5409`.

[104] ATLAS Collaboration, “Search for WH production with a light Higgs boson decaying to prompt electron-jets in proton-proton collisions at $\sqrt{s}$=7 TeV with the ATLAS detector”, *New J. Phys.* **15** (2013) 043009, `doi:10.1088/1367-2630/15/4/043009`, `arXiv:1302.4403`.

[105] ATLAS Collaboration, “Search for long-lived neutral particles decaying into lepton jets in proton-proton collisions at $\sqrt{s} = 8$ TeV with the ATLAS detector”, *JHEP* **11** (2014) 088, `doi:10.1007/JHEP11(2014)088`, `arXiv:1409.0746`.

[106] ATLAS Collaboration, “A search for prompt lepton-jets in pp collisions at $\sqrt{s} = 8$ TeV with the ATLAS detector”, *JHEP* **02** (2016) 062, `doi:10.1007/JHEP02(2016)062`, `arXiv:1511.05542`.

[107] ATLAS Collaboration, “Search for light long-lived neutral particles produced in pp collisions at $\sqrt{s} = 13$ TeV and decaying into collimated leptons or light hadrons with the ATLAS detector”, *Eur. Phys. J. C* **80** (2020), no. 5, 450, `doi:10.1140/epjc/s10052-020-7997-4`, `arXiv:1909.01246`.

[108] LHCb Collaboration, “Search for hidden-sector bosons in $B^0 \to K^{*0}\mu^+\mu^-$ decays”, *Phys. Rev. Lett.* **115** (2015), no. 16, 161802, `doi:10.1103/PhysRevLett.115.161802`, `arXiv:1508.04094`.

[109] LHCb Collaboration, "Search for Dark Photons Produced in 13 TeV *pp* Collisions", *Phys. Rev. Lett.* **120** (2018), no. 6, 061801, `doi:10.1103/PhysRevLett.120.061801`, `arXiv:1710.02867`.

[110] A. Berlin, S. Gori, T. Lin, and L.-T. Wang, "Pseudoscalar portal dark matter", *Physical Review D* **92** (2015), no. 1, 015005.

[111] S. Banerjee et al., "Cornering pseudoscalar-mediated dark matter with the lhc and cosmology", *Journal of High Energy Physics* **2017** (2017), no. 7, 80.

[112] U. Haisch and F. Kahlhoefer, "On the importance of loop-induced spin-independent interactions for dark matter direct detection", *Journal of Cosmology and Astroparticle Physics* **2013** (2013), no. 04, 050.

[113] T. Li, "Revisiting the direct detection of dark matter in simplified models", *Physics Letters B* **782** (2018) 497–502.

[114] L. Evans and P. Bryant, "LHC machine", *Journal of instrumentation* **3** (2008), no. 08, S08001.

[115] CMS Collaboration, "The CMS tracker system project: Technical Design Report",.

[116] CMS Collaboration, "The CMS electromagnetic calorimeter project: Technical Design Report",.

[117] CMS Collaboration, "The CMS hadron calorimeter project: Technical Design Report",.

[118] R. Brun and F. Rademakers, "ROOT—an object oriented data analysis framework", *Nuclear Instruments and Methods in Physics Research Section A: Accelerators, Spectrometers, Detectors and Associated Equipment* **389** (1997), no. 1-2, 81–86.

[119] J. Alwall et al., "The automated computation of tree-level and next-to-leading order differential cross sections, and their matching to parton shower simulations", *JHEP* **07** (2014) 079, `doi:10.1007/JHEP07(2014)079`, `arXiv:1405.0301`.

[120] CMS Collaboration, "Search for new physics in final states with an energetic jet or a hadronically decaying W or Z boson and transverse momentum imbalance at $\sqrt{s} = 13$ TeV", *Phys. Rev. D* **97** (2018), no. 9, 092005, `doi:10.1103/PhysRevD.97.092005`, `arXiv:1712.02345`.

[121] T. Sjöstrand et al., "An introduction to PYTHIA 8.2", *Comput. Phys. Commun.* **191** (2015) 159–177, `doi:10.1016/j.cpc.2015.01.024`, `arXiv:1410.3012`.

[122] GEANT4 Collaboration, "GEANT4–a simulation toolkit", *Nucl. Instrum. Meth. A* **506** (2003) 250–303, `doi:10.1016/S0168-9002(03)01368-8`.

[123] J. Allison et al., "Geant4 developments and applications", *IEEE Trans. Nucl. Sci.* **53** (2006) 270, `doi:10.1109/TNS.2006.869826`.

[124] J. Allison et al., “Recent developments in Geant4”, *Nucl. Instrum. Meth. A* **835** (2016) 186–225, `doi:10.1016/j.nima.2016.06.125`.

[125] CMS Collaboration, “Extraction and validation of a new set of CMS PYTHIA8 tunes from underlying-event measurements”, *Eur. Phys. J. C* **80** (2020), no. 1, 4, `doi:10.1140/epjc/s10052-019-7499-4`, `arXiv:1903.12179`.

[126] CMS Collaboration, “The CMS muon system in Run2: preparation, status and first results”, *PoS* **EPS-HEP2015** (2015) 237, `doi:10.22323/1.234.0237`, `arXiv:1510.05424`.

[127] CMS Collaboration, “Search for decays of stopped exotic long-lived particles produced in proton-proton collisions at $\sqrt{s} = 13$ TeV”, *JHEP* **05** (2018) 127, `doi:10.1007/JHEP05(2018)127`, `arXiv:1801.00359`.

[128] CMS Collaboration, “CutBasedElectronIdentificationRun2 < CMS < TWiki”. `https://twiki.cern.ch/twiki/bin/view/CMS/CutBasedElectronIdentificationRun2#Electron_ID_Working_Points_WP_de`.

[129] CMS Collaboration, “CutBasedPhotonIdentificationRun2 < CMS < TWiki”. `https://twiki.cern.ch/twiki/bin/view/CMS/CutBasedPhotonIdentificationRun2#Photon_ID_Working_Points_WP_defi`.

[130] CMS Collaboration, “MuonIdRun2 < CMS < TWiki”. `https://twiki.cern.ch/twiki/bin/viewauth/CMS/SWGuideMuonIdRun2#Loose_Muon`.

[131] M. Cacciari, G. P. Salam, and G. Soyez, “The anti-k_t jet clustering algorithm”, *JHEP* **04** (2008) 063, `doi:10.1088/1126-6708/2008/04/063`, `arXiv:0802.1189`.

[132] M. Cacciari, G. P. Salam, and G. Soyez, “FastJet User Manual”, *Eur. Phys. J. C* **72** (2012) 1896, `doi:10.1140/epjc/s10052-012-1896-2`, `arXiv:1111.6097`.

[133] D. Guest et al., “Jet Flavor Classification in High-Energy Physics with Deep Neural Networks”, *Phys. Rev. D* **94** (2016), no. 11, 112002, `doi:10.1103/PhysRevD.94.112002`, `arXiv:1607.08633`.

[134] CMS Collaboration, “Identification of heavy-flavour jets with the CMS detector in pp collisions at 13 TeV”, *JINST* **13** (2018), no. 05, P05011, `doi:10.1088/1748-0221/13/05/P05011`, `arXiv:1712.07158`.

[135] G. Cowan, K. Cranmer, E. Gross, and O. Vitells, “Asymptotic formulae for likelihood-based tests of new physics”, *Eur. Phys. J. C* **71** (2011) 1554, `doi:10.1140/epjc/s10052-011-1554-0`, `arXiv:1007.1727`. [Erratum: Eur.Phys.J.C 73, 2501 (2013)].

[136] CMS Collaboration, “Current Recommendations for Luminosity Estimations”. `https://twiki.cern.ch/twiki/bin/view/CMS/TWikiLUM#CurRec`.

[137] CMS Collaboration, “CMS Internal TWiki < Non standard features of the Higgs PAG limit setting tool”. `https://twiki.cern.ch/twiki/bin/viewauth/CMS/HiggsWG/SWGuideNonStandardCombineUses`.

[138] T. Junk, “Confidence level computation for combining searches with small statistics”, *Nucl. Instrum. Meth. A* **434** (1999) 435–443, `doi:10.1016/S0168-9002(99)00498-2`, `arXiv:hep-ex/9902006`.

[139] A. L. Read, “Presentation of search results: The CL(s) technique”, *J. Phys. G* **28** (2002) 2693–2704, `doi:10.1088/0954-3899/28/10/313`.

[140] P. Madau, S. Shen, and F. Governato, “Dark matter heating and early core formation in dwarf galaxies”, *The Astrophysical Journal Letters* **789** (2014), no. 1, L17.